Fault Tolerant Position Control of SM-PMSM In an Electro-Mechanical Brake Actuator Against AMR Angle Sensor Failure

Von der Fakultät IV-Elektrotechnik und Informatik
der Technischen Universität Berlin
zur Erlangung des akademischen Grades

Doktor der Ingenieurwissenschaften
-Dr.-Ing-

genehmigte Dissertation

vorgelegt von
Diplom-Ingenieur
Lai Geng

Promotionsausschuss:

Vorsitzender: Prof. Dr.-Ing. Stephan Völker
1. Gutachter: Prof. Dr.-Ing. Clemens Gühmann
2. Gutachter   Prof. Dr.-Ing. Uwe Schäfer

Tag der wissenschaftlichen Aussprache: 18.09.2008

Berlin 2008
D83

Danksagung

Die vorliegende Arbeit entstand im Rahmen meiner Tätigkeit als Doktorand bei der Robert Bosch GmbH Forschung und Vorausentwicklung in Schwieberdingen, Deutschland.

An dieser Stelle möchte ich mich zuerst bei allen Kollegen der Abteilung CR/AEV bedanken, die mich während der vergangenen Jahre unterstützt haben. Herrn Dr.-Ing. Cao Chi-Thuan und Herrn Prof. Dr.-Ing. Clemens Gühmann gilt mein besonderer Dank. Ihre kompetente fachliche Betreuung sowie den Beistand während der schwierigen Zeit waren ganz entscheidend für das Gelingen dieser Arbeit. Mein herzlicher Dank geht ebenfalls an Herrn Wolfgang Haas, der mir die ganze Wissensreserve des damaligen Projekts über sensorlose Regelung zur Verfügung stellte.

Herrn Peter Claus und Herrn Dietmar Martini danke ich für ihre tatkräftige Unterstützung beim Aufbauen des Prüfstands. Herrn Prof. Dr.-Ing. Uwe Schäfer möchte ich für die sofortige Bereitschaft, das zweite Gutachten zu übernehmen, für die interessante Diskussion und Tipps herzlich danken. Bei Herrn Dr. Dirk Hofmann bedanke ich mich auch herzlich für die Promotionsmöglichkeit bei Bosch. Herrn Dipl.-Ing. Stefan Strengert möchte ich auch danken für die vielen wichtigen Tipps über Echtzeit Simulation und Rapid-Control-Prototyping.

Nicht zuletzt gilt mein Dank meinen Eltern und meiner Freundin Ying Hong für ihre ständige Ermutigung.

Zusammenfassung

Die vorliegende Arbeit leistet einen Beitrag zur Fehlertoleranz einer von Robert Bosch GmbH entwickelten elektromechanischen Keilbremse. Durch die Fehlermöglichkeits- und Einfluss-Analyse (FMEA) wurde der AMR-Winkelsensor (AMR: anisotropischen magnetischen Widerstand) als eine der kritischsten Komponenten in dem Bremsaktuator festgestellt. Der AMR-Winkelsensor liefert den Rotorwinkel einer Permanentmagnet-Synchronmaschine mit oberflächemontiertem Magnet (SM-PMSM). Dieser Motor erzeugt die definierte Bewegung des Keils im Bremsaktuator. Ohne Fehlertoleranz führt der Fehler des AMR Winkelsensors zum unvoraussehbaren Verhalten des Bremsmoments. Die vorliegende Arbeit fokussiert sich auf dieser Problematik und strebt einer Softwarelösung der Fehlertoleranz an, um Ausschalten des Bremsaktuators beim AMR Winkelsensorausfall zu vermeiden. Softwarelösungen haben den Vorteil, dass sie kaum zusätzliche Produktionskosten verursachen.

Ein Schema der aktiven fehlertoleranten Regelung wird in dieser Arbeit entworfen, indem der Positionsregler zwischen den gemessenen und geschätzten Rotorwinkel umgeschaltet wird. Das Fehlerverhalten wird untersucht und die entsprechende Fehlererkennung wird entworfen. Die Verfahren der Winkelschätzung von SM-PMSM werden vergleicht und untersucht. Eine Ad-hoc-Lösung für die Winkelschätzung dieser Maschinentyp in dem gesamten Drehzahlbereich einschließlich Stillstand wird entwickelt. Ein neuer Positionsregler ohne Kaskadenregelung wird ebenfalls hergeleitet. Die Parametereinstellung des Positionsreglers ist problemlos möglich aufgrund seiner einfachen Struktur. Zur Validierung der Algorithmen wird ein Rapid-Control-Prototyping Prüfstand aufgebaut.

Abstract

This study is part of the development of fault tolerance function for an electro-mechanical wedge brake actuator at the Robert Bosch GmbH. Through the *Fault Mode and Effect Analysis* (FMEA) on the present brake actuator design, the AMR angle sensor (AMR: anisotropic magnetic resistance) is identified as one of the most critical components in the brake actuator. This angle sensor is applied to measure the rotor angle of a surface-mount permanent magnet synchronous machine (SM-PMSM), which produces the desired displacement of the wedge in the brake caliper. Without fault tolerance measure, the failure of the AMR angle sensor would lead to unpredictable brake moment. This study focuses on this problematic and strives for a software fault tolerance solution to cope with AMR sensor fault without shutting down the actuator. Software solution needs little hardware change and involves hardly any production cost increase.

An active fault tolerant control scheme has been proposed in which the position controller is switched online between the measured and the estimated rotor angle. The fault behavior of the AMR angle sensor is investigated and a fault detection module is designed. The rotor angle estimation of an SM-PMSM in the whole rotor speed range is investigated and an ad-hoc solution is proposed for the application in the specific brake actuator. A position controller with single closed-loop structure instead of cascaded closed-loop structure has also been designed. The parameter tuning of the position control is very simple thanks to the simple structure of the new controller. For the validation of the algorithm with real SM-PMSM hardware, a rapid control prototyping test bench is designed and built.

Contents

Nomenclature

A_s The amplification factor of the sine channel of the AMR sensor

A_c The amplification factor of the cosine channel of the AMR sensor

$e_{\alpha,\beta}$ Back-EMF components in the α-β coordinate system.

H Magnetic field strength

$\vec{I}_s$ Stator current vector

J Rotor inertia

M_{el} Torque of one equivalent single-pole-pair motor (the electrical moment)

M_{mech} Motor torque (the mechanical moment)

M_{load} The loading moment on rotor shaft

N Number of turns

R Phase resistance of the stator

U_b The supply voltage of the AMR angle sensor

$\vec{U}$ Voltage vector in the stator-fixed coordinate system.

Z_p Number of pole pairs.

Φ_{pm} Permanent magnet flux of one pole pair

Ψ_{pm} Flux linkage of the permanent magnet flux ($N \cdot \Phi_{pm}$)

θ^* Set value of the electrical angle of the rotor

$\bar{\theta}$ Measurement of the mechanical rotor angle.

θ_{dc} Angle of the dc-axis in the dc-qc coordinates

θ_d, θ_{el} Rotation angle of the equivalent single-pole-pair motor (the electrical angle)

θ_{mech} Rotation angle of motor (the mechanical angle)

$\Delta\theta$ $\theta_{dc} - \theta_d$

ω_1 Rotation speed of the dc-qc coordinate system; the estimated rotor speed (electrical).

ω_r Rotation speed of the d-q coordinate system, also the electrical rotating speed of the rotor

ω_{mech} The rotor rotation speed

λ Stator flux linkage

Chapter 1

Introduction

1.1 Introduction to Brake by Wire

X-by-wire technology was originally developed and used in the aviation industry. Airplane engineers found that eliminating bulky mechanical systems and replacing them with electronic systems makes airplanes lighter and more compact. The by-wire technology also facilitates computer assisted control. Automotive engineers have studied this technology and have been developing ways to translate it to passenger cars. Typical examples of such attempts are the research on the steer-by-wire and brake-by-wire. Such by-wire systems replace the traditional mechanical and hydraulic control of steer or brake systems in automobile with electronic control using electromechanical actuators and human-machine interfaces such as pedal and steering feel emulators. Some X-by-wire technologies have been already installed on commercial vehicles such as throttle-by-wire. Brake-by-wire technology is still under development and has not been widely commercialized. This is mainly due to the safety critical nature of brake products. An intermediate solution for the brake-by-wire technology currently in commercial use is the electro-hydraulic brake (EHB), which decouples the brake pedal from the hydraulic brake system. The vacuum booster in conventional hydraulic brake is replaced by electric pump. The distribution of the brake pressure on four wheels is electronically controlled. Direct hydraulic connection between brake pedal and the front wheel brakes still exists and is used as backup in case of electronic control failure.

In a 'pure' brake-by-wire system, the hydraulic system is completely removed. The driver's will on deceleration is interpreted by measuring the brake pedal movement. The signal from the pedal sensors would be fed to the electronic control unit (ECU)

which decides the braking moment distribution. The brake moment of each wheel is produced by an electro-mechanical brake actuator. The braking moment at each wheel can thus be controlled independently.

$C_{calipler}$: the elastic constant of the caliper

Δy: elastic deformation of the caliper

F_{app}:   the application force, i.e. the actuation force
              from the electric drive

F_n: the normal force on the brake disc

F_f: the friction force between the brake disc and
              the lining.

μ: friction coefficient
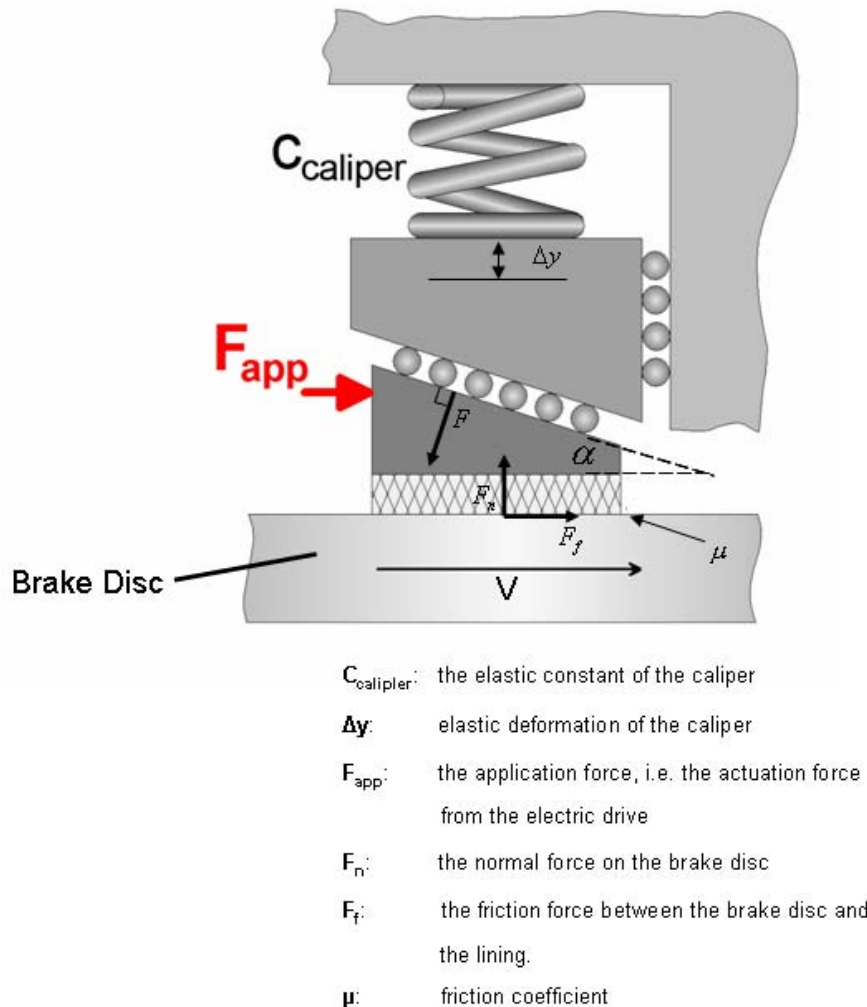
Figure 1.1: The principle sketch of a wedge brake.

Various concepts of electrical brake actuator have been proposed with the same purpose, i.e. to press the lining to the brake disk or brake drum. Early designs use high power electric drives to produce the lining pressure up to several tons with e.g. ball screw construction. The large current of the electric drives can damage the conventional 14 V vehicle power net. Wedge brake is an intelligent concept to reduce the necessary actuation force and thus the necessary current. Wedge brake utilizes the friction between the lining and the brake disc to amplify the lining pressure instead of producing the lining pressure solely with the electric drive. Figure 1.1 shows a principle sketch of a wedge brake. For simplicity, it is assumed that the application force, i.e. the actuation force brought by the electric drive is in the horizontal direc-

tion. Without derivation, the normal force on the brake disc is described by equation 1.1, if the brake disc rotates in the direction shown in figure 1.1.

$$F_n = \frac{1}{\tan\alpha - \mu} \cdot F_{app} \qquad\qquad (1.1)$$

From equation 1.1, it is trivial that the amplification of the normal force can be adjusted by choosing a proper wedge angle. To utilize the self-strengthening effect for both wheel rotating directions, construction with wedges in both directions is a possible solution. The necessary application force is thus significantly reduced and so is the current in the electric drive. Smaller electric drive (<5 kW) is sufficient for wedge brakes. This not only avoids damage to the 14 V vehicle power net but also reduces the unsprung mass and the volume.

Using electro-mechanical brakes (EMB) has several advantages. The main benefit is that the control response of the brake actuator is faster than hydraulic system, resulting in shorter stop distance and better performance of vehicle dynamic control. Since the hydraulic system is replaced by electronic control and electric actuation, the brake is very 'quiet'. The brake by wire takes up much less space than the hydraulic brake which is an important advantage for the automotive manufacturers considering how tight engine compartments have become today. Environmental damage of the corrosive and toxic brake fluid is avoided. The maintenance effort is also reduced due to the automatic diagnosis. New functions for brake are merely an update of the software without hardware modification. Brake pedal is no longer necessary which results in better passenger safety at collision and flexible interior design.

1.2 The Motivation and Scope of the Study

Safety has always been a concern with any new system; even more so with a safety critical item such as brakes. The enormous maintenance effort for airplanes is not affordable for automobile in mass utilization. This results in very high requirement on the reliability and availability of EMB. Brake regulations, e.g. ECE Nr.13, has made it compulsory for brake systems in automobile to have a dual system. For EMB, this means dual pedal sensors, dual control computers (ECU), dual communication channels and dual power supply. An example of such redundant system architecture is shown in figure 1.2.
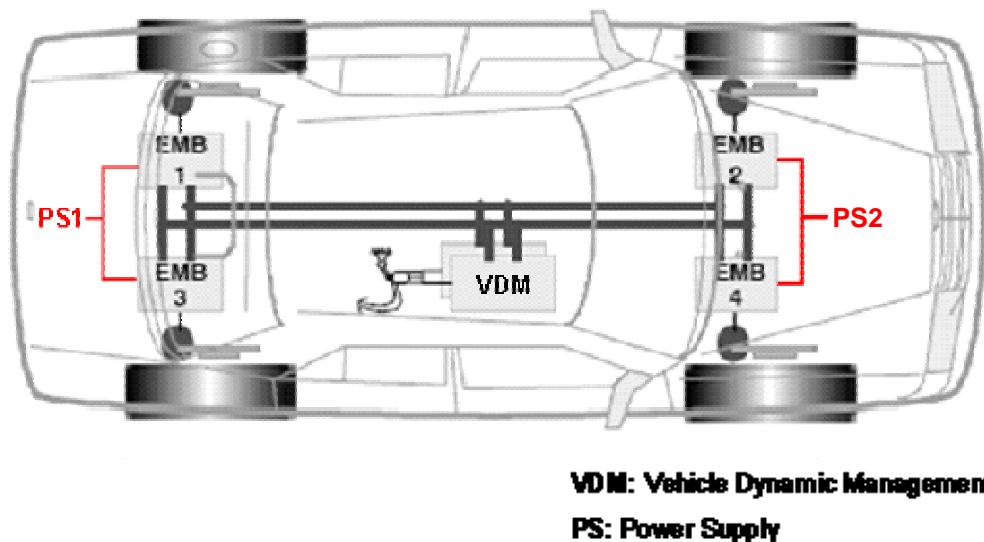
Figure 1.2: an example of the system architecture of EMB

With redundant system architecture, it is a widely accepted approach to shut down the brake actuator if a critical fault is detected in that specific brake actuator. Because the four brake actuators are considered as redundancy for one another and one can brake theoretically with even only one wheel. However, the loss of the brake moment on one wheel, especially on a front wheel, causes not only the reduction of the total deceleration (up to ca. 30%) but also introduces a yaw moment on the vehicle. Though the compensation of the yaw moment is possible with proper coordination of steering and braking, the operation can be dangerous for inexperienced drivers if the change of vehicle behavior is unexpected. The psychological impact on inexperienced driver of such sudden change can also promote human errors, which worsen the driver reaction and increase the probability of accident. Therefore, sudden shut down of one or more brake actuators is not a safe option for fault handling. To avoid brake actuator shut down as much as possible, fault tolerance of each of the four brake actuators is desired despite the redundant system architecture.

The tolerance to the brake moment loss of one or more brake actuators could also be provided by an intelligent vehicle dynamic management (VDM), which modifies the distribution of the brake moment. However, such advance vehicle dynamic control is not considered as part of the 'basic' brake system so far. It is very likely that the basic brake system is later combined with vehicle dynamic control from different manufacturer whose functions are not standardized. Therefore, under the current product modularization, the safety of the basic brake system should be maximized independent from any specific design of the vehicle dynamic control.

This study is part of the development of fault tolerance for an EMB wedge brake actuator at the Robert Bosch GmbH. Through the *Fault Mode and Effect Analysis* (FMEA) on the present brake actuator design, the AMR angle sensor has been identified as one of the most critical components in the brake actuator. This angle sensor is applied to measure the rotor angle of a surface-mount permanent magnet synchronous machine (SM-PMSM), which produces the desired displacement of the wedge in the brake caliper. And this displacement of the wedge results in a defined normal force between the brake lining and brake disc and thus a defined brake moment on the wheel. Without fault tolerance measure, the malfunction of the AMR angle sensor would lead to the failure of the position control of the SM-PMSM. And this results in unpredictable brake moment. The brake actuator has to be shut down immediately. This study focuses on this problematic and strives for a fault tolerance solution to cope with AMR sensor fault without shutting down the actuator.

An intuitive fault tolerant solution for the AMR sensor would be using redundant AMR sensors for the fault monitoring and the angle measurement. However, the redundant AMR sensor introduces extra production cost due to the extra electronic components and the more complex design of the mechanical housing. For mass production in the automotive industry, such cost increase is very unfavorable. The goal of the study is therefore to develop a software fault tolerant solution for brake actuator control under AMR sensor malfunction. Software solution has the advantage of posing hardly any production cost and is therefore preferred if feasible. The study itself can also serve as an example for the development of software fault-tolerant functions for the other components in the brake actuator.

The problematic to be tackled is basically a fault tolerant control problem. Fault tolerant control can generally be divided into three steps.

- Fault detection, isolation and identification.
- Decision making.
- Controller reconfiguration.

Fault detection can be signal-based or model-based [6]. Signal-based fault detection monitors the signal features that indicate the fault status while model-based fault detection uses mathematical model of the system to estimate some measurable quantities and compare them to the measurement. In this study, both detection approaches have been investigated. For signal-based fault detection, the circular locus of the sensor output vector (sine, cosine) is a typical signal feature that can be used to detect AMR sensor faults. Fault detection method with this signal feature has become stan-

dard meanwhile. If the fault effect does not violate the circular locus of the sensor output vector, e.g. constant output vector on the standard circle; model-based fault detection can check the plausibility of the measured angle. The model-based fault detection compares the estimated rotor angle and the angle measurement from the AMR angle sensor. The rotor angle can be estimated with motor current and voltage. The estimated rotor angle is also used by the position controller in the case of AMR sensor malfunction. Controller reconfiguration is not necessary.

If the signal-based fault detection reports fault event, the fault source can be isolated, because the fault detection only bases on the output signals from the AMR sensor. If the fault event is only reported by the comparison of the estimated rotor angle and the measured angle, i.e. the model-based fault detection; then fault status of the current sensors should also be taken into account to determine the fault source[1]. It should be noted that once the current sensors are determined to be faulty, the fault detection on the AMR sensor is no longer exhaustive. Because the model-based plausibility check is no longer reliable; and some fault types, e.g. constant sensor output vector, can not be detected. It is assumed in this study that the vehicle will be repaired as soon as possible after the first fault has been detected; and no more fault event occurs before the reparation. Under this assumption, the situation that both the current sensors and the AMR sensor are faulty at the same time is not discussed.

For amplitude fault and offset fault of the AMR sensor, fault identification and compensation is theoretically possible with online estimation of the new amplitude and offset parameters. This possibility has also been investigated. The estimation with least-square method (LS), recursive least square method (RLS) and recursive least square with forgetting factor have been studied. However, none of these methods provides satisfying solution. Therefore the online compensation of amplitude fault and offset fault is not included in the proposed fault tolerant control. Some discussion about this problem is presented in section 4.3.

The decision making function determines if the measured rotor angle or the estimated rotor angle is fed to the motor position controller. If neither of them is possible, the brake actuator still has to be shut down. But this scenario occurs only if the AMR sensor and the current sensors are faulty at the same time. To avoid instability of the position control loop caused by frequent switching between the measured and estimated rotor angle; the decision making function does not allow such frequent switching. Once the position controller starts using the estimated rotor angle, switching

---

[1] The motor phase voltages are internal signals of the control algorithm. These signals are therefore always 'correct'.

back to the measured angle will only take place if the conditions for using measured angle have been fulfilled for long enough time. How long this time should be remains a topic for discussion in the future study. And restarting the brake actuator from the shut down state is also beyond the consideration of this study, since this would involve analysis on the details of too many functions in the EMB system.

The rotor angle estimation with motor current and voltage is of essential importance for the fault tolerant control against AMR sensor fault, since otherwise the brake actuator can only be shut down. In chapter 5, various rotor angle estimation methods for SM-PMSM found in the literature are analyzed. The estimation methods can be classified as passive methods and active methods. Passive estimation methods do not inject any current or voltage test signals while active methods do.

The passive estimation methods exploit the physical effect of either the stator winding flux-linkage or the back electro-motive force (back-EMF). Estimation using Extended-Kalman Filter (EKF) is a sophisticated method that does not explicitly estimate the back-EMF. But it is not applicable if the back-EMF vanishes (motor standstill). In general, back-EMF based estimation methods have very good performance and robustness for estimation at high and medium rotor speed (>100 rpm); but they fail if the rotor speed is low since the back-EMF is too weak for a robust estimation. The application of flux-linkage based angle estimation is theoretically not restricted by the rotor speed. However, the widely known DC-drift problem of the open-loop integration fails such methods. Although Hu and Wu [21] proposed an elegant solution to constrain the DC-drift by using a closed-loop integrator structure with first-order delay and amplitude limiter; the angle estimation still drifts.

For angle estimation at very low rotor speed and stand still, active estimation method is an intensive research field. The active estimation methods inject high frequency current or voltage test signals in the motor winding and detect the rotor-position-dependent inductance anisotropy by analyzing the voltage or current response of the test signals. The active methods can be further classified in two groups according to the injected test signal [49]. The first group injects strong voltage/current pulse periodically in the stator winding and triggers strong magnetic saturation in the iron, which leads to significant inductance anisotropy. But the big amplitude of the current pulse introduces strong torque ripples; and this seriously disturbs the position control of the motor and shortens the durability of the bearing. Depending on the frequency of the test signal, acoustic noise is also a problem. The other group of active estimation methods detects the weak magnetic saturation effect by injecting continuous carrier signal. Such methods do not have the problem of torque ripples. However, the

inductance anisotropy is too weak in an SM-PMSM for a robust estimation. Further more, the estimation will be erroneous under mechanical load. Recently a new type of injection signal is introduced in [44]. The injected test signal has a very high frequency of 100-500 kHz[2]. However, this kind of oscillation signal can not be generated by conventional power converters that normally work at a frequency of 20 kHz or less. Extra hardware is therefore needed for the high frequency test signal generation which makes this method not practical for commercial use.

So far there is no mature angle estimation method for SM-PMSM which is applicable for the whole operation speed range including standstill. For high and medium rotor speed, back-EMF based angle estimation with observer is a robust method with small computation effort. For very low rotor speed and standstill, the flux-linkage based method proposed by Hu and Wu [21] is the only reasonable choice at the moment. But as mentioned before, the angle estimated with this method still drifts. An ad-hoc solution for this problem is to add a small but fast position variation to the position set value periodically if the rotor speed dwells under the speed threshold for long enough time. With this position set value manipulation, the rotor speed is forced to exceed the threshold after certain time dwelling in the very low speed range. And once the rotor speed is higher than the threshold, the closed-loop back-EMF based angle estimation will correct the drift and re-initialize the flux-linkage based estimation when the rotor speed falls below the threshold again. The period of this position set value manipulation depends on the offset error of the current measurement, which influence the drift speed of the angle estimate. The bigger the offset error is, the faster the drift will be and hence the shorter period should be chosen. The waveform of the additional position set value variation should be able to force the rotor speed to exceed the speed threshold; and the amplitude of the additional position variation should be as small as possible to minimize the disturbance on the brake moment control. The period and the waveform of the position set value manipulation had been determined empirically during the test bench experiment.

1.3 Dissertation Outline

The organization of the dissertation is as follows:

Chapter 1 makes a brief introduction to the content of the dissertation.
Chapter 2 introduces the development process of the solution and the experiment environment for the study.

---

[2] The injection signals of the other methods have typically the frequency in the range of 0.5 kHz-3 kHz.

Chapter 3 first introduces the background knowledge of the position control of the SM-PMSM in the brake actuator and then presents the fault tolerant control scheme.

Chapter 4 discusses about the fault behavior of the AMR angle sensor. The fault detection and the decision making are presented. The discussion about the possibility of online compensation for amplitude fault and offset fault of the AMR sensor can also be found in this chapter.

Chapter 5 describes the various rotor angle estimation methods and explains the estimation method used in the proposed fault tolerant control.

Chapter 6 presents the experiment results.

Chapter 7 makes a summary on the study and outlines possible future research.

Chapter 2

The Development Process and the Experiment Environment

2.1 The Development Process of the Fault Tolerant Control

Electronic control systems are intensively utilized in today's automobile for many purposes, e.g. more comfort, more safety, weight reduction. The functions of the electronic systems are versatile ranging form power train control, chassis control to car entertainment. The information exchange among them creates a highly complex network. The complexity of developing safe and reliable automotive electronic systems increases dramatically. As a safety critical system, the safety and reliability of EMB is of utmost importance. Improving product safety and reliability is a challenge embedded in the whole product life cycle from the product conception to product disposal. The international norm IEC 61508 provides a general guideline for all the activities during the life cycle of a safety relevant system such as brake-by-wire which utilizes electrical and/or electronic components to realize its safety functions. The overall product life cycle is summarized in IEC 61508 as shown in figure 2.1. The development of the technical fault tolerant functions can be considered as part of the realization steps in the product life cycle (step 9 to 11).

For the development of software in general (not only for automotive electronics), several standard processes models have be established in the industry. The *C*apability-*M*aturity-*M*odel-*I*ntegration (CMMI) model defines the requirements on a good development process but does not specify how these requirements can be achieved. It is actually a modular system to assess and improve the quality of the product development process. The *S*oftware *P*rocess *I*mprovement and *C*apability *D*etermination (SPICE) model is also only an auxiliary process for evaluating the concrete devel-

opment process. The V-Model is very widely adopted in the automotive industry. It was first developed in 1986 by the German Federal Ministry of Defense. The goal is to reduce development cost and development risk while being compliant with various norms and ensuring a minimal quality of the software.
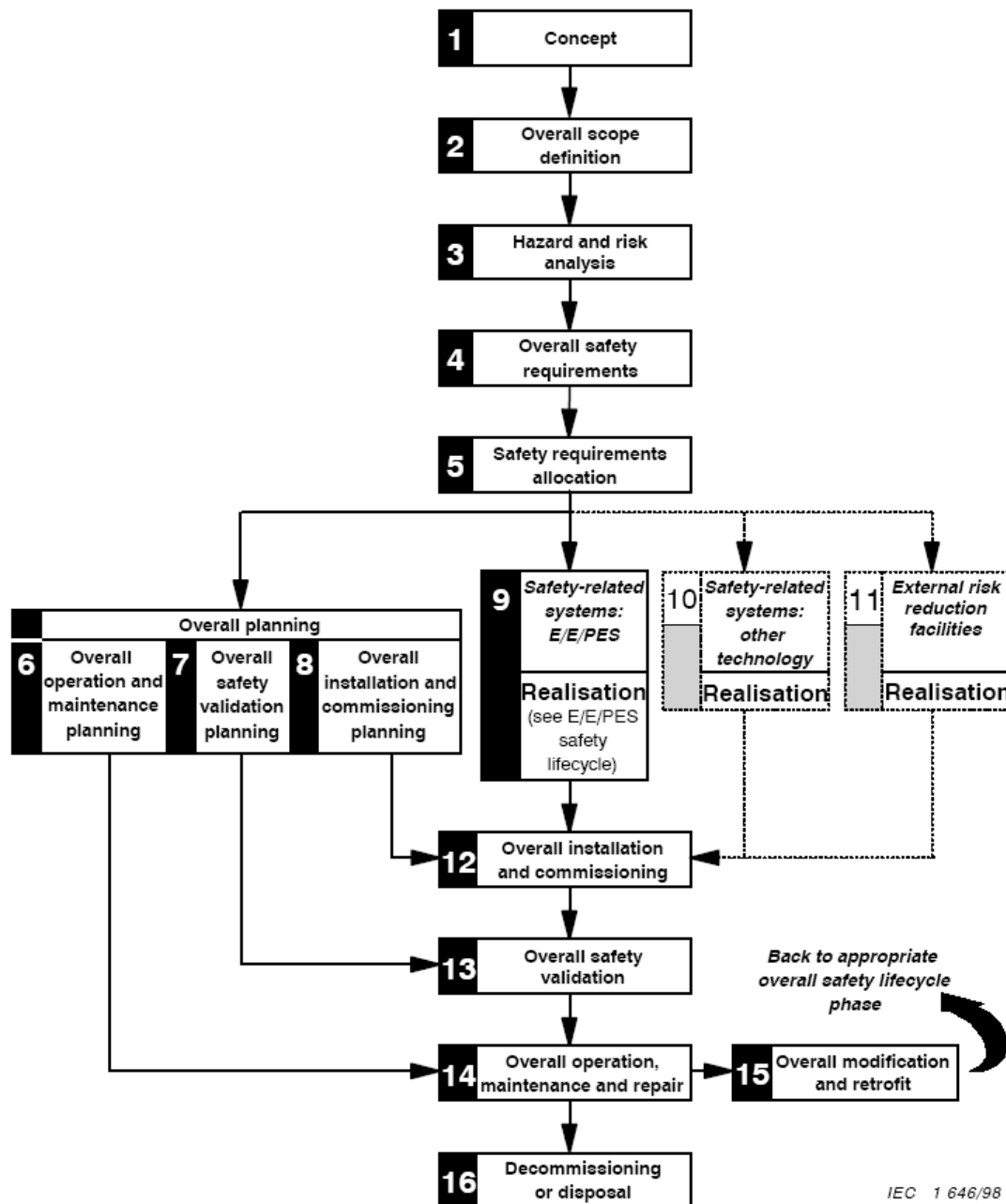

Figure 2.1: the product safety lifecycle in IEC 61508.

The V-Model is an abstract, comprehensive project management structure. Its name comes from its V-shaped illustration of the project elements in the software development, arranged according to their time sequence and the depth of development detail. Different from the classical phase model in project management, the V-model

only defines the activities and results of each step but does not specifies the time-frame of the steps. Iterations are possible between the steps. The activities in a V-model can also be projected in a waterfall model or a spiral model. The V-model is often modified and adapted to different product development projects and is no longer restricted to the software product. Figure 2.2 shows an example of the V-model for software development for automobile electronics.
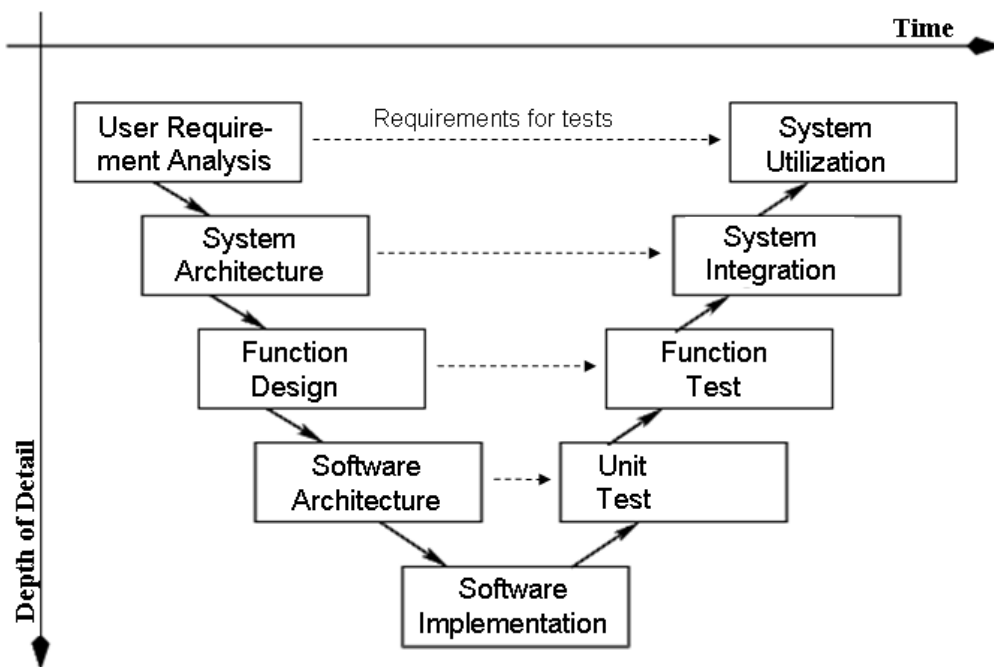
Figure 2.2: the V-model for software development for automobile electronics.

The development always starts from defining the requirements for the system to be designed and ends up with the system test. The requirements on the system are used as criteria for the system test. At the bottom of the V-model is the implementation of the software on the computation platform. The intermediate steps are adapted in the specific projects. Actually the development process of every subsystem or sub-function also follows its own V-model.

2.2 The Experiment Environment

2.2.1 An Overview of the Experiment Environment

For the development and validation of the fault tolerant control, an experiment environment is designed and built. The requirements on the functions of the experiment environment are determined by the development. The development of fault tolerant control is separated into four steps. After the requirement definition the fault tolerant control is first analytically derived; the algorithm is first tested in offline simulation with actuator and sensor models. If the simulation is successful, the algorithm will be implemented on a motor test bench to exam the performance and robustness of the algorithm with real actuator components.

For the offline simulation of the fault tolerant control, the simulation tool *Matlab/Simulink*® from Mathworks is applied. For the test of the algorithm with real actuator components, a motor test bench and a real time computation platform are built. The implementation of the algorithm with manual coding is very time consuming and error-prone. During the development of the algorithm, it is expected that the algorithm will be modified very frequently. Hence the manual implementation is not practical. Automation is needed to accelerate the development. Optimal will be a simulation environment, in which the offline simulation model can be automatically converted into real time application with little modification. *RT-Lab* is a software package from Opal-RT that supports this purpose. The *Real-Time Workshop* toolbox from Mathworks is applied for automatic code generation.

Figure 2.3 shows the overall constellation of the experiment environment. The environment consists of the host PC, the target PC and the motor test bench. On the host PC, the offline simulation and the automatic code generation is carried out. During the test bench experiment, the host PC functions also as the monitoring terminal. The host PC runs windows operating system. The designed algorithm runs on the PC target with QNX operating system. Through analog and digital I/O boards (PCI boards), the control algorithm can communicate with the hardware components on the motor test bench. Ethernet is used for the communication between the host and the target.
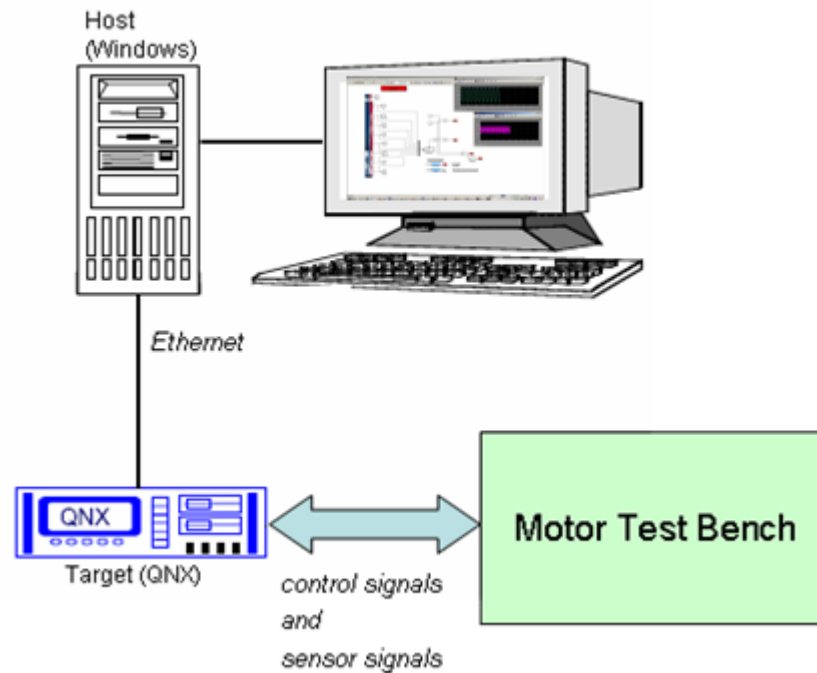
Figure 2.3: the constellation of the experiment environment.

The motor test bench consists of two electric drives of the same type, the power elec-
tronics (PCU), the sensors and the power supply. The electric drives are the same as
those in the brake actuator. One of them is the test object and the other produces
loading moment that simulates the loading condition in the brake actuator.

Details of the simulation environment will be introduced in the following sections.
The Simulink offline model is briefly described in section 2.2.2. The motor test
bench setup will be introduced in section 2.2.3. And the automated implementation
of the algorithm with RT-Lab will be introduced in section 2.2.4.

2.2.2 The Offline Simulation

The offline simulation is done with *Matlab/Simulink* to test the analytical design of
the fault tolerant control algorithm. The offline model simulates the control loop of a
single brake actuator with the fault tolerant solution. The structure of brake actuator
control and the offline model is illustrated in figure 2.4.

Figure 2.4: the structure of offline model.

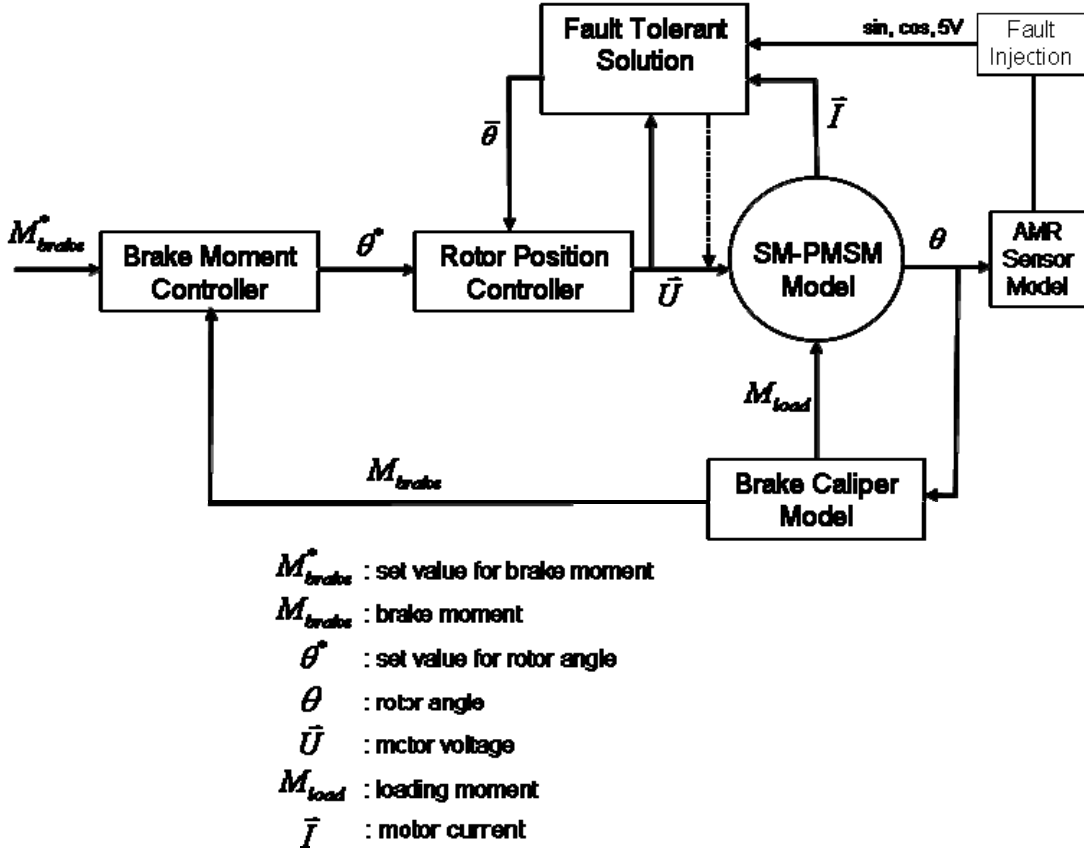The control loop of a brake actuator has a cascade structure. The outer loop controls the brake moment and produces an angular position set value for the position control loop. The position controller controls the motor to rotate to the desired angle so that the wedge is pushed/pulled to the proper position. And by this means, a controlled normal force is exerted on the brake disc to generate the required brake moment. The rotor position is measured directly by an AMR angle sensor mounted at the end of the rotor shaft. In the reality, the brake moment can not be measured directly. Actually a strain gauge is installed in the caliper to measure the elastic deformation of the brake caliper. And the brake moment is estimated from this measurement. But in the simulation, this is simplified as if the brake moment is directly measurable. The brake caliper model calculates the brake moment and the loading moment on the rotor shaft according to the rotor angle.

The control loop of a brake actuator itself is the inner cascade of the control of the whole brake system. And the control of the whole brake system is again the inner cascade of the control loop of the overall vehicle dynamics. But in this study, only the fault tolerant control of a brake actuator is relevant; and the behavior of the other outer control loops is not considered.

The brake moment controller is a simple PI-controller. The design of the position controller is explained in chapter 3, subsection 3.1.2. The fundamental frequency model of an SM-PMSM is used. The model is described mathematically by the voltage equation 3.3 and the mechanical equation 3.7 and 3.8. The brake caliper model is taken as black box from the project. The AMR sensor model consists of the conversion of the rotor angle in sine and cosine output. And the fault injection module produces additive errors on the signals from the AMR angle sensor model. Amplitude fault, offset fault, constant output and random fault (zero mean, gauss distributed) can be injected. Discussion on the relevant faults is made in chapter 4. And the design of the fault tolerant solution is explained in detail in chapters 3, 4 and 5.

The brake moment controller is not directly influenced by the AMR sensor measurement as shown in figure 2.4. If the fault effect of the AMR sensor could be handled within the position control loop, the brake moment control will not be disturbed. The study is therefore focused on the position control loop.

2.2.3 The Motor Test Bench and Its Control

The test bench experiment aims to validate the performance of the fault tolerant control with real actuator hardware. The online simulation setup is shown in the diagram in figure 2.5 schematically.

The SM-PMSM model and the AMR angle sensor model in the offline simulation are replaced by the real AMR angle sensor, the SM-PMSM motors, the power electronics (PCU) and the power supply modules. But the brake caliper model remains for the calculation of the loading moment on the rotor shaft. And the loading moment is produced by another SM-PMSM (loading machine), which is coupled with the SM-PMSM under test (test machine) mechanically. The experiment with a real brake caliper will require a rotating brake disc to simulate the self-strengthening effect. And to rotate the brake disc realistically as in a vehicle, a high power electric drive system is necessary. But the effort and cost to construct a hardware simulation system in such scale is not justified for the purpose of this study.

The fault tolerant control design is implemented on a QNX PC target. QNX is a commercial-off-the-shelf real time operating system. The control software communicates online with the actuator hardware through digital or analog I/O boards with PCI interface. The implementation detail can be found in section 2.2.4. The brake moment

control in the offline simulation is not implemented online, because the study is focused on the position control loop. Pre-determined rotor position set values are used for the online experiment.

The fault injection module produces additive error on the measurement signals from the AMR angle sensor. Amplitude fault, offset fault, constant signal and a random fault (zero mean, gauss distributed) can be injected. The fault type and fault parameters can be adjusted online from the host PC. The shut down of the motor is realized by setting the output of the position controller to zeros. The PWM generation function calculates the PWM patterns for the switching of the transistor elements in the DC/AC converter on the PCU.

For the control of the loading machine, a motor moment controller had been designed. It is a field-oriented closed-loop current controller. The design detail of the controller is not cited here. The phase currents are measured by LEM converters, which are also part of the PCU.
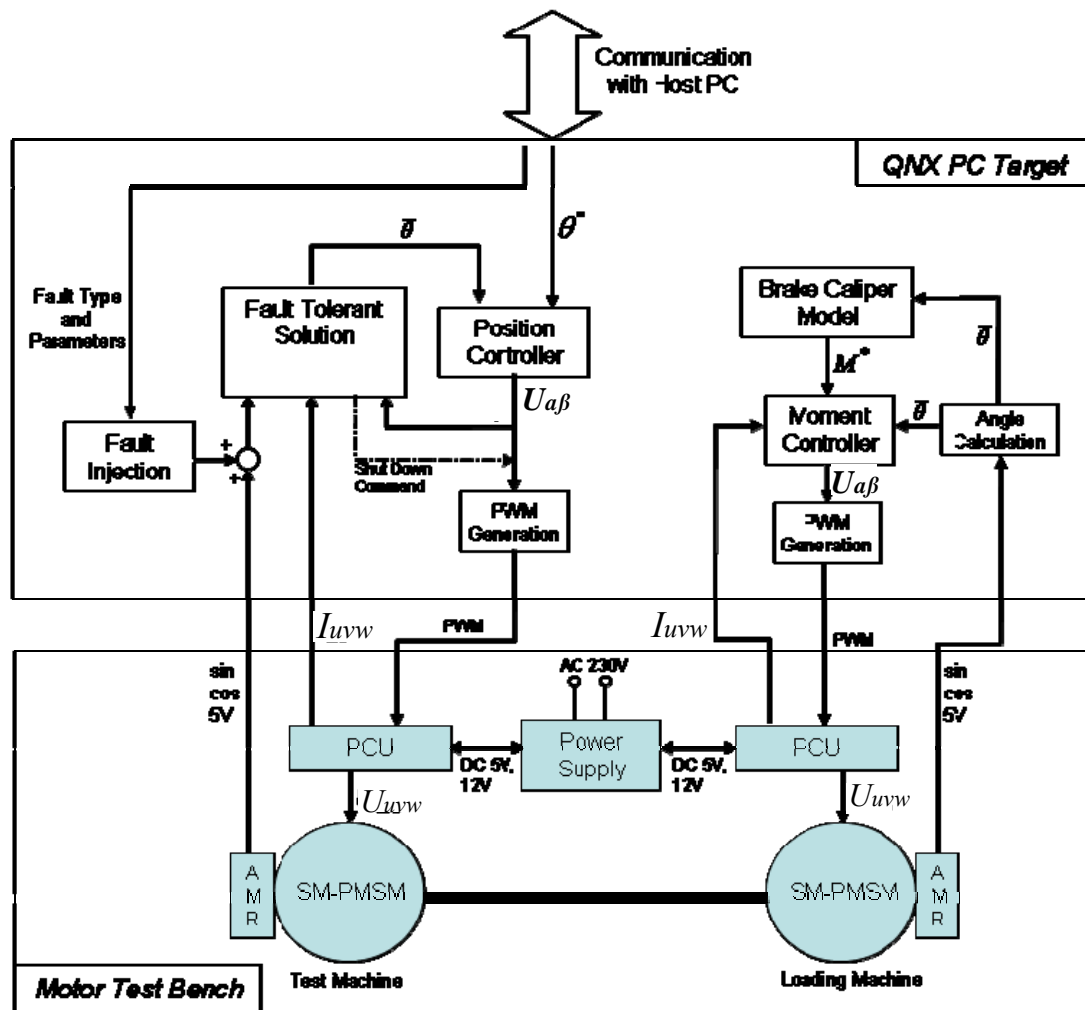
Figure 2.5: the motor test bench and its control with the QNX Target PC.

The power supply module consists of two individual voltage sources, the battery and the DC/DC converters. The voltage sources supply a constant voltage of 14 V, simulating the voltage of the 14 V vehicle power net. The DC/DC converters stabilize the 14 V voltage supply for the DC/AC converter circuit on the PCU (DC-link voltage of the bridge circuit) and also generate the stable 5 V supply for the other electronic elements on the PCU. The AMR sensors are also supplied by this power source. The battery is used as energy buffer. It also protects the voltage sources from overcharging during the generator operation of the motors.

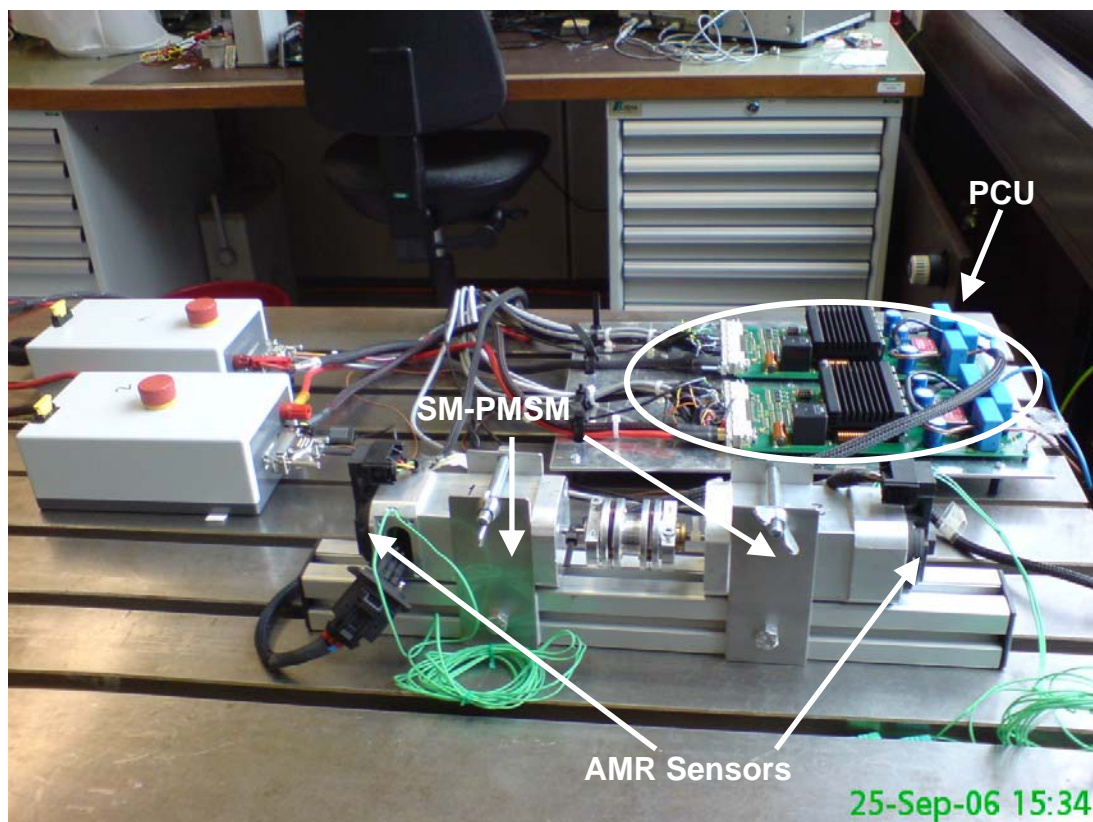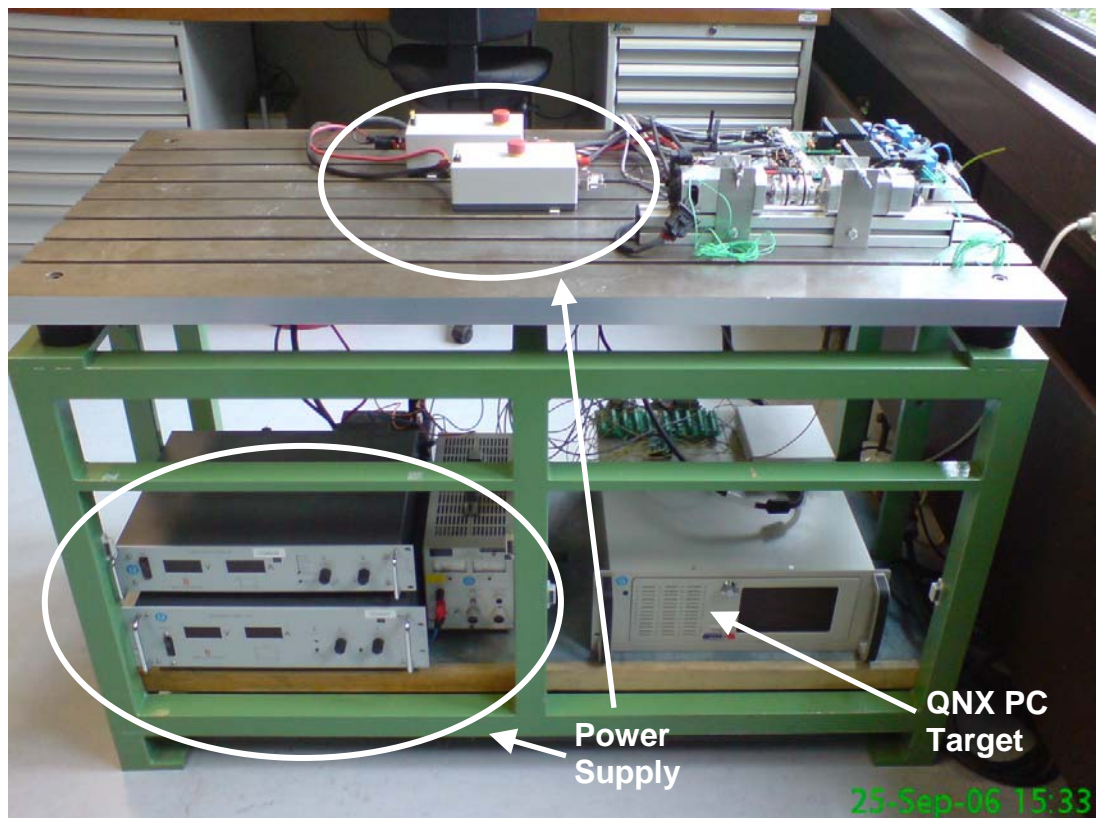Figure 2.6 shows the actual view of the motor test bench and the QNX PC target.

Figure 2.6: photos of the motor test bench and the QNX PC target.

2.2.4 The Automated Algorithm Implementation for Test Bench Experiment

The development of the control algorithm in general is a process with many iteration of modification. The implementation of the algorithm by manual coding is very time consuming. Structural change of the algorithm often leads to complete re-programming. Manual coding is also susceptible to human error. Detail knowledge of the real time computation platform is necessary. Automating the control implementation can greatly accelerate the development process, reduce the effort on time consuming coding and minimize the error caused by human programmer. For this purpose, an automated implementation system with the software tool *RT-Lab* from Opal-RT has been constructed.

RT-Lab is a software package for rapid prototyping of complex control systems and Hardware-in-the-Loop simulations. It supports a seamless process of automated algorithm implementation from Simulink model, the deployment of the algorithm on PC-cluster-based computation platforms and online monitoring as well as data logging. The Simulink model is used as front-end user interface for the online control. The work flow of the automated implementation with RT-Lab is shown in figure 2.7.

The starting point of the implementation is a Simulink model in which the algorithm is offline tested. For the automated implementation and deployment, some modification of the Simulink model is necessary. The model must be grouped into subsystems corresponding to the later distribution on the different computation platforms (host and targets). In our case, there are only two PCs, i.e. the Windows host and the QNX target. Therefore, the Simulink model is grouped into two subsystems as shown by the screenshot in figure 2.9. The *SC_Host* system remains on the host PC. And for the *SM_QNX* subsystem, C code will be generated and transferred to the QNX PC target. For communication between the host and the target, special communication block should be included in the model. The interfaces to the drivers of the I/O boards are integrated in the Simulink model in the form of C S-functions. An example is shown in figure 2.10. The C code of these interfaces will be automatically handled during the code generation with Real-Time Workshop.

RT-Lab automatically recognizes the Simulink subsystem for the target and applies the toolbox *Real-Time Workshop* from Mathworks to generate C code for the QNX target. Real-Time Workshop is an extension of capabilities of Simulink and Matlab that automatically generates, packages, and compiles source code from Simulink

models to create real-time software applications. The automatically generated C code is processor independent. The C code of the algorithm is transferred via Ethernet from the host to the QNX PC target.
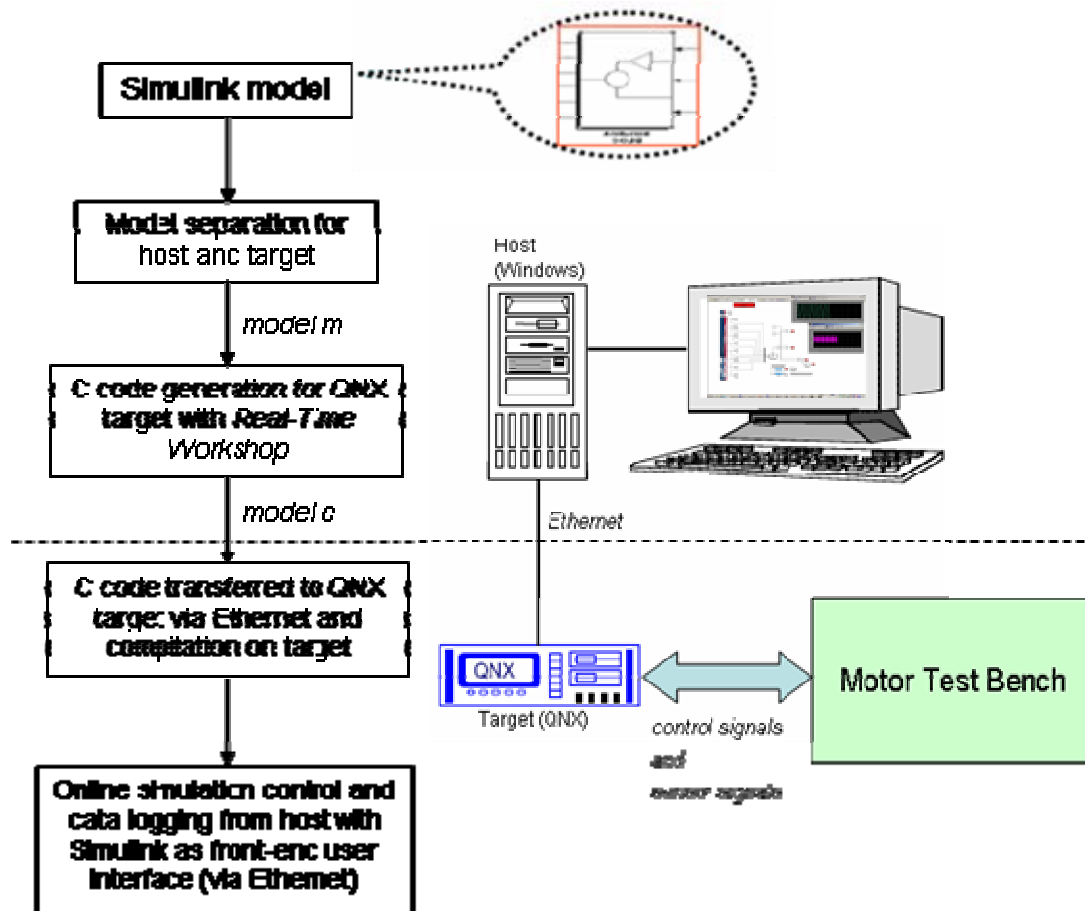
Figure 2.7: the work flow of the automated control implementation with RT-Lab and Real-Time Workshop.

The QNX PC target has a 3 GHz Intel processor. PC had been chosen as the real-time computation platform due to its enormous computation capacity and the flexible communication interface. The design of the fault tolerant control is not restricted by the computation power. Various types of commercial-off-the-shelf analog/digital I/O boards with PCI interface can be mounted in the PC target for the communication between the control algorithm and the hardware components of the motor test bench.

QNX is a real-time operating system for 'hard' real-time applications, i.e. application with very short sample time or high requirement on synchronization. It has a UNIX similar structure and is POSIX compatible. The QNX operation system allows a shortest interrupt processing time of 0.55 μs with a Pentium III processor. Compared to that, Windows NT 4.0 and other time-sharing operating system need at least 10ms

to react to events. With its fault tolerant design, pre-emptive multitasking and the runtime memory protection, QNX provides a very stable foundation for the implementation of hard real-time applications. The C code of the algorithm is compiled on the QNX PC target into an executable with GNU compiler collection (gcc).

The executable, i.e. the control algorithm and the other control functions for the motor test bench, can be started and killed as a user process of QNX from the host PC via the Ethernet. The smallest sampling time of the designed control algorithm is 100 μs. The synchronization of all the I/O boards at this sampling rate is realized with a timer, which triggers a square wave signal with a period of 100 μs. The interesting signals for online monitoring and data logging will be sent from the target to the host also through Ethernet. Online parameter modification via Ethernet is also possible. The subsystem in the Simulink model for host PC is used as the front-end user interface for online monitoring and parameter tuning from the host PC. Figure2.8 shows an example of this subsystem in the experiment.
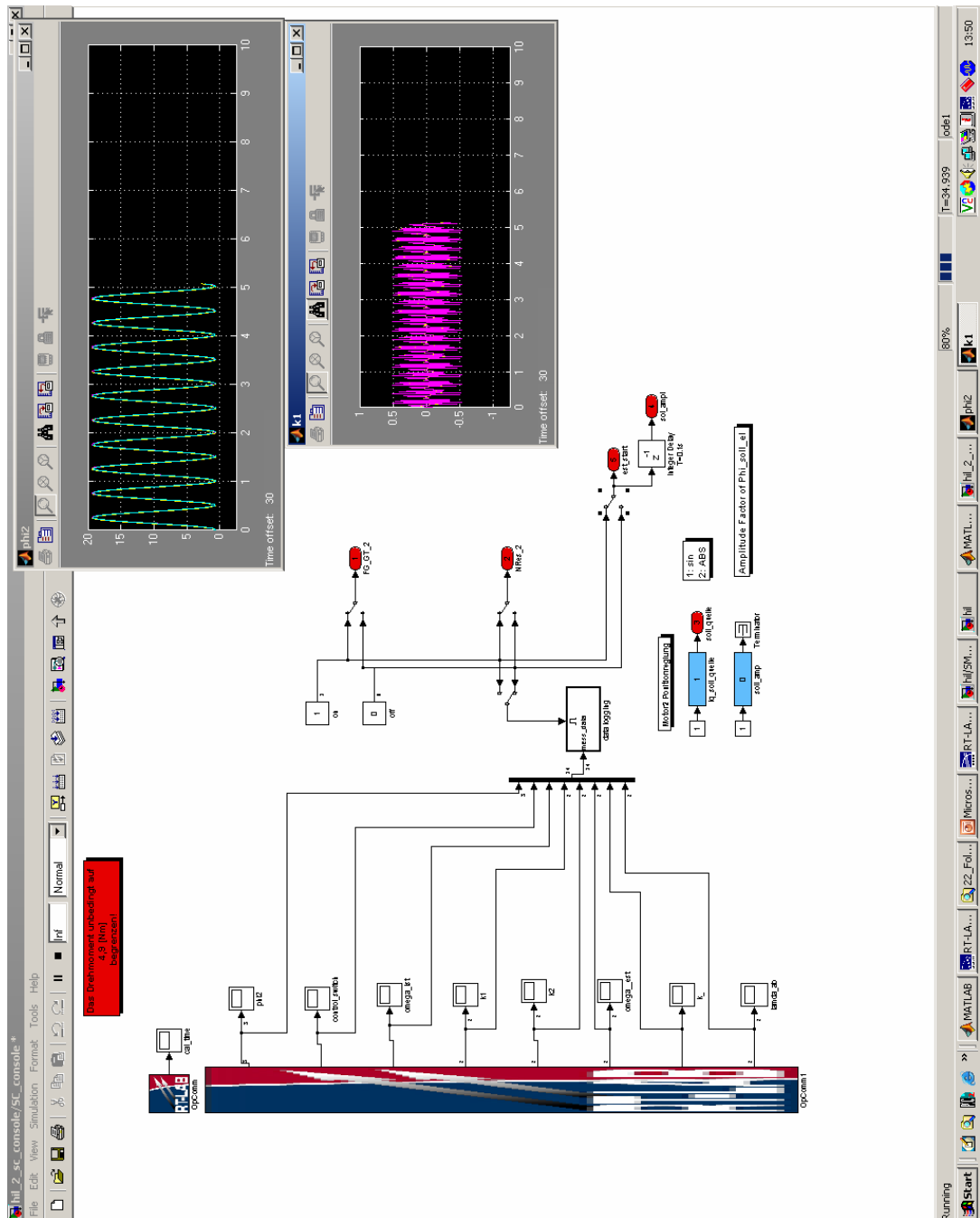
Figure 2.8: an example of the subsystem in the Simulink model for online monitoring and parameter tuning from host.

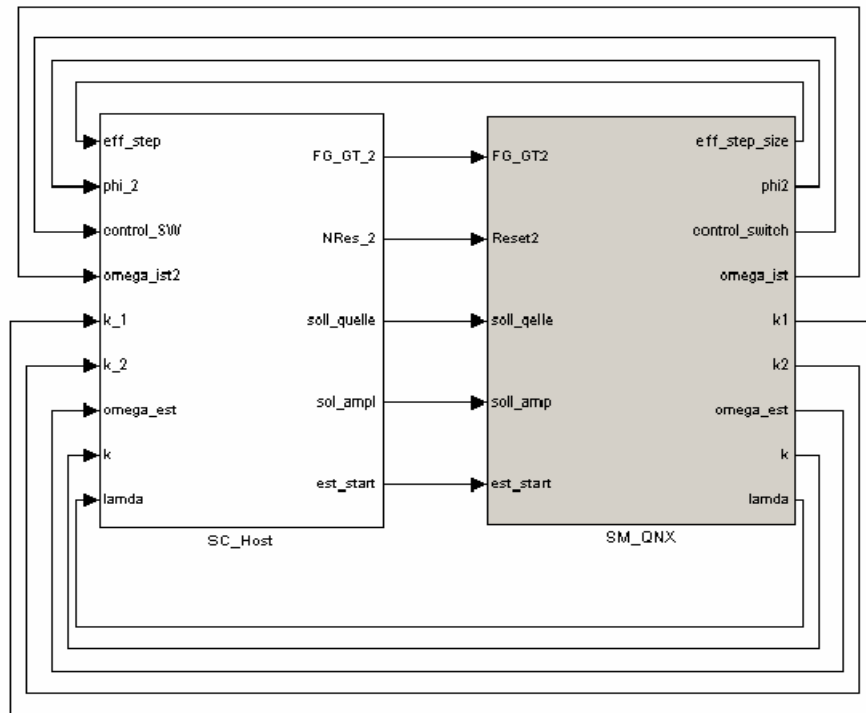**Figure 2.9: an example of the grouping of the Simulink model on the top level for the automated control implementation. The SC_Host subsystem remains on the host PC. And C code will be generated for the SM_QNX subsystem and transferred to the QNX PC target.**
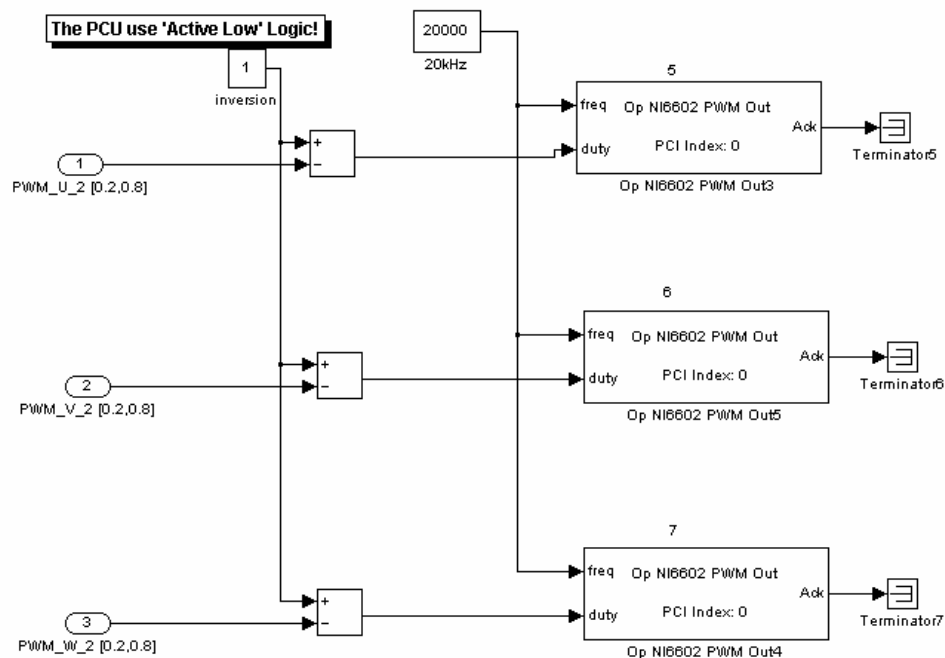

Figure 2.10: an example of the interfaces to the drivers of the I/O boards that are integrated in the Simulink model as C S-functions.

Chapter 3

The Fault Tolerant Control Scheme

In this chapter, the fault tolerant control design of the brake actuator against AMR angle sensor fault is presented. The brake actuator control consists of two cascaded control loops as illustrated in figure 2.4; i.e. the outer loop of brake moment control and the inner loop of motor position control. The fault effect of AMR angle sensor has direct impact on the position control loop. If the position control fails, the brake moment control is not possible. Therefore, the problem is actually the fault tolerant position control of the SM-PMSM. The section 3.1 introduces the knowledge of surface-mount permanent magnet synchronous machine (SM-PMSM), its position control and the work principle of the AMR angle sensor. In section 3.2, an overview of the fault tolerance techniques and fault tolerant control is provided first. And then the proposed fault tolerant position control scheme of the SM-PMSM will be presented.

3.1 The Position Control Loop of the SM-PMSM in the Brake Actuator

This section aims to explain the motor position control loop in the brake actuator. For a better understanding of the position control, the fundamental-frequency machine model of SM-PMSM is first explained. The new position control design is then presented in sub-section 3.1.2. At the end the AMR angle sensor is introduced as background knowledge for the later analysis on the fault behavior of such sensor.

3.1.1 SM-PMSM and the Machine Model

3.1.1.1 Surface-mount Permanent Magnet Synchronous Machine (SM-PMSM)

Permanent magnet synchronous machines (PMSM) are 3-phase synchronous machine in which the excitation field is produced by permanent magnet. Although such machines are generally more expensive than asynchronous induction machines, this machine type is widely used in automotive systems due to its high power density. The cross-sections of several typical constructions of PMSM are shown in figure 3.1 schematically.

The stator of a synchronous machine consists of a stack of laminated ferromagnetic core with internal slots, a set of three-phase distributed stator windings placed in the slots, and the housing and bearing for the rotor shaft. The cross-section of the rotor can be salient or cylindrical. Salient here means the protruding poles (figure 3.1 a). The permanent magnet can be surface mounted or buried in the rotor. The type of construction in the current brake actuator design is the cylindrical rotor with surface-mount permanent magnet, which is shown in figure 3.1c). This type of machine shows the least saliency because ideally the magnetic resistance is the same in any radial direction.

a) salient rotor construction   b) cylindrical rotor with buried magnet

c) cylindrical rotor with surface-mount magnet (SM-PMSM)
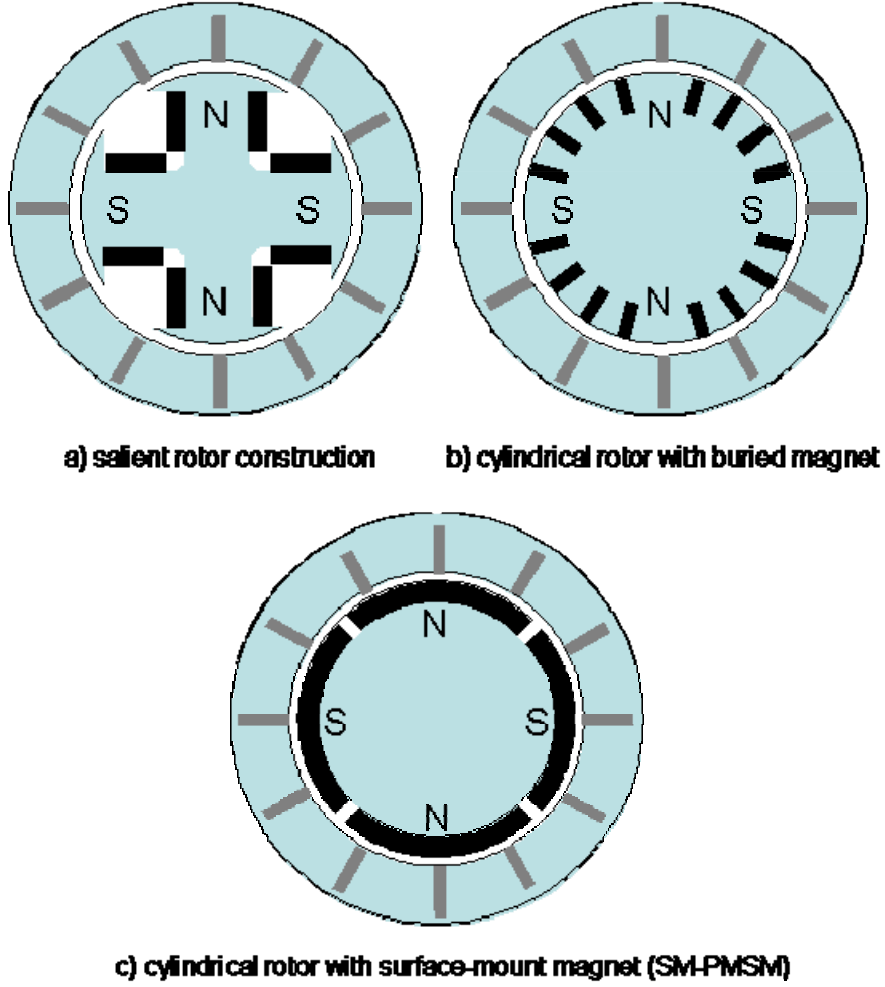
Figure 3.1: different constructions of permanent magnet synchronous machine

Normally there are more than one pole pairs in a SM-PMSM so that the realization of larger motor moment with smaller current is possible. Figure 3.2 compares the ideal layouts of SM-PMSM with one pole pair and two pole pairs. Machines with Z_p pole pairs can ideally be considered as 'pressing' Z_p single-pole-pair machines spatially together into one machine while keeping the magnet flux of each permanent magnet pole pair unchanged. Therefore the total motor moment of this machine can be calculated by:

$$M_{mech} = Z_p \cdot M_{el} \tag{3.1}$$

where M_{mech} is the total motor moment and M_{el} is the moment produced by one equivalent single-pole-pair machine. The motor in use has two pole pairs, i.e. four poles. In the later discussion, the analysis on this machine is carried out with one of its equivalent single-pole-pair machines. And all the quantities of this single-pole-pair machine are annotated with the subscription *el*, i.e. electrical; and the quantities

of the machine in use are specified by the subscription *mech*, i.e. mechanical. Since the equivalent single-pole-pair machines are spatially 'pressed together', the following relation between the rotation angles is valid:

$$\theta_{el} = Z_p \cdot \theta_{mech} \tag{3.2}$$

$$Z_p = 1 \qquad\qquad Z_p = 2$$
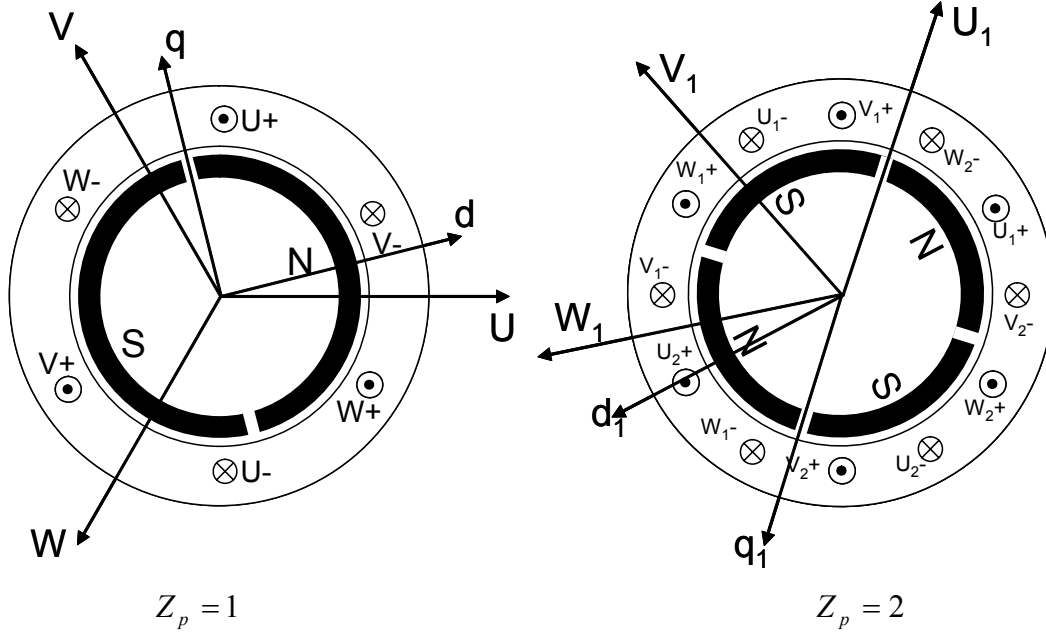
Figure 3.2: comparison of SM-PMSM with one pole pair and two pole pairs.

In figure 3.2, the 3-phase U-V-W coordinate system and the rotor synchronous d-q coordinate system are also drawn. The definition of these coordinate systems is introduced in appendix A. The angular 'compression' of the coordinates in the machine with two pole pairs can be seen in the figure.

3.1.1.2 The Fundamental Frequency Machine Model of SM-PMSM

The derivation of the fundamental frequency machine model is not cited here. The model is called fundamental frequency model because the distribution of the rotor magnet flux is assumed to be sinusoidal. The voltage equation of an SM-PMSM in the d-q coordinate system is:

$$\begin{pmatrix} U_d \\ U_q \end{pmatrix} = \begin{pmatrix} L_d & 0 \\ 0 & L_q \end{pmatrix} \begin{pmatrix} \dfrac{di_d}{dt} \\ \dfrac{di_q}{dt} \end{pmatrix} + \begin{pmatrix} R & -\omega_r L_q \\ \omega_r L_d & R \end{pmatrix} \begin{pmatrix} i_d \\ i_q \end{pmatrix} + \begin{pmatrix} 0 \\ \omega_r \Psi_{pm} \end{pmatrix} \tag{3.3}$$

For SM-PMSM the inductance in d- and q-direction are very similar if magnetic saturation is ignored. This means:

$$L = L_d = L_q \tag{3.4}$$

With this assumption, the voltage equation can be expressed in α-β coordinate system as:

$$\begin{pmatrix} U_\alpha \\ U_\beta \end{pmatrix} = \begin{pmatrix} L & 0 \\ 0 & L \end{pmatrix} \begin{pmatrix} \dfrac{di_\alpha}{dt} \\ \dfrac{di_\beta}{dt} \end{pmatrix} + \begin{pmatrix} R & 0 \\ 0 & R \end{pmatrix} \begin{pmatrix} i_\alpha \\ i_\beta \end{pmatrix} + \begin{pmatrix} -\omega_r \Psi_{pm} \sin\theta_d \\ \omega_r \Psi_{pm} \cos\theta_d \end{pmatrix} \tag{3.5}$$

The general equation to calculate the motor moment is:

$$M_{mech} = Z_p \cdot M_{el} = \frac{3}{2} Z_p \cdot \left| \vec{\Psi}_{pm} \times \vec{I}_s \right| \tag{3.6}$$

where $\vec{I}_s$ is the stator current vector. In the case of SM-PMSM the equation can be simplified as:

$$M_{mech} = \frac{3}{2} \cdot Z_p \cdot \Psi_{pm} \cdot I_q \tag{3.7}$$

where I_q is the projection of the stator current vector $\vec{I}_s$ on the q-axis. The mechanical motion of the rotor is described by the following equation:

$$J \cdot \dot{\omega}_{mech} = M_{mech} - M_{load} \tag{3.8}$$

where M_{load} is the loading moment on the rotor shaft and J is the inertia of the rotor.

3.1.2 The Position Controller Design

Two quantities determine the mechanical motion: the motor moment M_{mech} and the loading moment M_{load}. Since the loading moment is often unknown, the control of

the motion of a SM-PMSM is based on the control of the motor moment. And according to equation 3.7, the motor moment is linearly proportional to the amplitude of the q-component (I_q) of the stator current vector. The d-component (I_d) of the stator current vector produces no torque but a magnetic field overlapped on the permanent magnet field. If field weakening operation is not considered, the effective way to generate motor moment while minimizing energy consumption and current is to force I_d to zero and control I_q to follow the set value, which is proportional to the desired motor moment. This is the basic idea of field oriented control.

The field oriented control enables the separation of the SM-PMSM motion control into an inner cascade of current (moment) control and outer cascades of rotor motion control (speed or position) as shown in figure 3.3 a). And the control delay time constant of the inner cascade should be much smaller than the outer cascade. There are many different approaches for field-oriented current control, a good overview is provided in [2]. Among these approaches, the multi-variable state-space controller provides the best performance regarding the current response dynamics and the transient oscillation [2]. But for applications with lower requirement on the dynamics of the current response, open-loop current control with decoupling network is simpler and does not need current measurement. The structure of these control methods are shown in figure 3.3 b) c). The decoupling network is basically a transformation of equation 3.3 by ignoring the derivative of the current:

$$\begin{pmatrix} U_d^* \\ U_q^* \end{pmatrix} = \begin{pmatrix} R & -\omega_r L_q \\ \omega_r L_d & R \end{pmatrix} \cdot \begin{pmatrix} i_d^* \\ i_q^* \end{pmatrix} + \begin{pmatrix} 0 \\ \omega_r \Psi_{pm} \end{pmatrix} \tag{3.9}$$

The superscript '*' in equation 3.9 indicates the control set values. The multi-variable state-space current control will not be discussed here. More details of it can be found in [2].
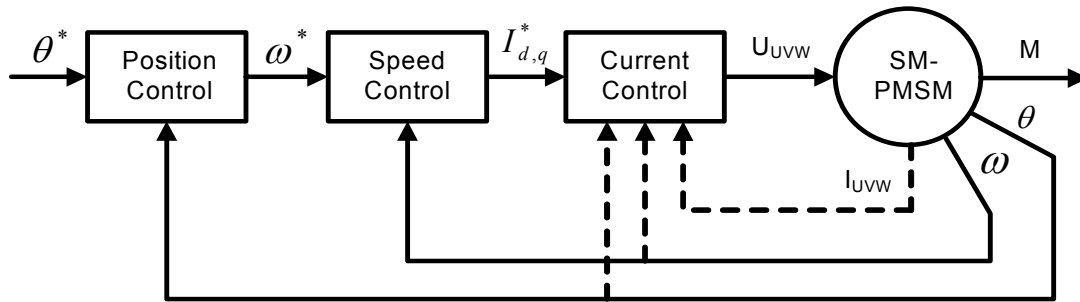
a) The cascaded structure of the control of SM-PMSM.
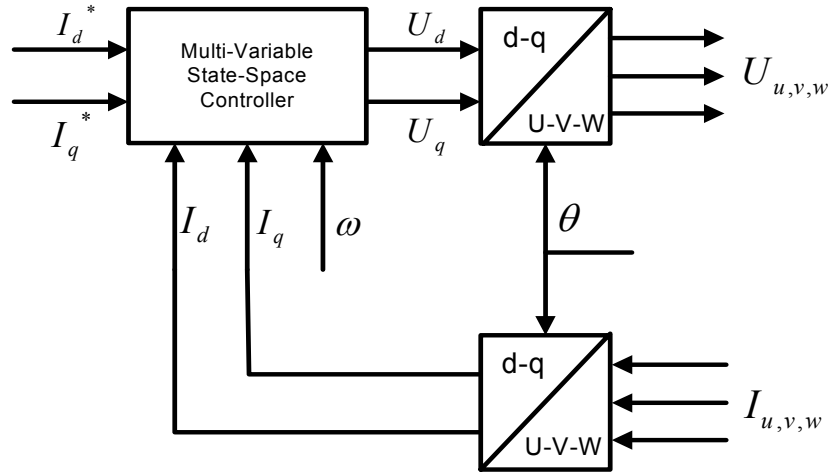
b) The multi-variable state-space current control loop.
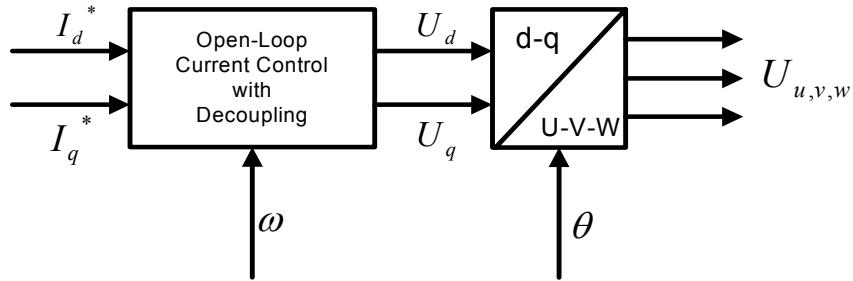
c) The open-loop current control with decoupling network.

Figure 3.3: the control structure of SM-PMSM.

The cascade structure of the position control shown in figure 3.3 a) with closed-loop speed control and closed-loop current control has some drawbacks. Due to the restriction that the outer loop should have much slower control response than the inner loop for stability reason, the response promptness of the position control is limited. The controller parameter tuning for three control loops is very time consuming. Therefore, a new position controller design is proposed. The speed control loop is removed and open-loop current control is applied. The structure of the new position control is depicted in figure 3.4. The sampling time of the control loop is 2.5ms. The position controller is first designed with continuous system equations and then approximated with the Euler method in the discrete system.
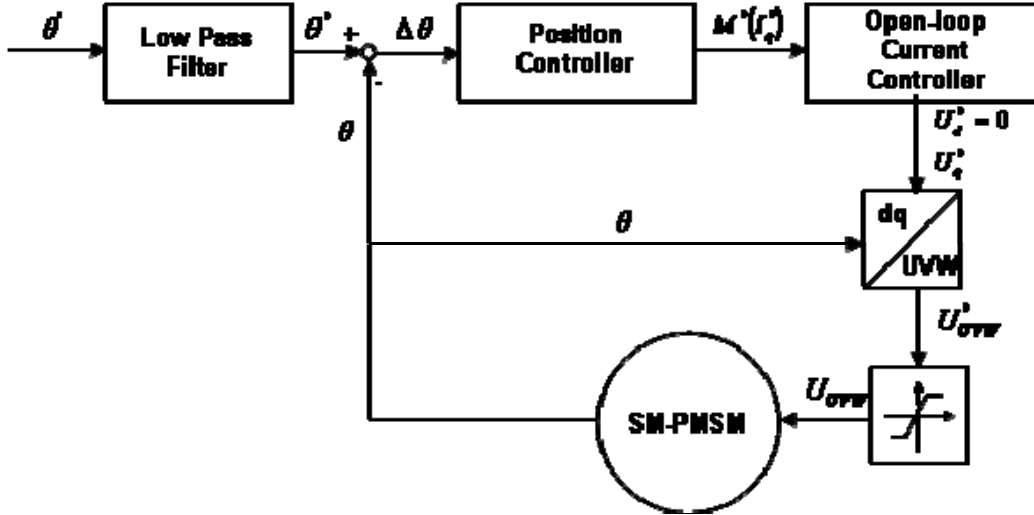
Figure 3.4: the structure of the new position control loop. The sampling time is 2.5ms.

The position controller should eliminate the position deviation $\Delta\theta$ by generating a proper set value of motor moment. The design of the position controller is based on the mechanical model (equation 3.8) of the motor:

$$\Delta\dot{\theta} = \omega^* - \omega_r$$
$$\dot{\omega}_r = \frac{1}{J}(M^* - M_L)$$

(3.10)

In which M^* is the set value of motor moment and M_L is the unknown loading moment. ω^* is the set value of the rotor speed that is calculated from the rotor angle set value. An intermediate control variable is constructed as follow:

$$v = a_0 \cdot \Delta\theta + a_1 \cdot \Delta\dot{\theta}$$

(3.11)

where $a_1 \neq 0$. The goal is to make $v = 0$ with proper control, then the following equation holds

$$\Delta\dot{\theta} = -\frac{a_0}{a_1} \cdot \Delta\theta$$

(3.12)

And as long as $a_0/a_1 > 0$, $\Delta\theta$ will converge to zero. And the bigger a_0/a_1 is, the faster $\Delta\theta$ vanishes. By differentiating both sides of equation 3.11, we obtain:

32

$$\dot{v} = a_0 \cdot \Delta\dot{\theta} + a_1 \cdot \Delta\ddot{\theta} = a_0(\omega^* - \omega_r) + a_1(\dot{\omega}^* - \frac{1}{J} \cdot M^* + \frac{1}{J} \cdot M_L) \qquad (3.13)$$

To force v to converge to zero, the same approach is applied again. Let:

$$\dot{v} = -k \cdot v \qquad (3.14)$$

By assigning a large positive value to the parameter k, v will converge to zero quickly. Comparing the right hand side of equation 3.13 and 3.14 we obtain the following expression for the set value of motor moment:

$$M^* = J\dot{\omega}^* + M_L + \frac{a_0}{a_1} \cdot k \cdot J \cdot \Delta\theta + \frac{J}{a_1}(a_0 + a_1 k)(\omega^* - \omega_r) \qquad (3.15)$$

Assuming $\omega^* - \omega_r \approx 0$ in average; the set value of motor moment can be calculated by:

$$M^* = J\dot{\omega}^* + M_L + \frac{a_0}{a_1} \cdot k \cdot J \cdot \Delta\theta = J\dot{\omega}^* + M_L + K\Delta\theta \qquad (3.16)$$

This controller design is inspired by the idea of the sliding-mode control. Equation 3.12 describes the dynamic behavior of the control deviation on the sliding manifold, on which the control deviation will automatically converge to zero. This sliding manifold is defined by $v = 0$. The control variable M^* forces the system to stay on the sliding manifold. Equation 3.16 has a very clear physical meaning. If $\Delta\theta = 0$, the motor moment should overcome the loading moment M_L and accelerate the rotor at the set value of acceleration $\dot{\omega}^*$ which is calculated from the rotor position set value θ^*. If $\Delta\theta \neq 0$, i.e. there is a position control deviation, an extra motor moment should be added to compensate this. And the factor $K = a_0 \cdot k \cdot J / a_1$ determines how fast the deviation is eliminated. This factor is chosen during the parameter tuning. The unknown loading moment is considered as disturbance and will be overcome by large control gain K.

The open loop current controller calculates the corresponding voltage set value $\left(U_d^*, U_q^*\right)$ with equation 3.9. Note that the numerical value of the inductance of our motor is very small (10^{-6} H) and $I_d^* \equiv 0$; hence the calculation of the voltage set value can be further simplified as:

$$U_d^* = 0$$
$$U_q^* = R \cdot I_q^* + \omega_r \Psi_{pm} \approx N \cdot M^* \qquad (3.17)$$
$$= N \cdot (J\dot{\omega}^* + K\Delta\theta)$$

where N is another gain factor to be tuned. With large control gain K the loading moment can be compensated; but this also leads to strong current peak if the position control deviation $\Delta\theta$ is big. Fast rotor acceleration can also results in such current peak. Therefore, a low pass filter is added to smoothen the variation of the position control set value (figure 3.4).

There are only two parameters to be tuned during the implementation, namely K and N. From equation 3.14, it is trivial that the intermediate variable v will converge to $v=0$ as long as K is positive. And if $v=0$, the position deviation $\Delta\theta$ is also stable at $\Delta\theta = 0$. The response promptness of the position control is actually determined by the low pass filter. This further simplifies the parameter tuning. The tuning of the parameter N and K is a compromise between fast elimination of the angle deviation and acceptable overshoot. The both parameters are first tuned with the offline model and then implemented on the test bench with further fine tuning. Some experiment results on the position control performance can be found in chapter 6. The simulation results are presented in figure 3.5 a) and b).
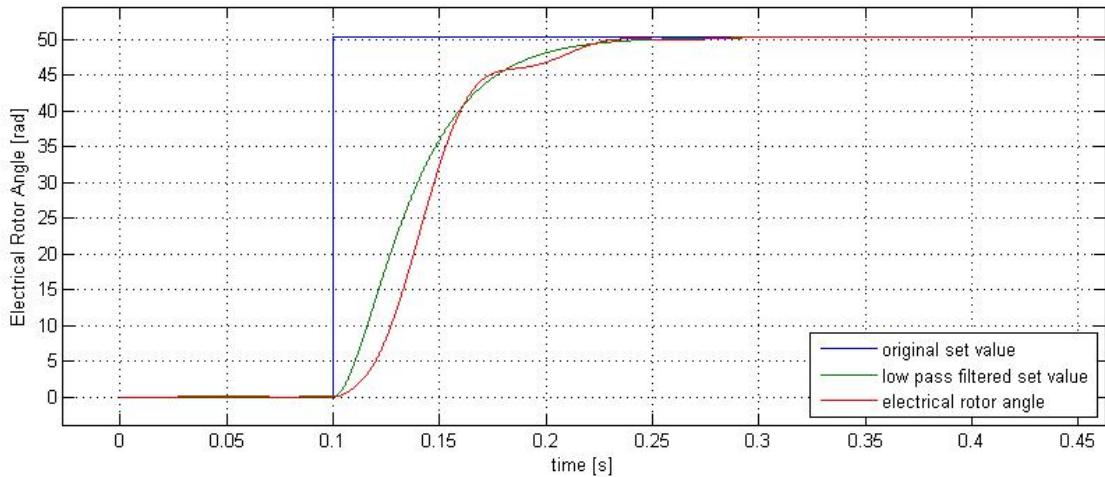
a)
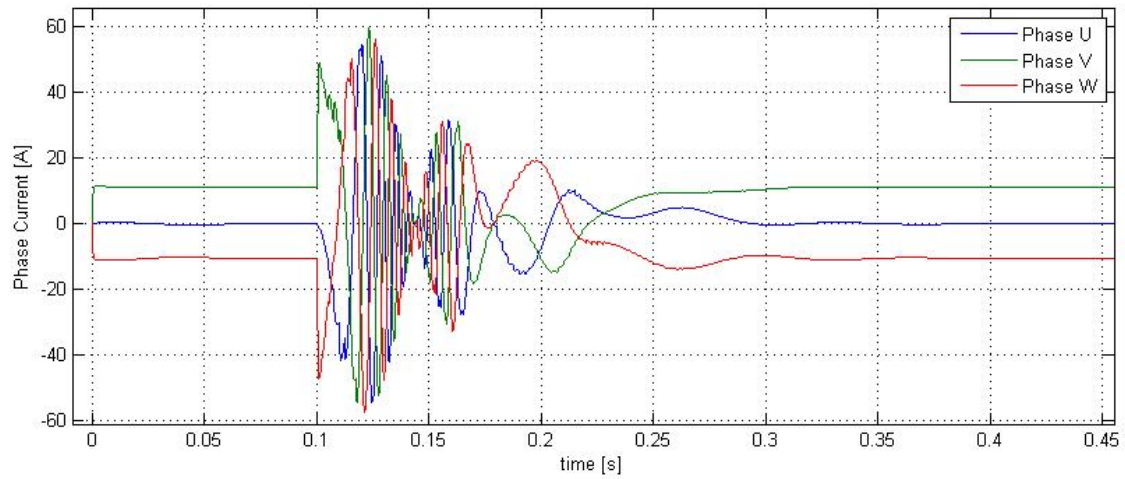
b)

Figure 3.5: the simulation results of the position controller. The loading moment is
constantly 0.15 Nm. Figure a) is the comparison of the electrical position
set values and the electrical rotor position. Figure b) is the simulated phase
current.

In figure 3.5, it can be seen that the control dynamic is actually determined by the low-pass filter. The green curve in figure 3.5 a) shows the 'smoothened' angle set value. The low-pass filter is a first-order delay element. Its time constant is determined so that the smoothened curve reaches 95% of the original set value at 100ms delay. Fast angle error elimination with large gain factor K will also strengthen the overshoot and hence result in big current peak. The overshoot can be reduced by choosing smaller controller parameters N and K. Figure 3.5 b) shows the phase currents. The current peak is reduced to smaller than 60 A per phase.

3.1.3 The AMR Angle Sensor

The Anisotropic Magneto-Resistive (AMR) angle sensor is commonly used today due to its advantage of contact-free measurement. The Anisotropic-Magneto-Resistive effect is the property of a current carrying magnetic material to change its resistance according to the orientation of an external magnetic field. Figure 3.6 shows a strip of such ferromagnetic material, e.g. perm-alloy.
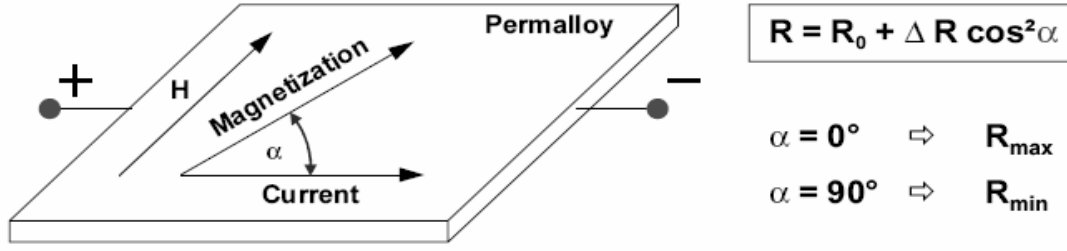
Figure 3.6: the magneto-resistive effect [19].

The resistance of the material depends on the angle between the internal magnetization direction and the direction of current. If an external magnetic field *H* is applied parallel to the plane, the internal magnetization direction of the material will be influenced. And if the external field is strong enough to saturate the material, it can be assumed that the internal magnetization direction is almost aligned with the external field. As a result, the resistance R of the material will change as a function of the rotation angle α of the external field (figure 3.6), as given by:

$$R = R_0 + \Delta R_0 \cos^2 \alpha \qquad (3.18)$$

where R_0 and ΔR_0 are material constant.. By measuring the change of the resistance, the angle of the external field can be determined. The setup of an AMR angle sensor is schematically shown in figure 3.7. A small piece of permanent magnet is mounted at the end of the rotor shaft. The sensor element is axially aligned to the magnet and fixed by plastic housing. In this setup, the orientation of the external field corresponds to the rotor angle.
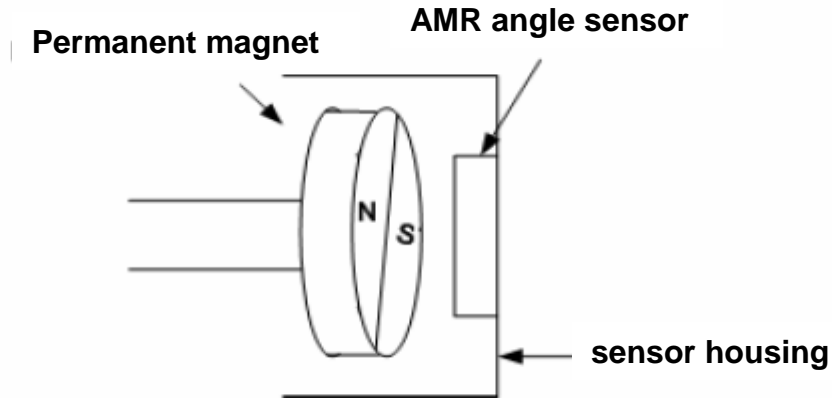
Figure 3.7: basic arrangement of sensor and magnet for contact-less angle measurement

The change of the resistance is measured with a Wheatstone bridge shown in figure 3.8. From equation 3.18, it is clear that with the measurement of one resistance the angle can only be unambiguously determined in a $\pi/2$-wide range. But if two Wheatstone bridges of the same type are used and placed with a 45 degree offset (figure 3.8); the outputs of the two Wheatstone bridges are proportional to $\sin 2\alpha$ and the $\cos 2\alpha$ respectively. And hence α can be determined in a π-wide range.
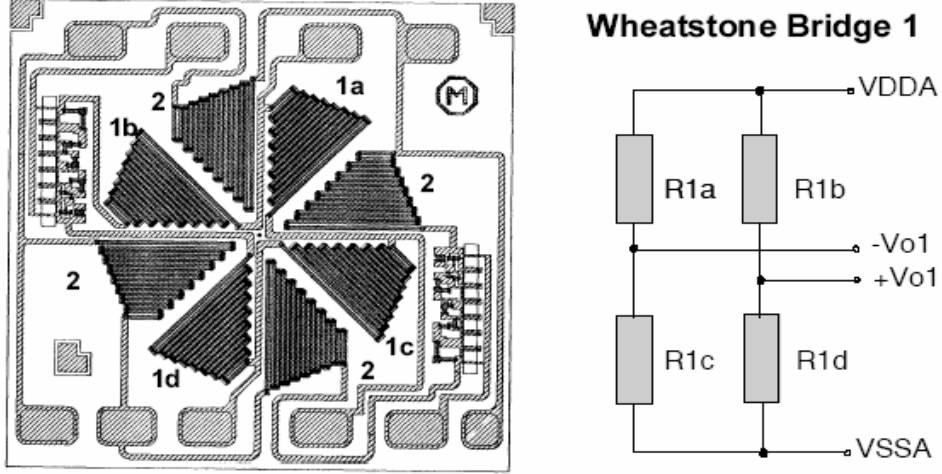
Figure 3.8: layout of an integrated AMR sensor and the Wheatstone-Bridge [19].

The outputs from the two Wheatstone bridges are amplified and offset by a signal conditioning circuit (figure 3.9). The signal conditioning circuit is integrated with the bridge circuits in one chip. Therefore, the outputs of the sensor are:

- $A_s \sin 2\alpha + U_b / 2$;
- $A_c \cos 2\alpha + U_b / 2$;

where A_s and A_c are the amplification factors of the sine and cosine channels; U_b is the supply voltage of the sensor. In fault-free operation, A_s and A_c should be equal and U_b should be 5V.

To calculate the angle from the output signals, the following equation is applied:

$$\alpha = \frac{1}{2} \arctan\left(\frac{A_s \cdot \sin 2\alpha}{A_c \cdot \cos 2\alpha} \right) \tag{3.19}$$

The offset is compensated by measuring the supply voltage U_b. The *arctan* operation can only provide a unique solution within an interval with the width π, e.g. $(-\pi/2, \pi/2)$; if the angle runs over the boundary, a 'jump' will appear in the calculated angle. But since the maximal angular velocity of the motor is limited, such 'jumps' in the calculated angle can be detected and corrected.
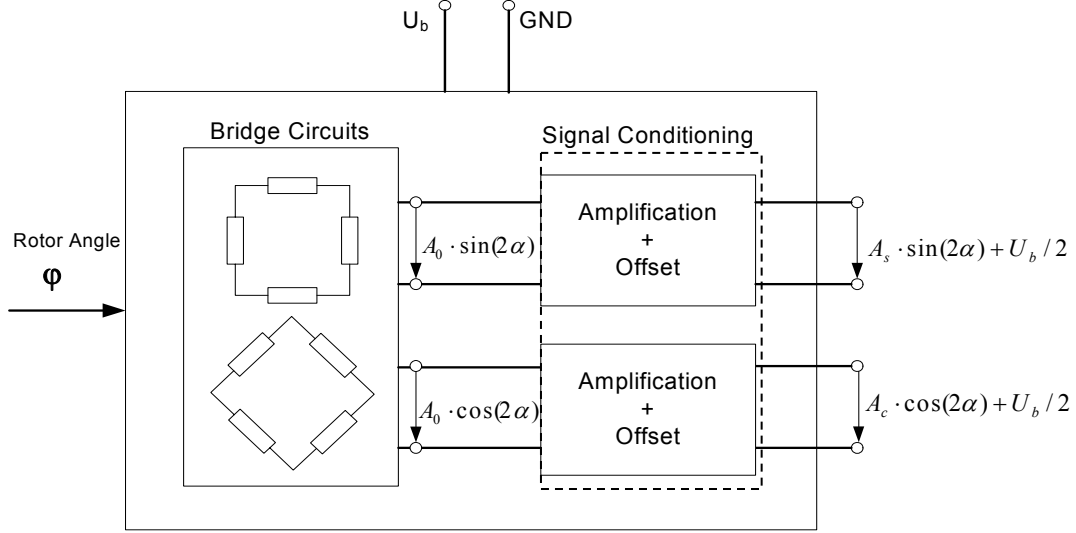
Figure 3.9: the block diagram of the AMR sensor.

3.2 The Proposed Fault-Tolerant Control Scheme against AMR Sensor Fault

In this section, the proposed position fault-tolerant control scheme for the SM-PMSM against AMR sensor fault is introduced. The first subsection introduces the concept of redundancy and provides arguments for the choice of analytical redundancy (software solution) for the fault tolerance. The second subsection provides an overview of the fault-tolerant control techniques. The proposed fault-tolerant scheme will be explained in the last subsection 3.2.3.

3.2.1 The Concept and Choice of Redundancy

The common measure to realize fault tolerance is *redundancy*. Redundancy is the existence of more than one means for performing a required function in an item [7]. Redundancy can be created by simply duplicating the hardware (physical redundancy) or be realized by software solution (analytical redundancy). From the operat-

ing point of view, redundancies can be categorized into active, warm and standby re-dundancy [7]:

1. *Active Redundancy* (parallel, hot): redundant elements are subjected from the beginning to the same load as operating elements, load sharing is possible.
2. *Warm Redundancy* (lightly loaded): redundant elements are subjected to a lower load until one of the operating element fails, load sharing is also possible.
3. *Standby Redundancy* (cold, non-loaded): redundant elements are subjected to no load until one of the operating element fails, no load sharing is possible.

To avoid common mode failures, redundant elements should be realized independently from each other. This independency could range from the function design, the location to the manufacturing of the elements.

In the case of the AMR angle sensor in a brake actuator, the most intuitive possibility of redundancy would be using *duplicated* AMR angle sensors to measure the rotor angle, i.e. a physical redundancy. To avoid common mode failure, the redundant AMR sensors should *not* be placed together. Due to the special spatial configuration of AMR angle sensor shown in figure 3.7, it is then only possible to put the AMR sensors at both ends of the rotor shaft. This makes it very difficult to integrate the AMR elements on the same PCB as the signal processing unit. The increase of production cost would be significant due to the extra electrical connections. Also restrictions will be posed on the mechanical construction of the brake actuator to provide a stable fixation and housing of the extra AMR elements and their electrical connections. This could lead to a higher production cost of the mechanical parts. And for mass production in the automobile industry, such cost raise can sum up to a huge amount.

Through sophisticated software functions, analytical redundancy extracts or estimates the missing information from information provided by other hardware components in the system or internal values of the control system. For AMR angle sensor, this means the estimation of the rotor angle with motor current and voltage. The estimated rotor angle can be used for fault detection or fault tolerant control. Analytical redundancy is basically a software solution. It will not increase production cost and poses little restriction on the system design. Therefore, analytical redundancy is the preferred solution.

3.2.2 Fault Tolerant Control Techniques

Fault tolerant control is a control system that can accommodate system component faults and is able to maintain stability and acceptable degree of performance not only when the system is fault-free but also when there are component malfunctions [4]. Fault tolerant control can be classified into two categories: passive fault tolerant control and active fault tolerant control [5]. Figure 3.10 illustrates the classification of fault tolerant control system.
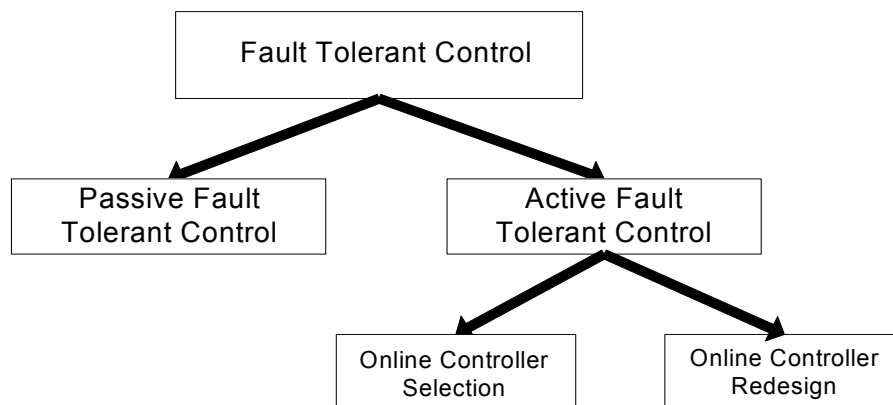
Figure 3.10: classification of fault tolerant control. The diagram is taken from [4]

The passive fault tolerant control is an approach to design the control according to anticipated fault events. These faults are simply tolerated by a robust controller design. Passive fault tolerant control treats the faults as if they were sources of modeling uncertainty. However, the main drawback of a passive fault tolerant control is that as the number of potential failures and the degree of system redundancy increase, controller design could become very complex. And a single fixed controller that needs to deal with different situations associated with all possible failure conditions can hardly be optimal for operation in any of the scenarios. Further more, the stability and performance of the controller is unpredictable if unanticipated failure occurs. Such drawback for passive fault tolerant control is the main motivation for developing active fault tolerant control.

The active fault tolerant control relies on the fault detection and identification (FDI) process to monitor the fault events and determines what change should be made to the controller. The active fault tolerant control process can be separated into two steps: the FDI; and the controller reconfiguration. The process is depicted schematically in figure 3.11.
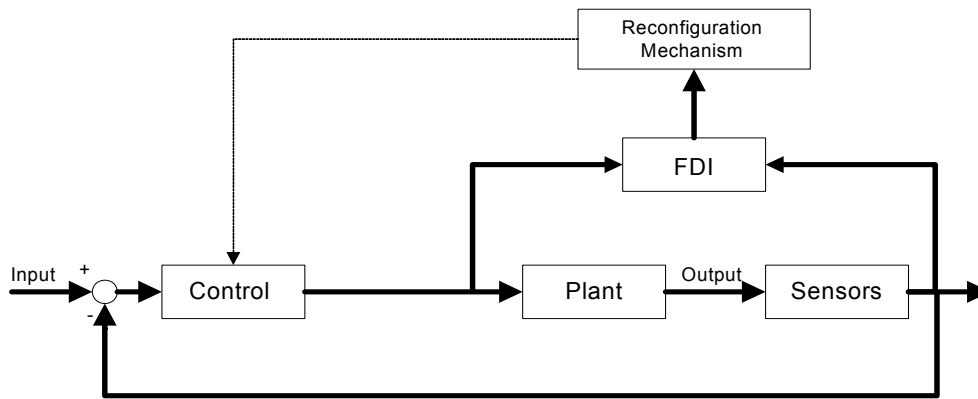
Figure 3.11: the process of active fault tolerant control.

The fault detection and identification can be signal-based or model-based [6]. The general schemes of signal-based and model-based fault detection and identification techniques are illustrated and compared in figure 3.12.
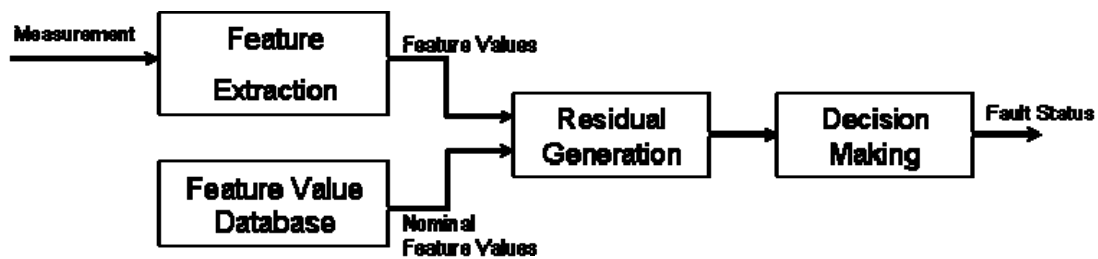
a) Signal-based FDI scheme.
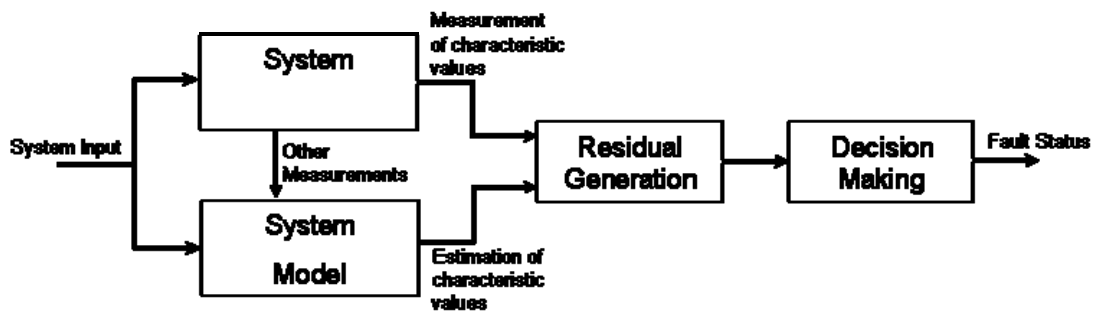
b) Model-based FDI scheme.

Figure 3.12: signal-based and model-based fault detection and identification (FDI) schemes.

Model-based approaches utilize the models of the system or process and the available measurements or internal values of the control algorithm to estimate some characteristic quantities of the system, e.g. system state, system outputs, parameters etc.

By comparing the estimated values to the measurements or predefined value range, residual can be generated and used to detect and identify faults. Typical model-based FDI approaches are observer-based approach, parity relation approach and parameter estimation approach [6]. The performance of model-based FDI approaches depends strongly on the quality of the model involved.

The signal-based FDI does not use models. The system behavior is expressed by the signal characteristics. Signal features that contain the information of fault status are first extracted from the measured signals by some signal processing techniques. Residuals are generated by comparing the feature values to their nominal values. Typical symptoms are the magnitudes of the time functions of the measured signals, their mean values, limit values, statistical moments, frequency spectrum, correlation coefficients, covariance etc [10]. The signal-based FDI approaches are in general more robust than the model-based FDI since they don't depend on any model and are hence immune to model error. But on the other hand, because signal-based FDI depends only on the directly measured signals, system states and immeasurable characteristic parameters are unknown.

To evaluate the performance of an FDI process, several performance indices have been defined [4], such as correct fault detection, false alarm rate, missed fault detection, incorrect fault detection and detection delay.

The reconfiguration mechanisms can be classified as online controller selection and online controller redesign/calculation [4], as shown in figure 3.10. In the first class of methods, different controllers associated with the predefined fault scenarios are designed a priori. And according to the decision made by the FDI algorithm, the proper controller is chosen online. Online controller selection is sometimes also known as projection-based methods. In the second class of methods, controllers are synthesized online after the occurrence of faults.

The online controller selection methods are highly dependent on prompt and correct operation of the FDI algorithm. Any false, missed, or error in fault detection may lead to degraded performance or even the loss of stability of a closed-loop system. In [11], attempt had been made to deal with the robustness problem of FDI and to design stability guaranteed active fault tolerant control. Some examples for online controller redesign are the pseudo-inverse method, Eigen-Structure assignment based algorithm, model-following approach and feedback linearization for non-linear systems [4].

3.2.3 The Proposed Fault Tolerant Control Scheme

The purpose of the fault tolerant control is to detect the fault of the AMR angle sensor and try to avoid brake actuator shut down. Since the rotor angle information is crucial for the position control, not shutting down the brake actuator implies that the position control will rely on the estimated rotor angle if AMR angle sensor is faulty. Actuator shut down can not be avoided if rotor angle estimation also fails. For this fault tolerance problem, it is not necessary to reconfigure the position controller. It is actually a problem to estimate the rotor angle online and to make decision if the angle measurement or the angle estimate should be fed to the position controller or neither of them (actuator shut down). The proposed scheme of the fault tolerant position control of the SM-PMSM is shown in figure 3.13. It is assumed that the status of the current sensors is known.

The decision making module determines which rotor angle (measured/estimated) should be used by the position controller or the actuator should be shut down. The decision is based on the fault status of current sensors and the fault status of the AMR sensor delivered by the fault detection module. To avoid stability problem caused by frequent switching between the two rotor angle information sources, the decision making module does not allow frequent switching. Once the position controller starts using the estimated rotor angle, switching back to the measured angle will only take place if the conditions for using measured angle have been fulfilled for long enough time. And restarting the brake actuator from the shut down state is beyond the consideration of this study, since this would involve analysis on the details of too many functions in the EMB system.

The fault detection module applies both model-based and signal-based fault detection and delivers the fault status of the AMR sensor. This module will be explained in chapter 4 in detail.

The angle estimation module estimates the rotor angle with the motor voltage and current. The estimation is only reliable if the current sensors are fault-free. The angle estimation is initialized during the pre-life check of the system and runs in parallel to the angle measurement in the whole actuator operation. Chapter 5 provides the detail of the rotor angle estimation method.
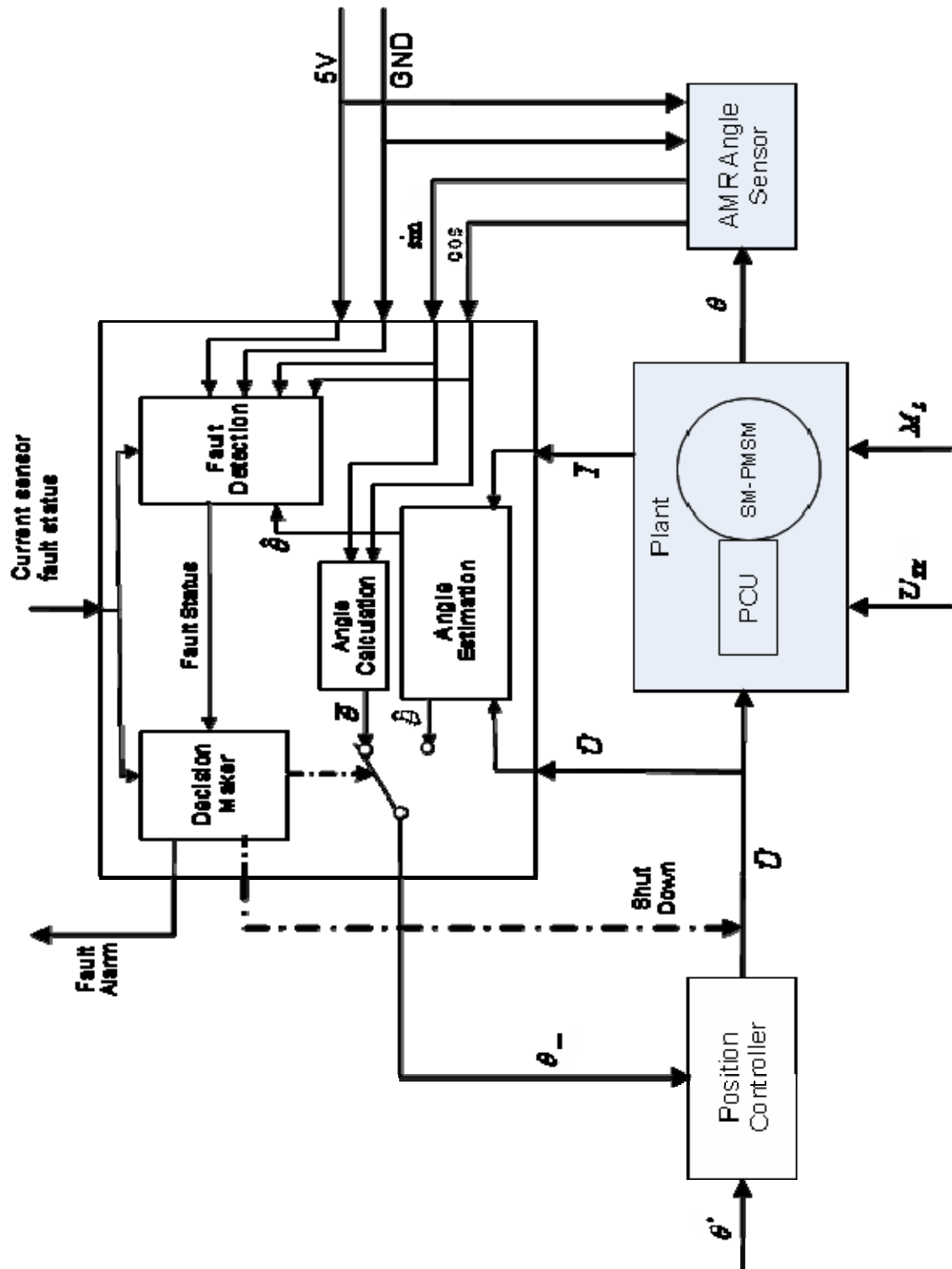
Figure 3.13: the proposed fault tolerant position control scheme against AMR angle sensor fault.

In figure 3.13, θ^* is the position set value, which is determined by the outer brake moment control loop. $\bar{U}$ is the set value of control voltage vector in the stator-fixed coordinate system. PCU is the power control unit. It contains the bridge circuit to

generate the terminal voltage and the sensors that measure the phase current and the DC-link voltage. $\bar{I}$ is the measured phase current vector in the stator-fixed coordinate system. $\bar{\theta}$ is the measured rotor angle. $\hat{\theta}$ is the estimated rotor angle. And $\theta_{\_}$ is the rotor angle that is fed to the position controller. $\overline{U}_{ZK}$ is the DC-link voltage. M_L is the loading moment. Except for the position controller, which works at a sampling rate of 400 Hz (T=2.5 ms); all the other software modules have a sampling rate of 10 kHz (T=100 µs).

Chapter 4

The Fault Detection and Decision Making

This chapter focuses on the design of the fault detection and the decision making of the fault tolerant position control of the SM-PMSM. Section 4.1 introduces important concepts and definitions of fault. Section 4.2 discusses about the fault behavior of AMR angle sensors. Section 4.3 explains the design of the fault detection module and discusses about the possibility of fault identification and compensation. The decision maker module is explained in section 4.4.

4.1 Concepts, Definitions and Classification of Faults

In general, a fault is something that changes the behavior of a technical system such that the system does no longer satisfy its purpose [17]. Faults can be an internal event, e.g. production related flaw, a broken signal connection, faulty signal amplification, component aging etc. It may also be a change in the environment in which the technical system works and exchanges information, energy and material, i.e. an incorrect power supply, unusual temperature change. It can also be the human who causes malfunction of the technical system by improper operation. In any case, fault is the primary cause of changes in the system structure or parameters that eventually leads to a degraded system performance or the loss of system function. Therefore in [17] a *fault* in a dynamical system is defined as:

A deviation of the system structure or the system parameters from the nominal situation.

Faults can be classified according to three main viewpoints which are their *nature,* their *origin* and their *persistence* [18].

The nature of faults can be accidental or intentional. Accidental faults are created fortuitously and intentional faults are created deliberately, presumably or malevolently [18].

The origin of faults can be further classified from three viewpoints: the *phenomenological causes,* the *system boundary* and the *phase of creation.* By considering the phenomenological causes, faults can be classified as physical faults and human-made faults [18]. Physical faults are caused by adverse physical phenomena. And human-made faults result from human imperfection. According to system boundary, one can distinguish internal faults and external faults. Internal faults could be a flaw in the microstructure of a chip, a short-circuited capacitor etc. External faults could be a wrong operation temperature range, electro-magnetic perturbation or incorrect supply voltage. With respect to the phase of creation, faults can also be classified as design faults and operational faults. Design faults are results of imperfections arising either during the development of the system or subsequent modifications or during the establishment of the procedures for operating or maintenance [18]. Operational faults occur during the system's exploitation.

Distinction can also be made with respect to the persistence of the faults. This leads to the classification of permanent faults and temporary faults. Permanent faults are the faults that are not related to pointwise conditions of the system, either internal or external [18]. That is, once occurred, such fault will persist until reparation. Temporary faults are faults that are present for a limited amount of time. When temporary faults are originated from physical external environment then they are called transient faults [18]. Temporary internal faults are often termed intermittent faults [18].

The classification of faults in [18] is shown in figure 4.1. It should be noted that the classifications according to the different viewpoints are not mutually exclusive. For example, a physical fault can be permanent fault, transient fault or intermittent fault; a design fault is a permanent fault. A summary is also provided in [18] on the possible combinations of the fault classes. This is shown in figure 4.2. The crosses in the table mark the possible combinations.
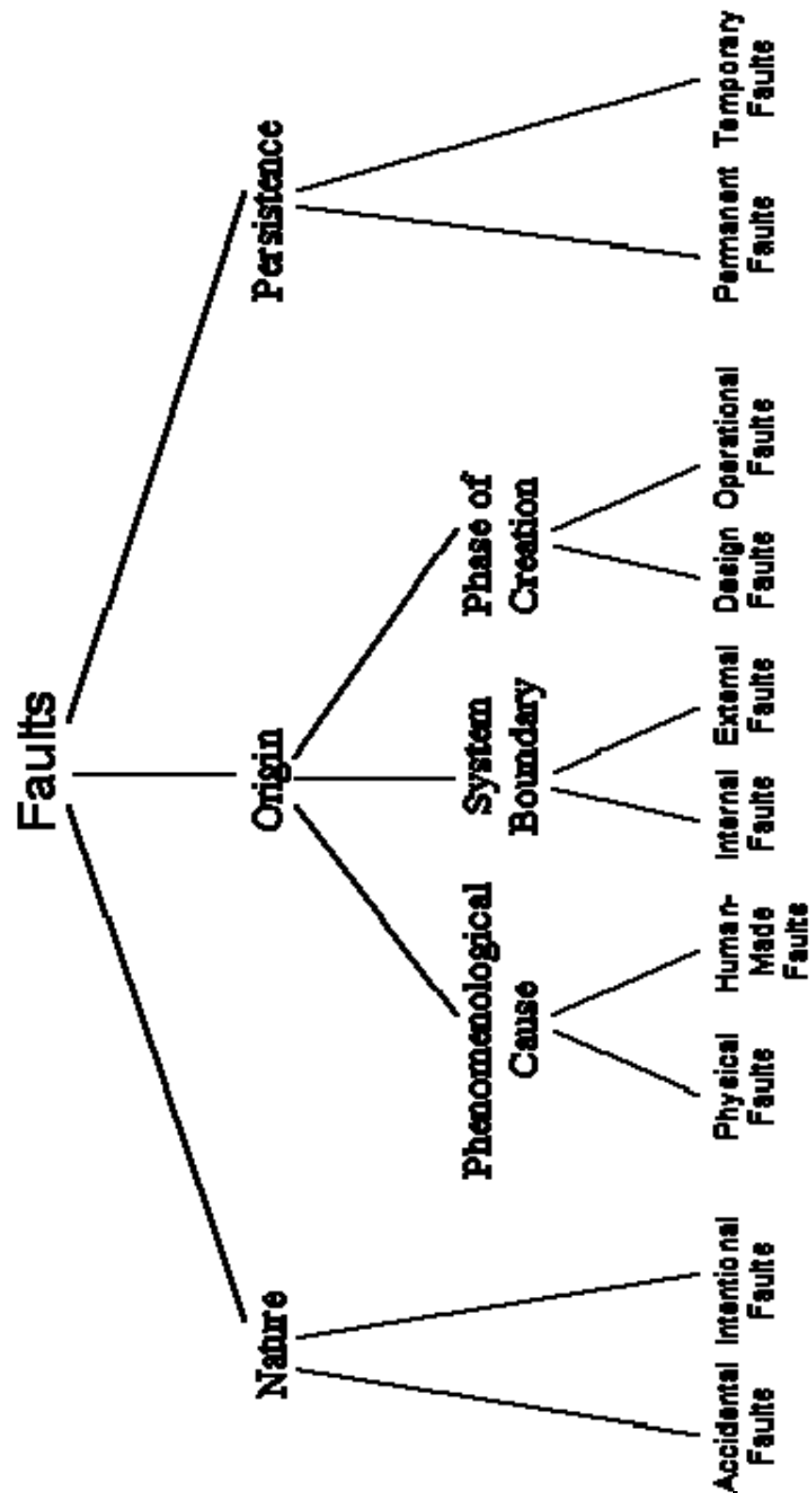
Figure 4.1: fault classifications according to various viewpoints in [18].

Nature — Accidental Faults	Nature — Intentional Faults	Phenomenological cause — Physical Faults	Phenomenological cause — Human-made Faults	Origin / System boundaries — Internal Faults	Origin / System boundaries — External Faults	Origin / Phase of creation — Design Faults	Origin / Phase of creation — Operational Faults	Persistence — Permanent Faults	Persistence — Temporary Faults	Usual Labeling
X	·	X	·	X	·	·	X	X	·	Physical faults
X	·	X	·	·	X	·	X	X	·	Physical faults
X	·	X	·	·	X	·	X	·	X	Transient faults
X	·	X	·	X	·	·	X	·	X	Intermittent faults
X	·	·	X	X	·	X	·	·	X	Design faults
X	·	·	X	X	·	X	·	X	·	Design faults
X	·	·	X	·	X	·	X	·	X	Interaction faults
·	X	·	X	X	·	X	·	X	·	Malicious logic
·	X	·	X	X	·	X	·	·	X	Malicious logic
·	X	·	X	·	X	·	X	X	·	Intrusions
·	X	·	X	·	X	·	X	·	X	Intrusions

Figure 4.2: summary on the possible combinations of fault classes [18].

4.2 The Fault Behavior of the AMR Angle Sensor

The premise of a successful design of fault detection is a clear definition of the relevant fault behavior. To define the relevant fault possibilities systematically, the system boundary and the possible interactions through the system boundary should be clarified. The relevant faults can then be gathered by methods like FMEA.

In the current design of the brake system, the physical rotor angle is detected by the AMR sensor, amplified by a signal conditioning circuitry (figure 3.9) and transferred to the signal processing unit as analog signals through shielded cable connection. The analog signals are then converted by analog-digital converter (ADC) and written to the register which the signal processing unit periodically reads for the calculation of the control algorithm. The boundary of the AMR sensor in this study is defined as the components from the conversion of the physical rotor angle into analog signals to the transferring of the analog signals for the signal processing. These components include:

- the permanent magnet mounted at the end of the rotor shaft;
- the AMR sensor chip, which contains the bridge circuits made of the magneto-resistive material and the signal conditioning circuitry;
- the shielded cable connection,

External influences through this boundary are:

- Operation temperature;
- External magnetic field;
- Electro-magnetic environment.

It is assumed that the mounting of the system is correct, only physical faults will occur. Design faults in the system including the programming faults (program bugs) are also excluded. The fault effects of each component are analyzed in the following subsections separately as was done in the FMEA. The signals from the AMR sensor that are available for the fault detection algorithm are:

- The supply voltage to the sensor;
- The sine output of the sensor chip;
- The cosine output of the sensor chip.

4.2.1 Faults Caused by the Permanent Magnet

There are three types of faults that may cause non-adequate magnetic field arrangement [19]. They are:

- Insufficient magnet field strength;
- Inhomogeneous magnet field;
- Influence of external magnetic fields influencing the primary field used for measurement.

The influence of external magnetic field depends on the actual operation environment and therefore its influence on the angle measurement error can not be described generally. The only possibility to get rid of external fields or to limit its impact is to use proper magnetic shielding.

There are two possible causes for an inhomogeneous magnet field: either the sensor is not properly aligned to the magnet or the magnet itself has inhomogeneous field due to scattered production quality. The sensor to magnet position must be ensured by proper mechanical construction of the sensor housing, which aligns the sensor to the magnet with acceptable tolerance and prevents incorrect mounting. The scattered quality of the magnet is more likely to cause inhomogeneous magnet field. But again, the inhomogeneity of the magnet field due to quality scatter is not possible to be described in general.

A complete magnetic saturation of the AMR sensor is not possible since it requires an infinitively strong magnet field. In the practice, the permanent magnet used for AMR angle measurement must provide field strength larger than a certain threshold so that the error due to incomplete magnetic saturation is reduced to a tolerable level. The choice of the magnet is always a compromise between the rest error and the magnet cost. Insufficient magnet field can be caused by aging, operation under high temperature or scattered quality in the magnet production. According to the technical documents available, insufficient magnetic field strength can introduce two fault effects, one is the form error of the sine and cosine output signals (higher order harmonics) and the other is hysteresis of the sensor response. For a better understanding of the fault effect of insufficient magnet strength, experiments have been done on the test bench on our specific AMR sensor. To weaken the magnet field, the sensor is shifted away from the magnet in the axial direction. A mechanical device on the test bench (figure 4.3 a) shifts the sensor to different distance to the magnet surface. The magnetic field strength at different distance is measured with a Gauss-meter before

the experiment so that we know the effective field strength on the sensor (figure 4.3 b) at different distance. Note that only the maximal field intensity in the radial direction at the specific distance was measured. The flux density (B) was measured instead of the field intensity (H). And the field intensity was calculated with the magnetic permeability of air after the measurement. The distance can be read directly from the micrometer. After measuring the field intensity, the AMR sensor is shifted with the same mechanical device to different positions; and measurements of the sine and cosine outputs of the sensor were done at different rotor speeds.

At zero distance, the magnet field is 90 kA/m (the recommended field intensity in the technical document is 100 kA/m). The sensor is shifted away from the magnet at equal increment of distance; and finally to a position where the magnet field is only 2 kA/m.

In the experiment, it has been observed that the fault effect of insufficient magnet strength is independent from the rotor speed. The dominant fault effect of insufficient magnet field strength is the amplitude reduction of the sinus- and cosine-output signals, which dropped from 1.75 V to 0.53 V (figure 4.4).
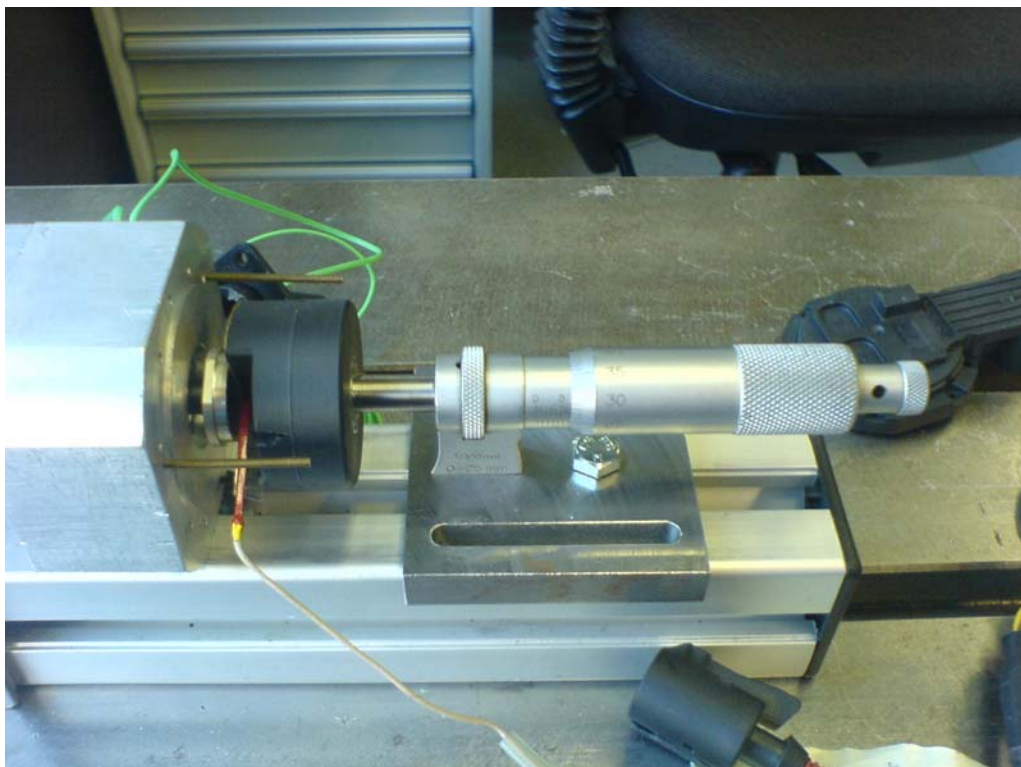
a) The mechanical device (micrometer) used to shift the sensor.
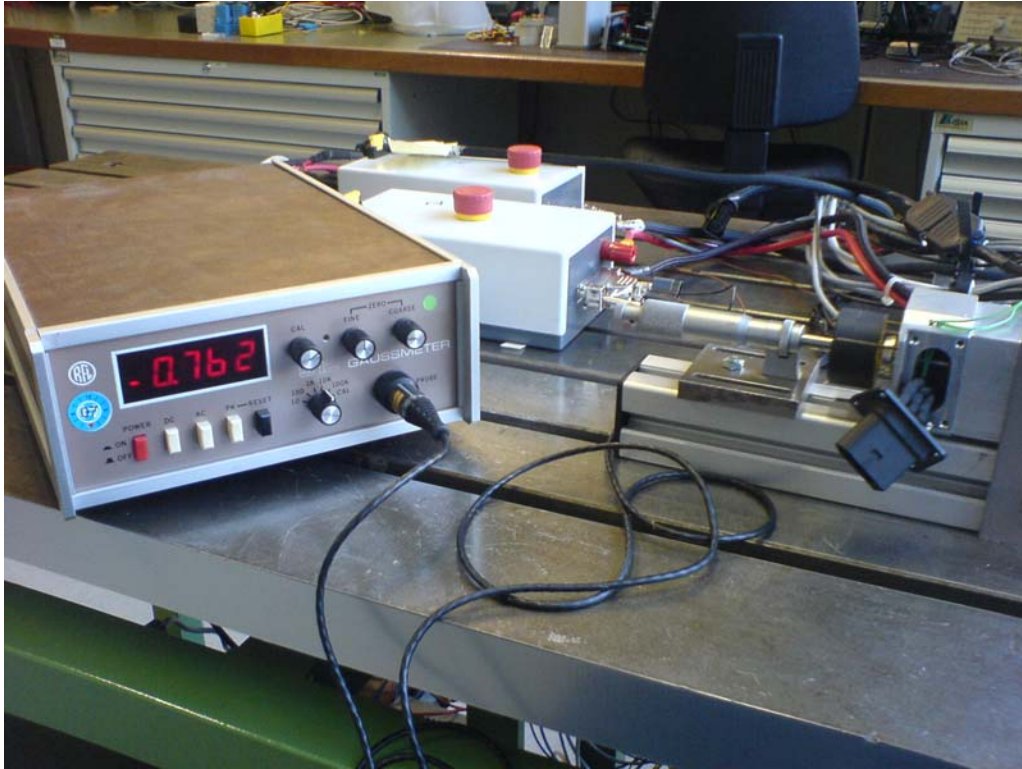
b) Magnet field measurement with a Gauss Meter.

Figure 4.3: the experiment setup for measuring the fault effect of insufficient magnetic field strength of AMR angle sensor.
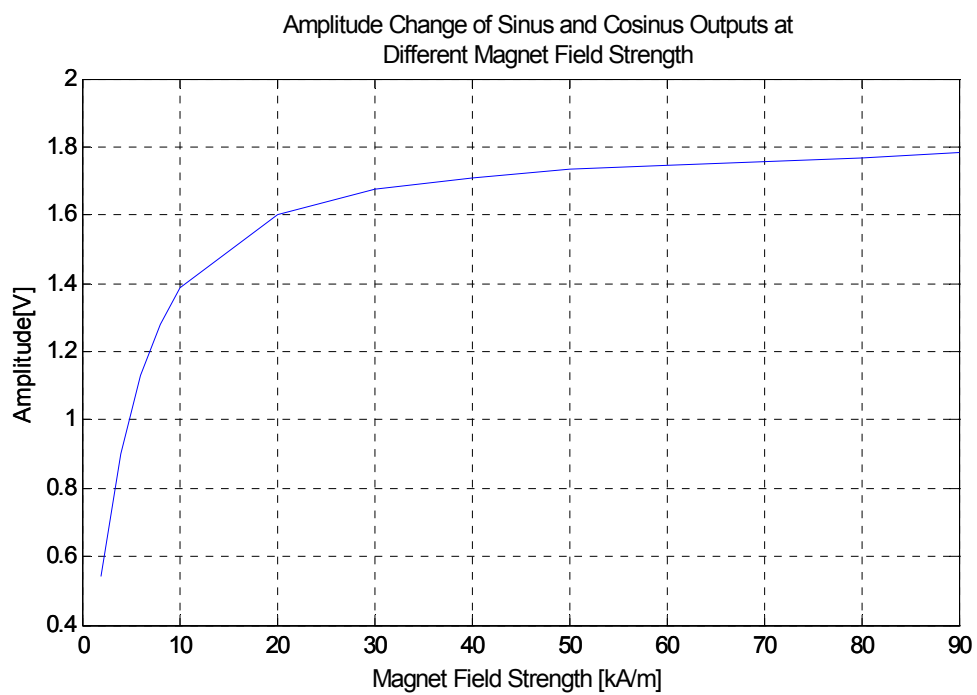
Figure 4.4: the relation between the magnet field intensity and the amplitude of sine and cosine signals.

In comparison to the amplitude reduction, the higher order harmonics and hysteresis are not significant. At magnet field strength higher than 20 [kA/m], the amplitude of the higher order harmonics is less than 5% of the useful sine signal (figure 4.5); the hysteresis is too weak to be observed. These errors are ignorable for the angle measurement with equation 3.19.
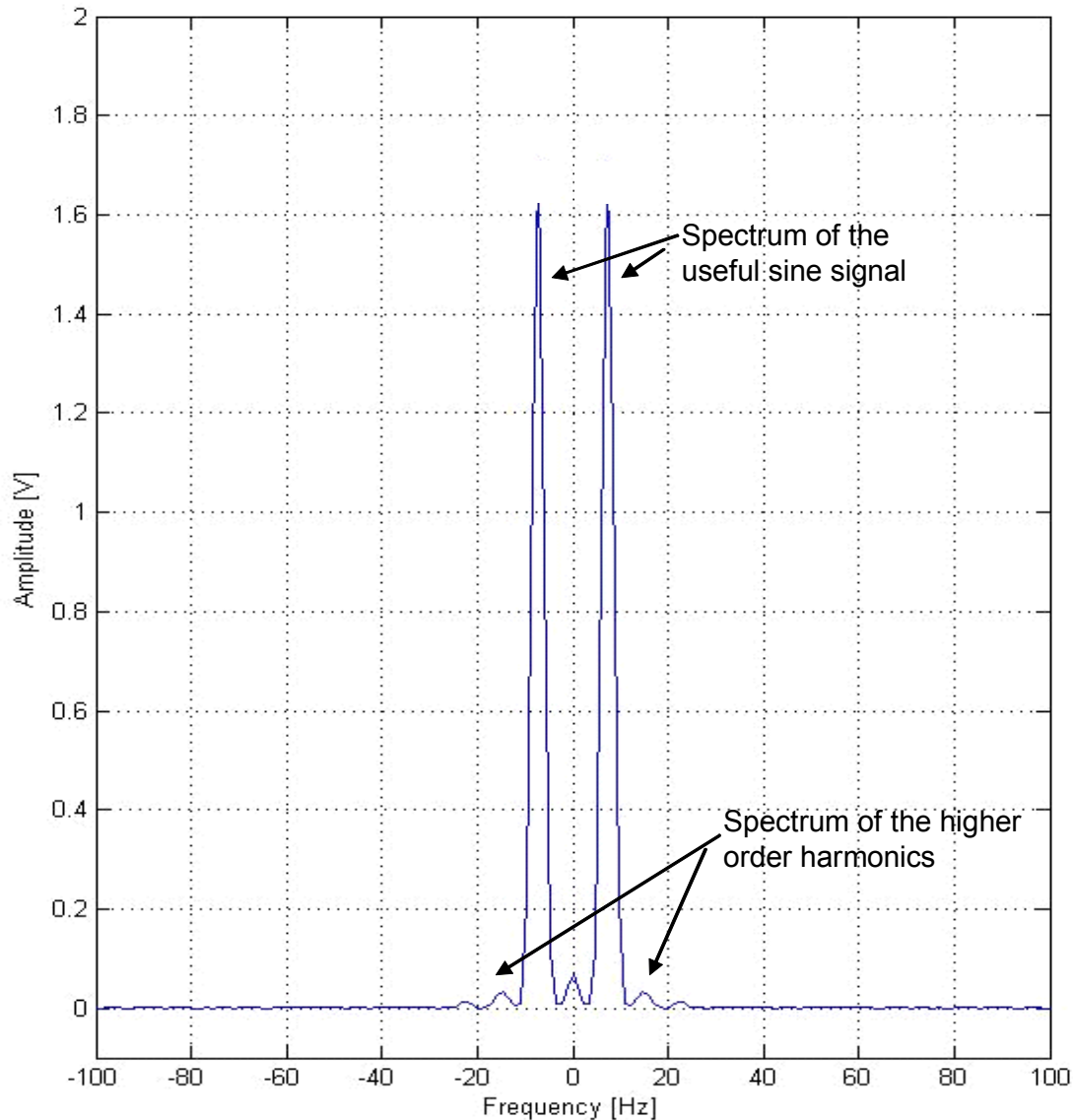
Figure 4.5: amplitude spectrum of the sine output of the AMR sensor after the offset is compensated. The magnet field strength is 20 kA/m and the motor is rotating at 8π rad/s. It can be seen that the amplitude of the higher order harmonics is very weak. The zero-frequency component is caused by non-ideal compensation of the offset.

4.2.2 Faults in the AMR Sensor Chip and Cable Connection

The AMR sensor chip consists of two parts: the bridge circuits made of the magnetic resistive material; and the signal conditioning circuitry (figure 3.9). The outputs of the chip are:

- $A_s \sin 2\alpha + U_b / 2$;
- $A_c \cos 2\alpha + U_b / 2$;

Besides incorrect supply voltage, any micro flaw in the chip, aging, operation under wrong temperature or external electro-magnetic disturbance can all result in the deviation of the sensor behavior from its nominal behavior, e.g. changed signal amplitude, offset or waveform. The supply voltage can be directly monitored while the other fault causes and effects are unknown. Therefore, except for the supply voltage, the other faults of the AMR sensor chip can only be monitored by checking if the sensor shows its nominal behavior, i.e. the measured angle is plausible compared to the estimated angle and signal features like amplitude, offset and waveform are proper.

Faults in the cable connection can be caused by loose contact of the connecter or damaged cables. This could result in constant signal or intermittent signal loss. The damage of the cable shielding exposes the cable to external electro-magnetic disturbance. The effect depends on the electro-magnetic environment of the operation and can not be described in general.

4.2.3 Summary on the Relevant Faults

In this section, the faults relevant for the design of fault detection are introduced. Basically, the relevant faults are caused by malfunctions in three different components: the permanent magnet; the sensor chip; and the cable connection. The possible faults and their effects are summarized in figure 4.6.

It had been observed through test bench measurement that the higher-order harmonics and the hysteresis caused by insufficient magnet field strength are ignorable compared to the effect of amplitude reduction in the sine and cosine output signals. Typical fault effects of the AMR sensor are incorrect amplitude, incorrect offset or constant sine and/or cosine signal. Other fault effects can not be described in general be-

cause they either depend on unknown external influence or have too many possibilities like in the case of the sensor chip malfunction.

Components	Fault Mode	Fault Effect

AMR Sensor

Permanent Magnet
- Insufficient Magnet Field Strength
  - Amplitude reduction of both Sin and Cos outputs
  - Form error of both Sin and Cos outputs (higher-order harmonics)
  - Hysteresis of Sin and Cos outpus
- Inhomogeneous Magnet Field
- External Magnet Field Disturbance
  - Faulty Sin and Cos outputs. Fault effect can not be described in general

Sensor Chip
- The Bridge Circuit Defect
- The Amplification Circuit Defect
  - Incorrect amplitude of Sin and/or Cos outputs
- The Offset Circuit Defect
  - Incorrect offset of Sin and/or Cos outputs
- The Supply Voltage Fault
  - Faulty Sin and Cos outputs. Fault effect can not be described in general

Cable Connection
- Cable Broken
  - Sin and/or Cos signal(s) remain constant
  - Supply Voltage loss for AMR sensor. Both Sin and Cos signals remain constant
- Loose Contact
  - Intermittent fault in Sin and/or Cos signals. Fault effect can not be described in general.
- Electro-Magnetic Disturbance
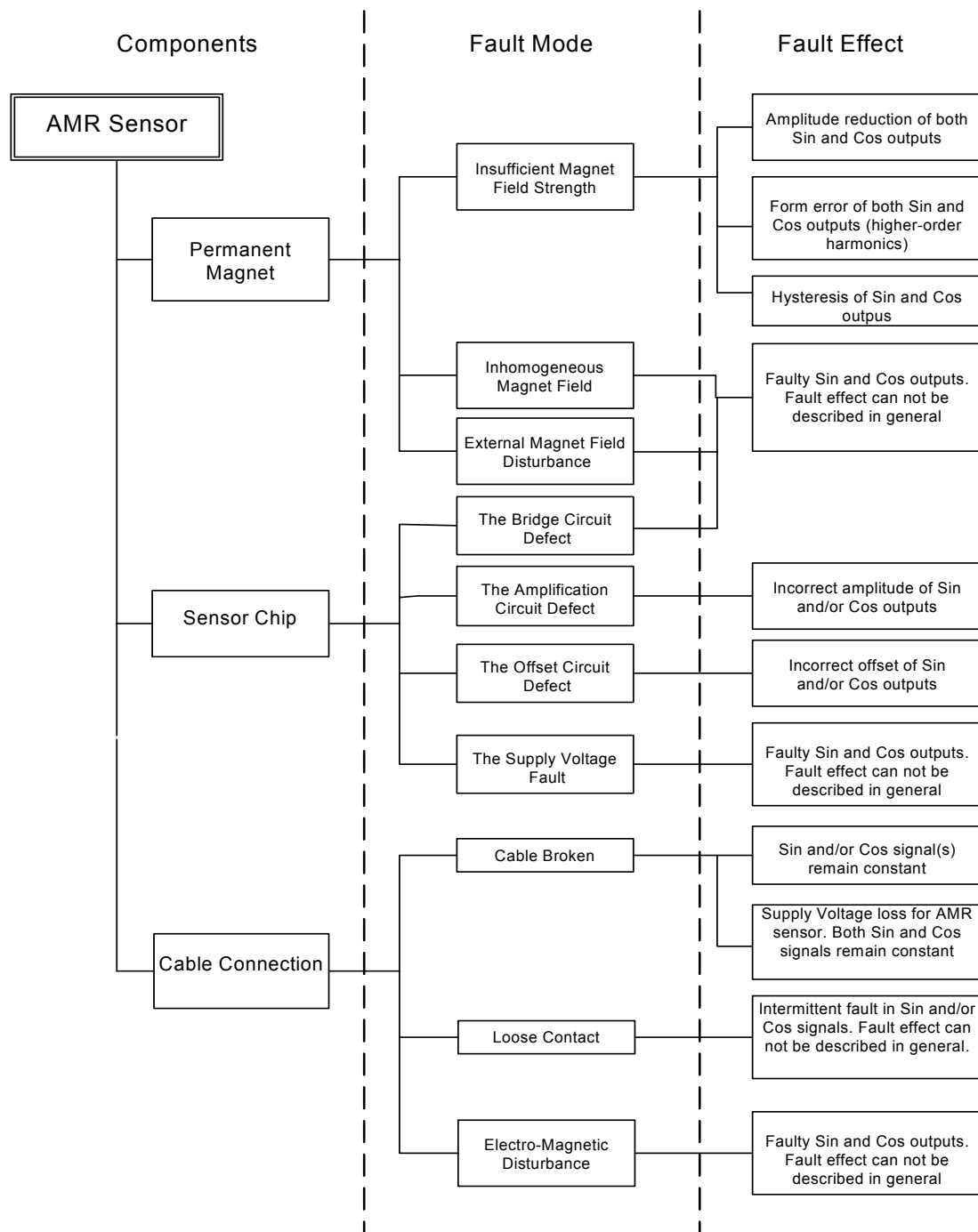 - Faulty Sin and Cos outputs. Fault effect can not be described in general

Figure 4.6: the relevant faults and their effects.

4.3 The Fault Detection Module

4.3.1 Fault Detection

This section focuses on the design of the fault detection module (figure 3.13). Ideally, the fault detection module should change the output fault status immediately if any relevant fault occurs. The fault detection can be either signal-based or model-based. However, the effects of many faults summarized in figure 4.6 depend on the actual operation environment and can not be described in general. This makes it impossible to define a feature set for the signal-based fault detection with which it can determine if the sensor is in *fault-free* state, because any feature except for the real rotor angle value could be violated by unknown fault behavior. Therefore, model-based fault detection must also be applied to check the plausibility of the measured angle. The model-based fault detection compares measured angle and the angle estimate. Since the correctness of the angle estimate relies on the intact operation of the current sensors, the fault status of the current sensors is also considered. If the current sensors are faulty, the result of the plausibility check will be discarded.
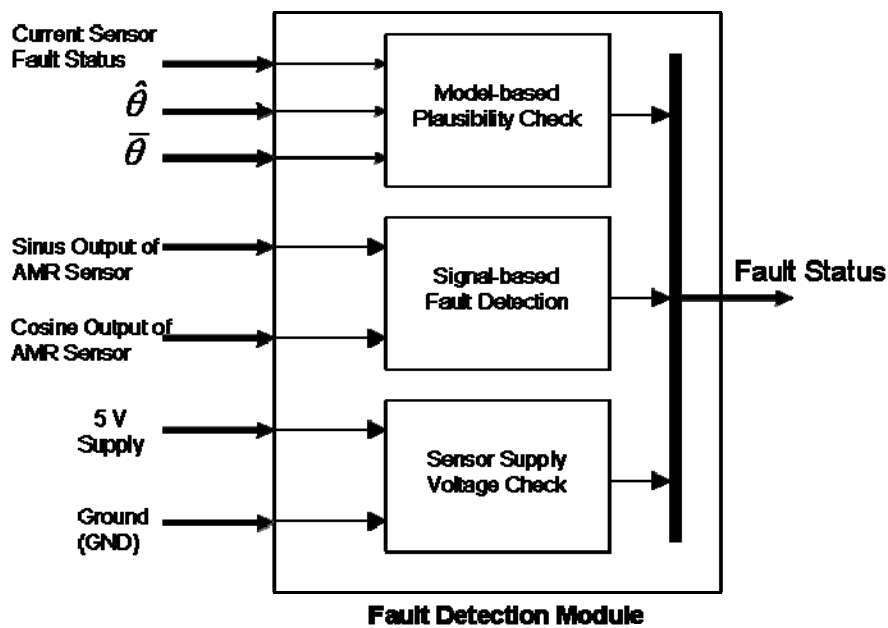

Figure 4.7: the structure of the fault detection module.

The dependency on the current sensor fault status also makes it necessary to have signal-based fault detection in parallel so that fault detection is still possible for some of the fault categories if the plausibility check is not reliable. The supply voltage for the sensor is monitored separately. The structure of the fault detection module is

shown in figure 4.7. The output fault status is a 3-dimensional vector comprised by the results from each of the three blocks.

The choice of signal feature is essential for the design of signal-based fault detection. For the sine and cosine outputs of the AMR sensor, the typical signal feature is the circular locus; if they are plotted in an orthogonal x-y coordinate by defining:

$$x = A_c \cdot \cos 2\alpha + O_c$$
$$y = A_s \cdot \sin 2\alpha + O_s$$

<div align="right">(4.1)</div>

Where x is the output of the sine channel and y is the output of the cosine channel. The offset of sine channel is denoted as O_s and the offset of cosine channel as O_c, the locus of the sensor outputs fulfils the equation 4.2

$$\frac{(x - O_c)^2}{A_c^{\,2}} + \frac{(y - O_s)^2}{A_s^{\,2}} = 1$$

<div align="right">(4.2)</div>

In fault-free operation, the signal amplitude A_c and A_s are equal and non-zero. The equation 4.2 represents a circle with a radius $r_0 = A_c = A_s$ and the centre (O_c, O_s). The circular locus is plotted in figured 4.8. This circle is taken as the standard circle. The signal-based fault detection checks if the measurement points are lying on this standard circle. Checking the distance r between the measured point and the centre of the standard circle (O_c, O_s) has become a standard method for the fault detection of AMR angle sensor. The distance r is compared to the radius r_0 of the standard circle. The difference between r and r_0 is shown in figure 4.8 as $e = r - r_0$. And it is taken as the residual. A positive and a negative threshold have been defined to determine if the residual e exceeds the allowed range[3]. Any faults that could make the measurement point (x, y) leave the circular locus can be detected with this simple method, e.g. amplitude fault, offset fault.

Another simple method to check the plausibility of AMR sensor outputs is to calculate the angle from only the sinus or the cosine output of the sensor and check if they are consistent. The standard offset and amplitude are assumed during the angle calculation. But since the radius check, the model-based plausibility check and the supply voltage check together cover all the fault possibilities. This method is not necessary.
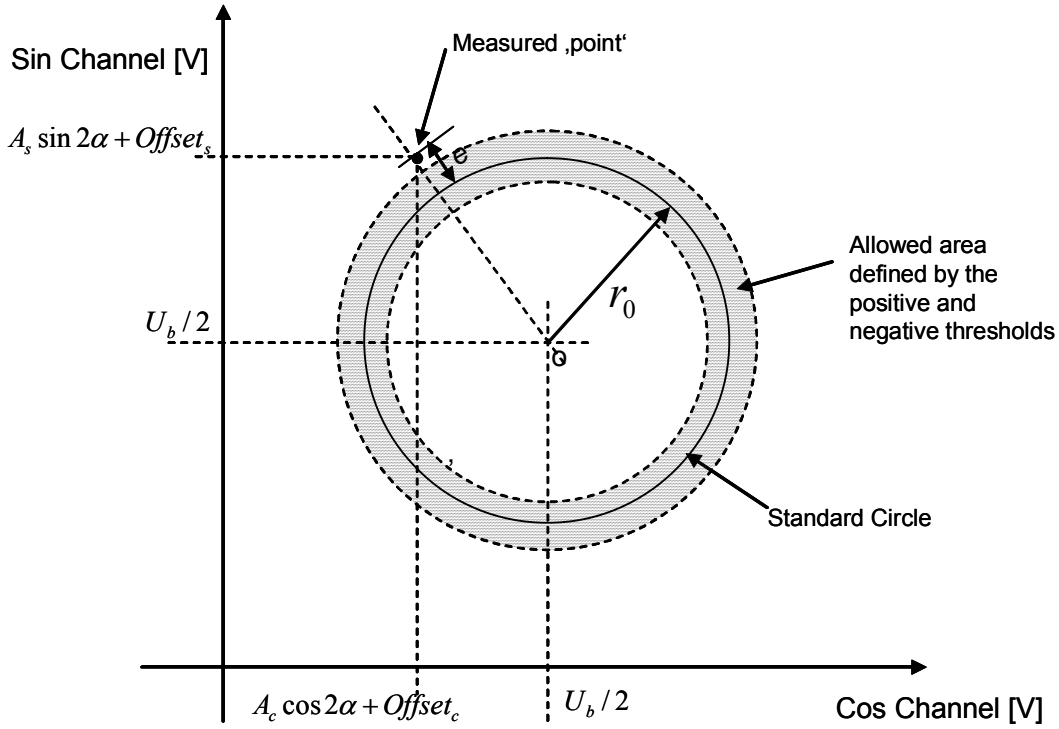
Figure 4.8: the signal-based fault detection of AMR angle sensor with radius monitoring.

4.3.2 Fault Identification and Compensation

According to the fault possibilities summarized in figure 4.6; if the measurement points can be fitted to an ellipse described by equation 4.2 but with a new set of parameters A_s, A_c, O_s and O_c, it is reasonable to assume that only amplitude and/or offset fault occur. In this case, the new parameters can theoretically be used to compensate the amplitude fault and/offset fault. This possibility had also been investigated in this study. The least-square method (LS), recursive least-square method (RLS) and the recursive least-square method with forgetting factor had been considered. However, none of these methods provides satisfying solution for the problem. The reason will be explained later in this subsection. Since the online compensation of amplitude fault and offset fault is only a 'nice-to-have' function; the investigation on this possibility is not further pursued. The fault compensation is hence not included in the proposed fault tolerant position control of the SM-PMSM. The investigated methods are still presented here.

---

[3] These threshold values are provided by the series product developer who is responsible for the fault monitoring function of this type of sensor.

The curve fitting basically looks for the optimal set of the parameters A_s, A_c, O_s and O_c so that the elliptical curve described by equation 4.2 is best-fitted to the given set of successive measurement points. The residual of the fitting can be used to judge if the fitting is precise.

Least Square Method (LS)

The Least-Square Method is a common mathematical procedure for such curve fitting problem, which searches for the parameters by minimizing the square sum of error (residual). The square sum of error is used instead of the sum of the absolute values so that the residual function is differentiable. To apply the least-square method, the equation 4.2 is reform as:

$$y^2 = -\frac{A_s^2}{A_c^2}x^2 + 2O_c\frac{A_s^2}{A_c^2}x + 2O_s y - O_c^2\frac{A_s^2}{A_c^2} - O_s^2 + A_s^2$$

$$A_c^2 \neq 0$$

(4.3)

To simplify the equation 4.3 the following new parameters are defined. The amplitude and offset parameters A_s, A_c, O_s and O_c will be solved from these new parameters later.

$$a_1 = -\frac{A_s^2}{A_c^2};$$

$$a_2 = 2O_c\frac{A_s^2}{A_c^2};$$

$$a_3 = 2O_s;$$

$$a_4 = -O_c^2\frac{A_s^2}{A_c^2} - O_s^2 + A_s^2$$

(4.4)

Equation 4.3 is now:

$$y^2 = a_1 x^2 + a_2 x + a_3 y + a_4$$

(4.5)

Suppose the n newest measurement points are taken for the estimation, and denote the equation error of each measurement point as ε_i ($i = 1 \ldots n$); the following equation system can be established:

$$\underbrace{\begin{pmatrix} y_1^2 \\ \vdots \\ y_n^2 \end{pmatrix}}_{Y} = \underbrace{\begin{pmatrix} x_1^2 & x_1 & y_1 & 1 \\ & & \vdots & \\ x_n^2 & x_n & y_n & 1 \end{pmatrix}}_{X} \cdot \underbrace{\begin{pmatrix} a_1 \\ a_2 \\ a_3 \\ a_4 \end{pmatrix}}_{\gamma} + \underbrace{\begin{pmatrix} \varepsilon_1 \\ \vdots \\ \varepsilon_n \end{pmatrix}}_{\varepsilon} \qquad (4.6)$$

And according to the least square method, the optimal parameter vector is:

$$\gamma = (X^T X)^{-1} X^T Y \qquad (4.7)$$

Knowing that $A_s, A_c, O_s, O_c > 0$, the new amplitudes and offsets can be solved with equation 4.4. But if the matrix $X^T \cdot X$ in equation 4.7 is ill-conditioned, the parameter estimation will fail. A situation that leads to such ill-conditioned matrix is that the successive points are very close to one another. This is the case if the rotor rotates at low speed or stands still. Continuous parameter estimation is only possible if the rotor is always rotating and rotates fast enough. Therefore the fault compensation with least square method does not have practical meaning for the fault tolerant position control of the SM-PMSM in the brake actuator. Because most of the time the SM-PMSM stands still.

Recursive Least Square Method (RLS)

The recursive least-square (RLS) method basically delivers the same parameter estimate as the LS in matrix form except that all the measurement points since the start of the estimation are considered instead of only a limited number of the newest measurement points (window of observation of LS). The RLS avoids the high online computation effort caused by the inversion and multiplication of the $n \times 4$ matrix X in the LS method. The disadvantage of RLS is that the residual of every measurement point since the measurement start is equally weighted. If there is a change in the parameter vector γ, it takes theoretically infinitively long time for the estimated parameter γ_n to converge to the new values, because the 'old measurements' are never 'forgotten'. This disadvantage makes the normal RLS not practical for online variable-parameter estimation.

Recursive Least Square Method with Forgetting Factor

An approach to accelerate the convergence speed of RLS is the modification of RLS with *forgetting factor* (FRLS). The FRLS minimizes a weighted residual:

$$J_n = \sum_{k=1}^{n} \lambda^{n-k} \cdot \varepsilon^2(k) \tag{4.8}$$

where $0<\lambda<1$ is the forgetting factor. With the new definition of residual in equation 4.8, the newer the measurement is, the stronger its corresponding square error $\varepsilon^2(k)$ will be weighted. This makes the estimation response faster to the recent parameter change. The choice of the forgetting factor λ is a compromise between fast convergence (small λ) and estimation stability (big λ). Although the explicit inversion of the correlation matrix in LS method is avoided by the FRLS; the ill-condition problem of the LS method is still unsolved. The FRLS also fails if the heavily weighted measurement points are too close to one another.

4.3.3 Summary on the Fault Detection Module

The fault detection module presented in section 4.3 consists of a model-based plausibility check, a signal-based fault detection block (radius check) and the monitoring of the supply voltage. Monitoring the radius is able to check the form of the locus of the measurement points. The amplitude and offset faults and any faults that change the form of measurement locus can be detected by this method. Constant output fault and other undefined fault behavior can be detected by the model-based plausibility check, which compares the estimated angle and the measured angle. Hence all the possible faults in figure 4.6 are covered by the proposed fault detection. The fault status from each fault detection block is low-pass filtered to avoid pulse-like status change. It should be noted that the fault detection module is working at a much higher sampling frequency (10 kHz) than the position controller (400 Hz). Therefore, the delay of the fault status caused by the low-pass filter will be 'invisible' for the position controller if the time constants of the filters are chosen small enough.

4.4 The Decision Making Module

The decision making module is a logic unit that determines the state of the brake actuator control loop. It considers the following status:

a. Fault status from the model-based plausibility check;
b. Fault status from the signal-based fault detection;
c. Fault status from the supply voltage monitoring;
d. The status of current sensors.

Three states of brake actuator control are possible:

1. Position control with measured rotor angle;
2. Position control with estimated rotor angle,
3. Shut down actuator.

Since the fault statuses provided by the fault detection module have already been low-pass filtered, pulse-like status change is not possible. Once the condition for state 1 of the brake actuator control is not fulfilled, the decision maker will switch the control to state 2 or 3. The control will be switched back to state 1 from state 2 only if the condition for state 1 has been fulfilled for a defined time. How long this time should be remains a topic for further investigation. Frequent state switching due to intermittent fault is impossible under this rule. The brake actuator will be shut down if the angle estimation is not reliable, i.e. the current sensors are faulty. Re-starting the brake actuator from shut down state is not investigated, since this would involve too many detail functions of the EMB system.

The decision regulations are rather simple. The conditions for the choice of each control state are listed below. The letter representing each fault status itself means 'fault-free' in the logic expressions. And its negation means 'faulty'.

Actuator Control State	Verbally Formulated Conditions	Logic Expression
State 1: position control with measured rotor angle $\bar{\theta}$	If the current sensors are intact, then the result of model-based and signal-based fault detection as well as the supply voltage monitor must all be fault-free If the current sensors are faulty, then the result of signal-based fault detection and the supply voltage monitor must be fault-free	$(e \wedge a \wedge b \wedge c) \vee (\bar{e} \wedge b \wedge c)$

State 2: position control with measured rotor angle $\hat{\theta}$	The current sensors are intact. If the result of the model-based or the signal-based fault detection or the supply voltage monitor is *not* fault-free	$e \wedge \left(\bar{a} \vee \bar{b} \vee \bar{c} \right)$
State 3: shut down the brake actuator	If state 1 and state 2 can not be chosen	$\overline{\left((e \wedge a \wedge b \wedge c) \vee (\bar{e} \wedge b \wedge c) \right)}$ $\vee \left(e \wedge \left(\bar{a} \vee \bar{b} \vee \bar{c} \right) \right)$

Table 4.1: the regulations for the decision making

It is trivial that the conditions are collectively exhaustive. The condition for state 3 is exclusive to the conditions for state 1 and state 2. It is only necessary to proof that the conditions for state 1 and state 2 are mutually exclusive.

Proof:

$$\left((e \wedge a \wedge b \wedge c) \vee (\bar{e} \wedge b \wedge c) \right) \wedge \left(e \wedge \left(\bar{a} \vee \bar{b} \vee \bar{c} \right) \right)$$
$$= \left((e \wedge a \wedge b \wedge c) \vee (\bar{e} \wedge b \wedge c) \right) \wedge e \wedge \left(\bar{a} \vee \bar{b} \vee \bar{c} \right)$$
$$= (e \wedge a \wedge b \wedge c) \wedge \left(\bar{a} \vee \bar{b} \vee \bar{c} \right)$$
$$= e \wedge \left(\bar{a} \vee \bar{b} \vee \bar{c} \right) \wedge a \wedge b \wedge c$$
$$= e \wedge \overline{(a \wedge b \wedge c)} \wedge (a \wedge b \wedge c)$$
$$= 0$$

This means the conditions for state 1 and state 2 are mutually exclusive. Therefore the switch conditions defined in the table are mutually exclusive and collectively exhaustive.

Chapter 5

The Rotor Angle Estimation

Rotor angle estimation with motor voltage and current is necessary for the model-based plausibility check of the AMR sensor as well as the fault tolerant position control after the AMR sensor fails. The phase voltage signals are taken from the output of the controller after the voltage limiter. And the phase current signals are measured by three LEM converters on the PCU[4].

In this chapter, a number of angle estimation methods are introduced. Their application condition, advantages and disadvantages are analyzed. Section 5.1 makes a short overview on the existing methods. Section 5.2 focuses on the passive angle estimation. And section 5.3 explains the active rotor angle estimation. The angle estimation for the fault tolerant position control of the SM-PMSM is presented at the end in section 5.4.

5.1 An Overview of the Existing Rotor Angle Estimation Methods

The electrical commutation for the control of an SM-PMSM requires precise information on the rotor angle so that phase currents can be synchronized to the instantaneous position of the rotor. The cost of angle sensors and the difficulty to place them has encouraged researchers to avoid their use and to research on the sensorless control. The idea of position-sensorless operation of brushless machines was first elaborated by Frus and Kuo [24] using a technique known as 'waveform detection' for deducing rotor position in voltage-fed variable-reluctance stepping motors. Since then

---

[4] Power Control Unit (PCU) consists of the DC/AC converter (B6 bridge circuit), the three LEM converters for phase current measurements and some other monitoring functions.

many solutions have been published. By applying different kinds of machine models and physical effects, they all use phase current and voltage to derive the rotor angle. There are three known physical effects that are exploited for the rotor angle estimation:

- Flux linkage;
- Motional electromotive force (back-EMF);
- Inductance variations due to local saturation.

Methods applying the local saturation related inductance variation inject test current or voltage to stimulate the magnetic saturation and extract the rotor position dependent inductance anisotropy from the voltage or current response to the test signal. These methods are hence called active estimation methods. Depending on the form of the injection signal, such methods can be further classified as methods using periodic pulse sequence or methods using continuous carrier injection. Rotor angle estimation basing on flux linkage or back-EMF do not need to inject any test signal and are therefore called passive methods.

Although many solutions can be found in the literature for both passive and active methods, each group of estimation methods has its advantages and drawbacks. The flux linkage based estimation proposed by Hu and Wu [21] successfully constrains the locus of the flux linkage estimate on the origin-centered circle. However, it is shown in subsection 5.2.1 that if the rotor does not rotate across the neutral line (figure 5.7), the angle estimation error will accumulate until it reaches a constant. Despite this problem, the flux linkage based estimation remains the only stable passive estimation method for low and zero rotor speed due to its open-loop nature. To correct the angle estimation error of the flux linkage based method, the back-EMF based closed-loop angle estimation is also applied during high speed motor operation. However such methods are not applicable for very low (<100 rpm) and zero rotor speed due to the vanishing of the back-EMF. Active estimation methods provide the possibility to estimate the rotor angle at very low and zero speed, but they either introduce strong torque ripple or have poor robustness for angle estimation of SM-PMSM. The active angle estimation can also be disturbed by big motor moment.

5.2 Passive Rotor Angle Estimation Methods

The passive rotor angle estimation methods exploit either the physical effect of flux linkage or back-EMF. Methods utilizing the back-EMF base on the machine voltage equation 3.5. The extended Kalman filter (EKF) approaches are basically also back-EMF based methods. But they combine the voltage equation and the mechanical equation in one system model and do not explicitly estimate the back-EMF vector. Due to the vanishing of back-EMF, such estimation methods can not be applied to operation at very low rotor speed or standstill, though they can generate good result at high and medium rotor speed (>100 rpm). Flux linkage based estimation methods do not have a lower speed limit for their application. However, methods using open-loop integration suffer the well-known DC-drift problem. Hu and Wu [21] proposed a closed-loop integrator with internal amplitude limiter, which constrains the flux linkage estimate on the origin-centered locus.

This section makes an introduction on the two important categories of passive estimation methods: the flux-linkage based methods and the back-EMF based methods.

5.2.1 Flux-Linkage-Based Rotor Angle Estimation

5.2.1.1 The Open-loop Integration Method

The open-loop integration method can be described briefly as integrating the back-EMF in the space-fixed α-β coordinate. The definitions of the different coordinate systems are depicted in figure A.1 (appendix A). Due to the small value of the inductivity L in the electrical machine equations 3.5 in the α-β coordinate, the differential terms of the currents can be ignored. The flux linkage vector λ in α-β coordinate is then calculated by:

$$\lambda_\alpha = \Psi_{pm}\cos\theta_d = \int_0^t (U_\alpha - Ri_\alpha)d\tau + \lambda_{0,\alpha}$$

$$\lambda_\beta = \Psi_{pm}\sin\theta_d = \int_0^t (U_\beta - Ri_\beta)d\tau + \lambda_{0,\beta}$$

(5.1)

The rotor angle is obtained by:

$$\theta_d = \arctan \frac{\lambda_\beta}{\lambda_\alpha} \tag{5.2}$$

The disadvantage of this estimation approach is the open-loop integration. In the practice, the measurement offset of voltage and current can never be completely removed. This offset error is accumulated by the open-loop integrator. And the accumulated offset results in a time-proportional drift of the centre of the circular locus of the estimated flux vector (figure 5.1).
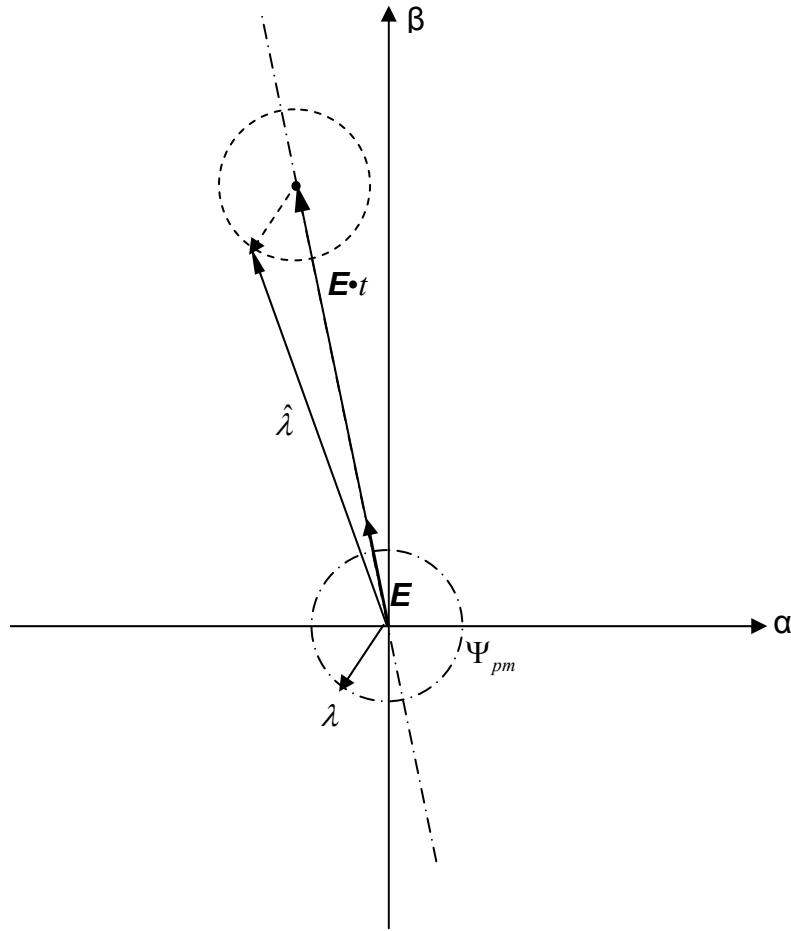
Figure 5.1: the drift of the circular locus of the estimated flux linkage due to the accumulation of measurement offset.

If the measurement offset of $\vec{U} - R \cdot \vec{I}$ is assumed to be a constant vector E as shown in figure 5.1; the origin-centered circular locus of the flux linkage estimate $\hat{\lambda}$ drifts away in the direction of the offset vector E. If t is big enough so that the radius of the circle is much smaller than $E \cdot t$, i.e. the distance between the new rotation centre and the origin, the flux linkage estimate $\hat{\lambda}$ points approximately in the direction of

the offset vector E. This is the reason why the estimated angle dwells around a constant with the open-loop integrator approach.

5.2.1.2 Flux Linkage Estimation Constrained on the Circular Locus

A logical solution for the DC-drift problem of the open-loop integration method is to constrain the flux linkage estimate on the origin-centered circular locus during the integration. To achieve this, it is necessary to recall the electrical machine equation 3.5. The differential term of the current is ignored again due to the tiny value of the inductance. According to equation 3.5, the back-EMF vector $(e_\alpha, e_\beta)^T$ in the α-β coordinate system is defined as:

$$e_\alpha = -\omega_r \Psi_{pm} \sin\theta_d = U_\alpha - R \cdot I_\alpha$$
$$e_\beta = \omega_r \Psi_{pm} \cos\theta_d = U_\beta - R \cdot I_\beta$$

$$(5.3)$$

And it is clear that the back-EMF defined in equation 5.3 is the time derivative of the flux linkage, i.e.:

$$\dot{\lambda}_\alpha = e_\alpha$$
$$\dot{\lambda}_\beta = e_\beta$$

$$(5.4)$$

The geometrical relation between the back-EMF and the flux linkage in the ideal case is depicted in figure 5.2. The flux linkage is moving along the origin-centered circular locus with the radius Ψ_{pm}. The back-EMF is the tangential velocity vector of the moving flux linkage vector. However, the measurement of the back-EMF vector $(\bar{e}_\alpha, \bar{e}_\beta)^T$ contains an offset error vector E:

$$\bar{e}_\alpha = \bar{U}_\alpha - R \cdot \bar{I}_\alpha = e_\alpha + E_\alpha$$
$$\bar{e}_\beta = \bar{U}_\beta - R \cdot \bar{I}_\beta = e_\beta + E_\beta$$

$$(5.5)$$

And since the open-loop integration method still estimates the flux linkage $(\hat{\lambda}_\alpha, \hat{\lambda}_\beta)$ basing on the equation 5.4, i.e.:

$$\dot{\hat{\lambda}}_\alpha = \bar{e}_\alpha$$
$$\dot{\hat{\lambda}}_\beta = \bar{e}_\beta$$

$$(5.6)$$

the measurement offset E leads to the error that the flux linkage estimate drifts away from the origin-centered locus.

In figure 5.2, the offset error vector E is decomposed into a tangential component and a radial component. The radial component of E is the actual cause that brings the flux linkage estimate away from the origin-centered locus. Therefore, the problem to constrain the flux linkage estimate on the origin-centered locus is actually the compensation of the radial component of the offset vector E.
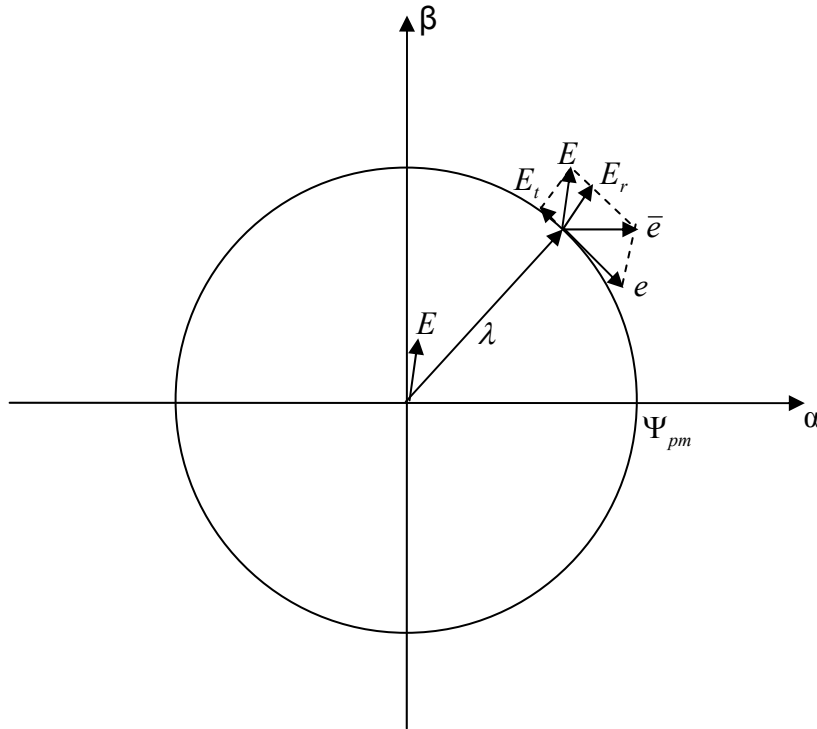
λ   The flux linkage vector

e The back-EMF vector

E The measurement offset vector

$\bar{e}$ The measured back-EMF, which is the vectorial sum of e and E

E_r The radial component of vector E

E_t The tangential component of vector E

Figure 5.2: illustration of the geometrical relation between the flux linkage, the back-EMF and the offset error vector in the α-β coordinate system.

Two approaches to compensate the tangential component of the offset vector E are introduced here.

Closed-loop compensation

The basic idea of this method is to 'control' the flux linkage estimate to move on the origin-centered circle. If the amplitude of the flux linkage estimate exceeds the radius of the circle, i.e. $\left|\hat{\lambda}\right| > \Psi_{pm}$; a vector component *pointing in the opposite direction of* $\hat{\lambda}$ is added to the measured back-EMF vector $\bar{e}$. If the amplitude of the flux linkage estimate is smaller than the radius of the circle, the opposite will be carried out. The compensation method can be expressed mathematically by equation 5.7.

$$\dot{\hat{\lambda}} = \bar{e} - k \cdot \left(\left|\hat{\lambda}\right| - \Psi_{pm}\right) \cdot \frac{\hat{\lambda}}{\left|\hat{\lambda}\right|} \tag{5.7}$$

The parameter k is a positive constant, which determines the convergence speed of the closed-loop correction. Without the derivation, it can be proved that:

$$\left|\dot{\hat{\lambda}}\right| = \bar{e} \bullet \frac{\hat{\lambda}}{\left|\hat{\lambda}\right|} - k\left(\left|\hat{\lambda}\right| - \Psi_{pm}\right) \tag{5.8}$$

It should be noted that the left-hand side is the derivative of the norm of $\hat{\lambda}$, not the norm of $\dot{\hat{\lambda}}$. The first term on the right-hand side (dot-product) is the amplitude of the orthogonal projection of $\bar{e}$ on the direction of $\hat{\lambda}$. If the measurement of the back-EMF vector is ideal, this amplitude should be zero since the vectors $\hat{\lambda}$ and $\bar{e}$ are perpendicular to each other. Due to the measurement offset vector E, this term will have a small value proportional to the amplitude of E. Let's define the amplitude upper-bond of this term as M ($M>0$), i.e.:

$$-M \leq \bar{e} \bullet \frac{\hat{\lambda}}{\left|\hat{\lambda}\right|} \leq M \tag{5.9}$$

Combining equation 5.8 and 5.9 we can obtain the following relation:

$$-k \cdot \left[\left|\hat{\lambda}\right| - \left(\Psi_{pm} - \frac{M}{k}\right)\right] \leq \left|\dot{\hat{\lambda}}\right| \leq -k \cdot \left[\left|\hat{\lambda}\right| - \left(\Psi_{pm} + \frac{M}{k}\right)\right] \tag{5.10}$$

Again note that $\left|\dot{\hat{\lambda}}\right|$ is the derivative of the norm of $\hat{\lambda}$. The inequality 5.10 shows that the compensation method expressed by equation 5.7 is able to confine the amplitude of the flux linkage estimate $\left|\hat{\lambda}\right|$ within a band symmetric to Ψ_{pm} (figure 5.3); i.e.:

$$\Psi_{pm} - \frac{M}{k} \leq \left|\hat{\lambda}\right| \leq \Psi_{pm} + \frac{M}{k} \qquad (5.11)$$

And if the positive parameter k is chosen big enough, the flux linkage estimate $\hat{\lambda}$ moves approximately on the origin-centered circular locus with the radius Ψ_{pm}.
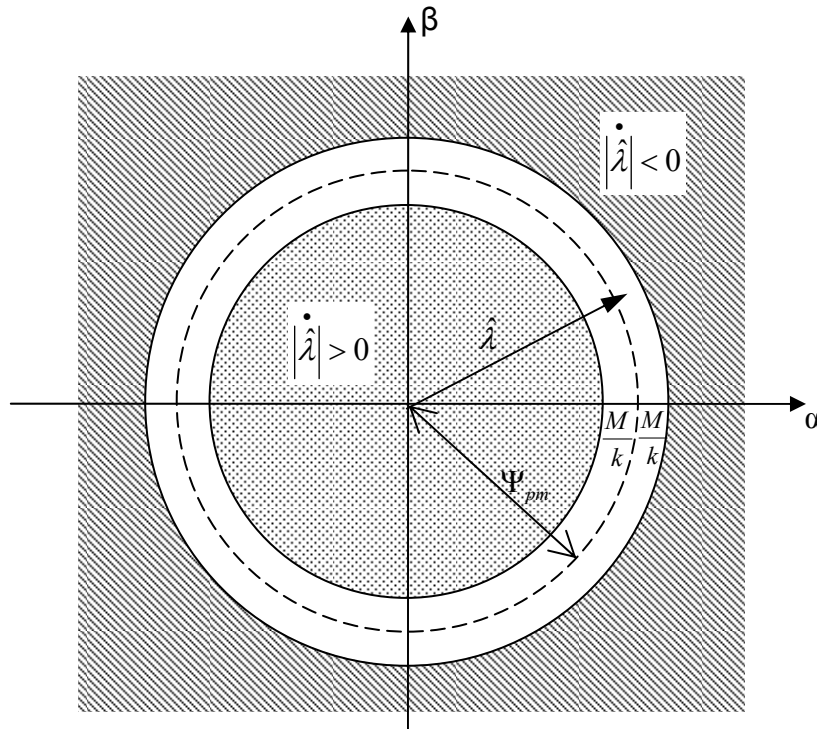
Figure 5.3: the compensation method of equation 5.7 confines the flux linkage estimate $\hat{\lambda}$ within a symmetric band along the circular locus.

Closed-loop Integrator with Amplitude Limiter

Hu and Wu [21] proposed a flux linkage estimation approach in 1998 using closed-loop integrator with amplitude limiter. The basic idea of this approach is to convert the open-loop integrator into an equivalent closed-loop structure and place an internal limiter in the closed-loop so that the amplitude of the flux linkage estimate $\left|\hat{\lambda}\right|$ is constrained in the vicinity of Ψ_{pm}. The figure 5.4 shows the equivalent closed-loop structure of an integrator. And figure 5.5 illustrates the estimation method.
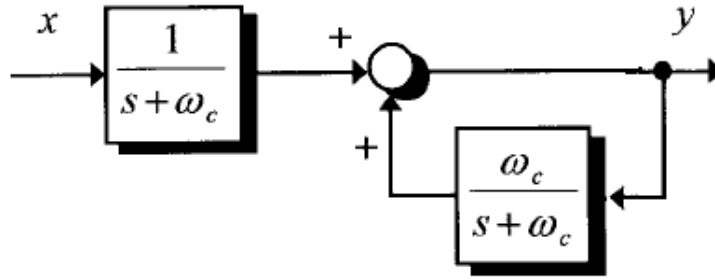
Figure 5.4: an integrator in the form of a closed-loop structure with two first-order delay elements [21]
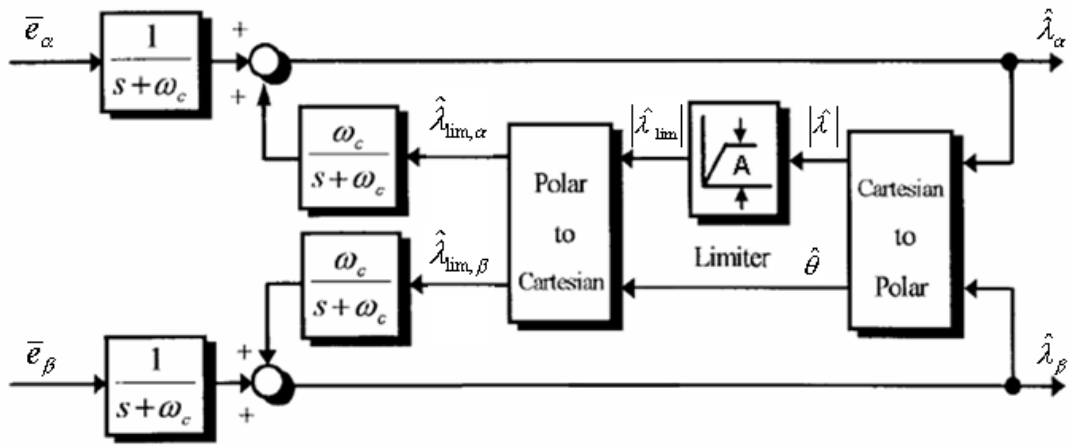

Figure 5.5: the second algorithm introduced by Hu and Wu [21]. The limiter limits the amplitude of the flux linkage estimate.

It can be seen in figure 5.5 that this algorithm is basically the integration of the measured back-EMF vector. The amplitude limiter is added to the feedback of the flux linkage estimate. The algorithm in figure 5.5 can be mathematically expressed by equation 5.12.

$$\mathcal{L}\{\hat{\lambda}\} = \frac{1}{s + \omega_c} \cdot \mathcal{L}\{\overline{e}\} + \frac{\omega_c}{s + \omega_c} \cdot \mathcal{L}\{\hat{\lambda}_{\text{lim}}\} \tag{5.12}$$

The operator 'L' indicates the Laplace transformation, and ω_c is a positive constant. In time domain, the algorithm is:

$$\dot{\hat{\lambda}} = \overline{e} - \omega_c \left(\hat{\lambda} - \hat{\lambda}_{\text{lim}} \right) \tag{5.13}$$

The resemblance between equation 5.13 and equation 5.7 can be noticed easily if we rewrite equation 5.7 in the following form:

$$\dot{\hat{\lambda}} = \bar{e} - k \cdot \left(\hat{\lambda} - \Psi_{pm} \cdot \frac{\hat{\lambda}}{|\hat{\lambda}|} \right) \tag{5.14}$$

Actually both methods are the same if the limiter in Hu's method [21] is replaced by setting $\left|\hat{\lambda}_{\text{lim}}\right|$ equal to the constant Ψ_{pm}; i.e.:

$$\left|\hat{\lambda}_{\text{lim}}\right| = \Psi_{pm}; \text{and}$$
$$\hat{\lambda}_{\text{lim}} = \Psi_{pm} \cdot \begin{pmatrix} \cos\hat{\theta} \\ \sin\hat{\theta} \end{pmatrix} = \Psi_{pm} \cdot \frac{\hat{\lambda}}{|\hat{\lambda}|} \tag{5.15}$$

Although the positive constant ω_c is referred to as cut-off frequency in [21], it actually functions the same as the amplification factor k in equation 5.7, which adjusts the convergence speed of the compensation and determines the tolerance of the compensation (figure 5.3). In [21], the author only set an upper bond to the amplitude of the flux linkage estimate $\left|\hat{\lambda}\right|$. This is not sufficient. Because depending on the angle of the flux linkage λ, the error vector E (figure 5.2) is not always pointing *outwards* of the origin-centered circle. If the flux linkage happens to dwell around the opposite direction of E, in which case the error vector E points *towards* the origin; the error vector E will cause an angle estimation error of about 180 within very short time. Since the flux linkage estimate $\hat{\lambda}$ can freely travel within the circle. Therefore, it is also necessary to set a lower bond to $\left|\hat{\lambda}\right|$. The question is what values the upper- and lower-bonds should take. These two boundaries set a tolerance band to the value Ψ_{pm}. Considering the inequality 5.10 by replacing k with ω_c, it can be understood that this tolerance band is actually 'wrapped' by another tolerance band whose width is determined by the value of ω_c (same as the tolerance band shown in figure 5.3). The tolerance band allowed by these boundaries actually worsens the effect of the compensation. Therefore, both the upper- and lower-bonds are set to Ψ_{pm} during the simulation and the test bench experiment, which means the two compensation methods are equivalent.
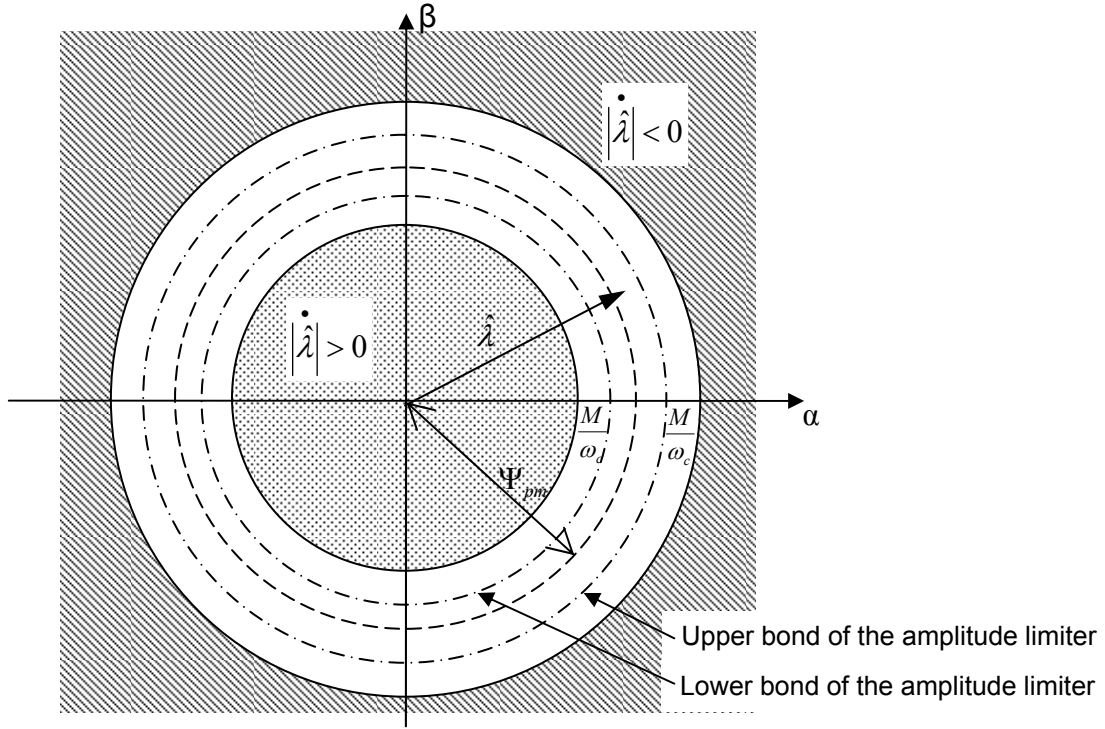
Figure 5.6: the tolerance band allowed by the upper- and lower-bond of the amplitude limiter is 'wrapped' by another tolerance band whose width is determined by ω_c (compare with figure 5.3).

So far it has been discussed how the radial component of the error vector E can be compensated. However the tangential component E_t still remains (figure 5.2) and causes error in the flux linkage estimate. The flux linkage estimation with compensation of the radial error component E_r integrates the sum of the back-EMF vector and the tangential error component E_t. The amplitude of the tangential component E_t varies depending on the angle of the flux linkage vector λ (figure 5.7). At high rotor speed, the amplitude of E_t is not significant in comparison to the amplitude of the back-EMF. But at low rotor speed, the rotation of the flux linkage estimate $\hat{\lambda}$ is strongly influenced by the tangential error component. This explains the observation mentioned in [21] that the algorithm had better performance at high rotor speed than at low rotor speed. The tangential error E_t tends to bring the estimated angle away from its real value to a constant angle which is defined by the direction of the offset error vector E (figure 5.7). This is understandable considering the orientation of the tangential component E_t along the circle (figure 5.7). This can cause a maximal electrical angle error of 180°, or a mechanical angle error of 90°. And the angle estimation error can not be deliberately corrected without closed-loop angle estimation methods. The advantage of the flux linkage estimation method is its open-loop na-

ture, which guarantees the stability of the estimation. It should also be noted that the error caused by the tangential error component E_t will compensate itself partly or completely if the rotor rotates across the neutral line shown in figure 5.7. This explains why the average angle estimation error is much smaller if the rotor rotates continuously more than a circumference.
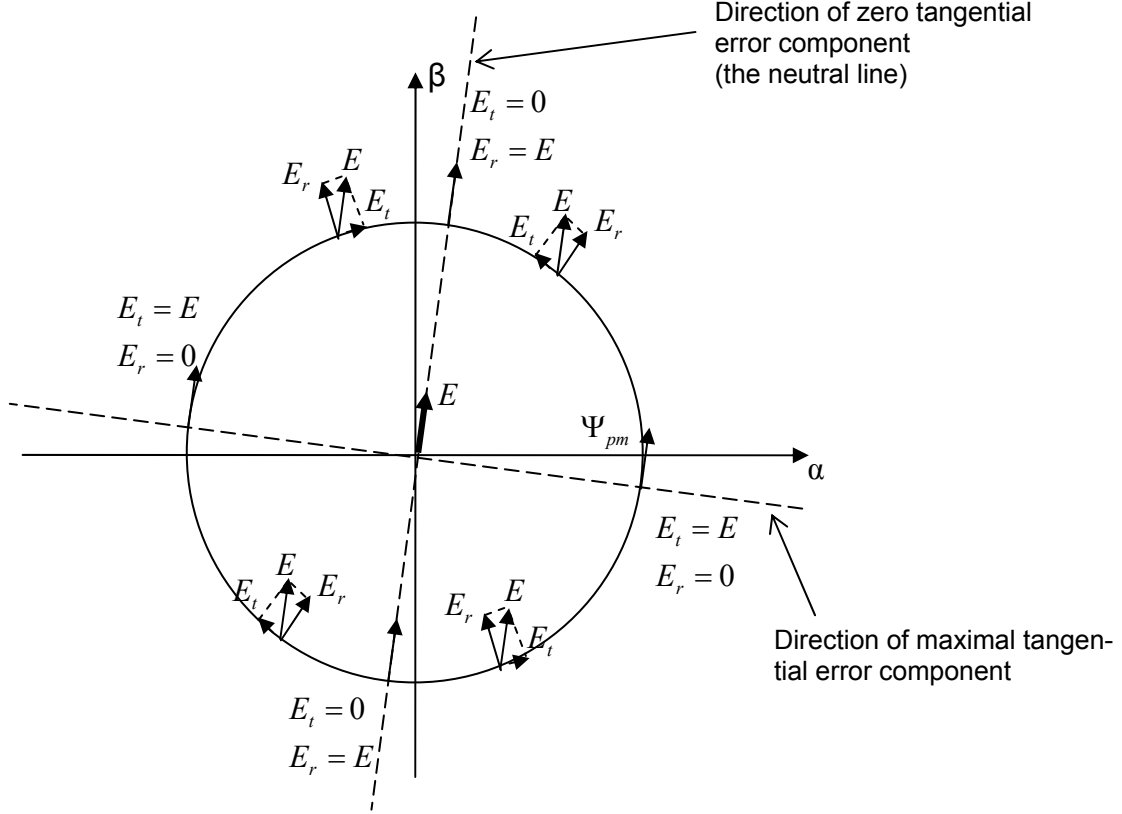
Figure 5.7: the tangential component E_t of the offset error vector *E*. The tangential error component E_t tends to bring the estimated angle to the direction of *E*.

### 5.2.1.3 The Simulation Results of the Flux Linkage Estimation Methods

The performance of the open-loop integration method and the method with E_r compensation are compared in the simulation. The upper figure of figure 5.8 shows the simulation result of the both angle estimation methods in a sinus operation. The estimation with the open-loop integrator soon dwells around the direction of the offset error vector *E* (-1.675 rad), which is injected in the simulation by injecting a current measurement error vector in the opposite direction. The reason of this behavior had been explained in subsection 5.2.1.1 with figure 5.1. While with E_r compensation; the angle estimation is very precise. The angle estimation error of the estimation with

E_r compensation is shown in the lower figure of figure 5.8. The angle error passes periodically through zero because the rotor rotates periodically across the neutral line in figure 5.7 and the tangential error component E_t compensates itself.
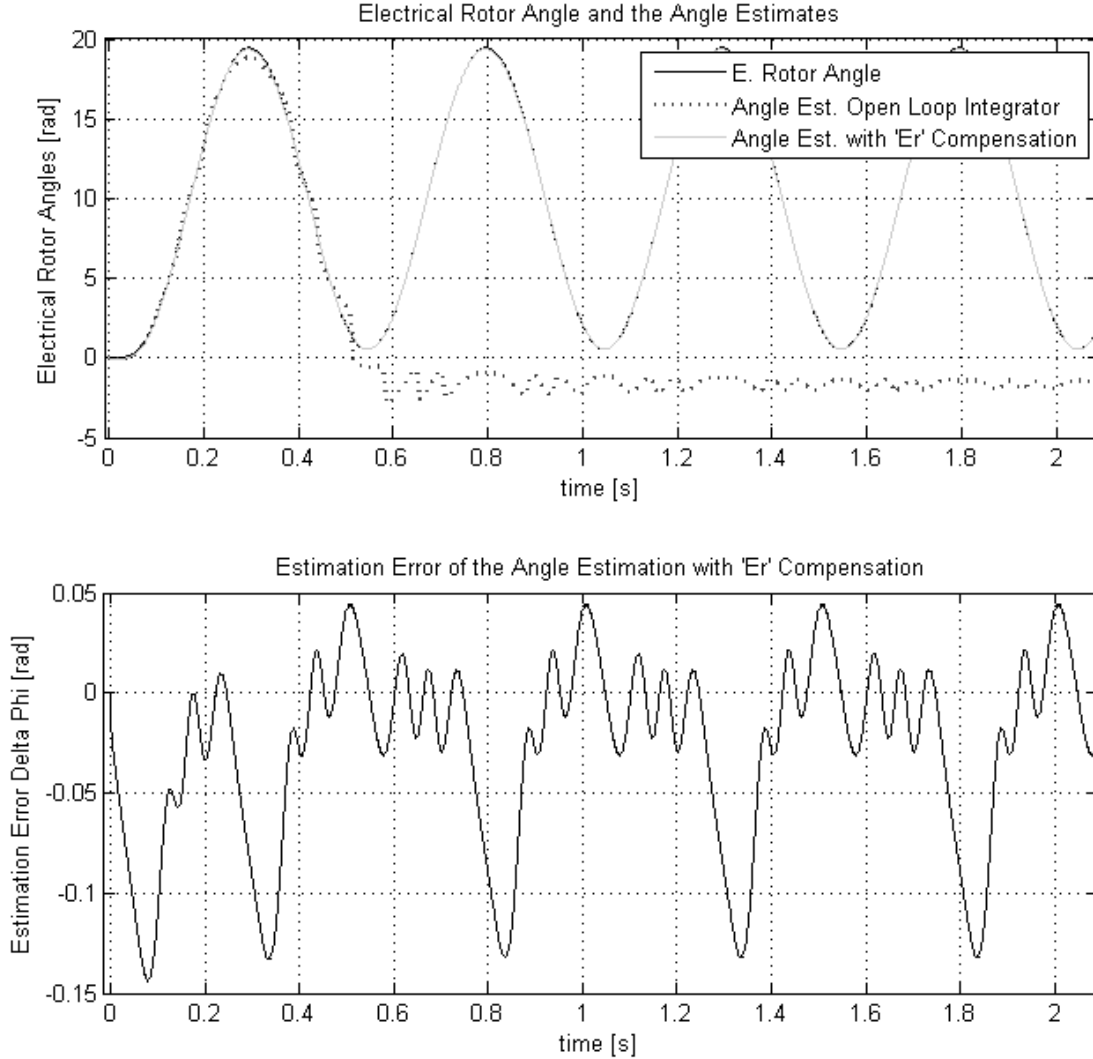
Figure 5.8: the upper figure shows the simulation result of the both angle estimation methods in a sinus operation. The angle estimation error of the estimation with E_r compensation is shown in the lower figure.

The locus of the flux linkage estimate of the open-loop integration and the estimation with E_r compensation is shown in figure 5.9. The locus of the open-loop integration drifts in the direction of the offset error vector E (-1.675 rad). The black curve is the locus of the flux linkage estimate with E_r compensation. It is successfully constrained on the origin-centered circle with the radius Ψ_{pm} (0.004 Vs).
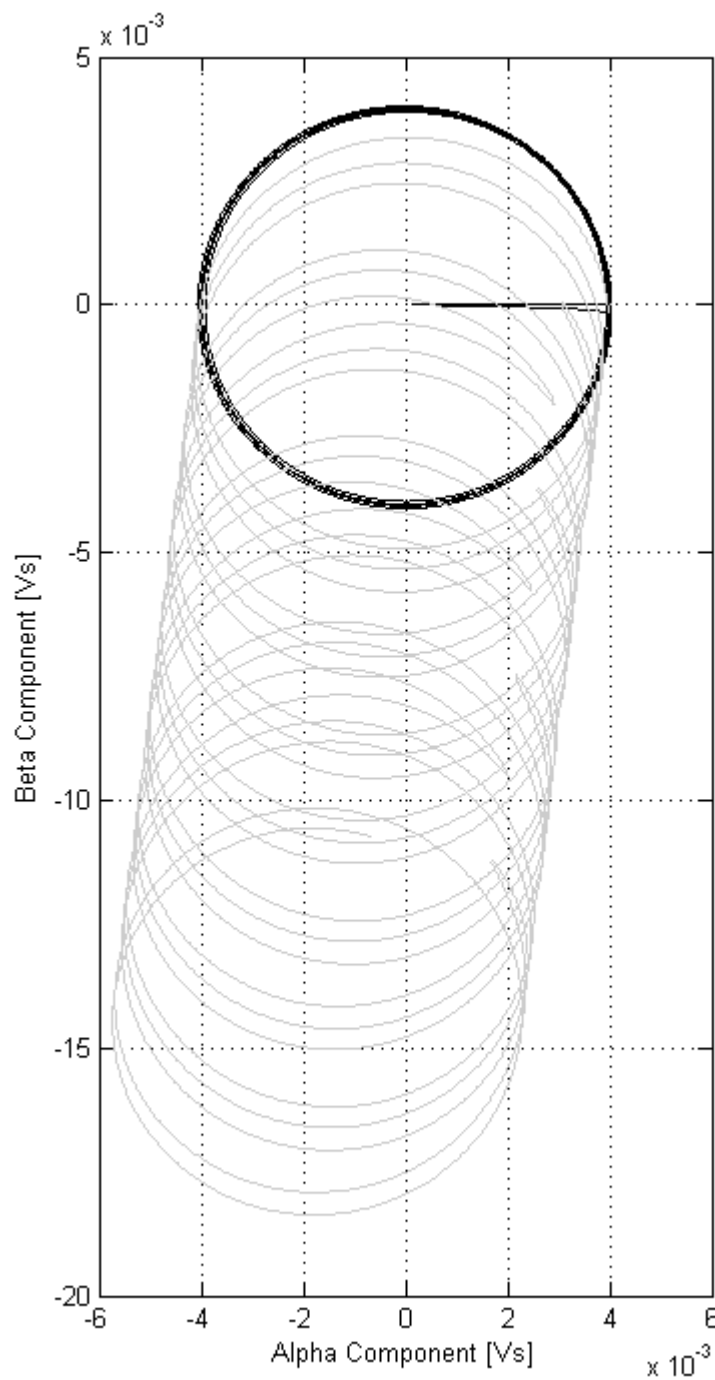
Figure 5.9: the locus of the flux linkage estimate of the open-loop integration and the estimation with E_r compensation. The grey curve is the locus of the open-loop integration. The black curve is the locus of the flux linkage estimate with E_r compensation.

If the rotor does not rotate across the neutral line shown in figure 5.7; the angle error caused by the tangential error component E_t accumulates until the angle estimate

remains in the direction of the error vector E (-1.675 rad). A typical situation is rotor standing still. The simulation of the drift in this case is shown in figure 5.10.
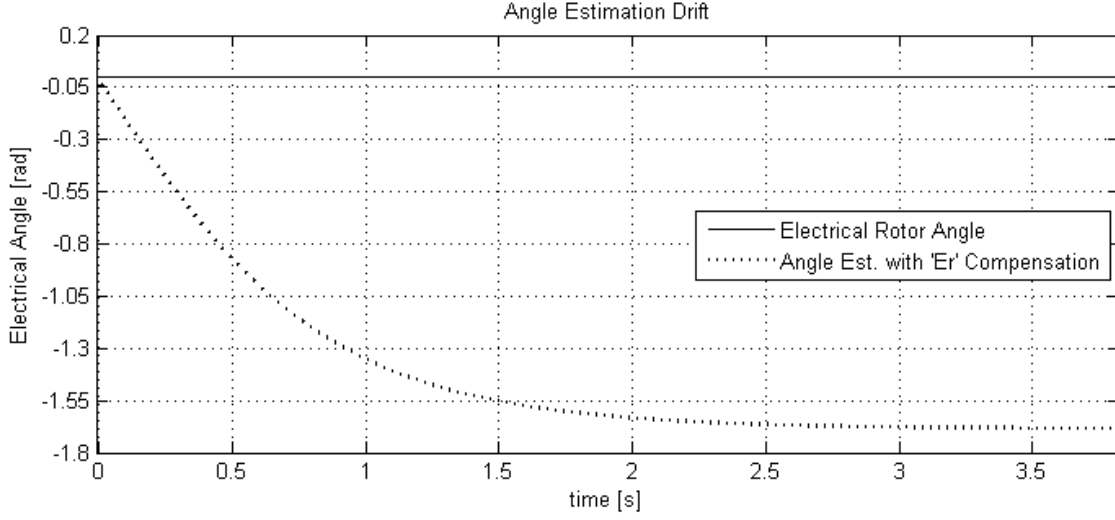
Figure 5.10: the drift of the estimated electrical angle with E_r.compensation. It can be seen that the estimated angle drifts to the direction of the offset error vector E (-1.675 rad), which is injected in the simulation.

5.2.2 Back-EMF-Based Rotor Angle Estimation

The back-EMF is another physical phenomenon that can be applied in the passive rotor angle estimation. The back-EMF vector is perpendicular to the direction of the rotor magnet flux (equation 3.5), i.e. aligned with the q-axis (figure A.1). In other words, the back-EMF vector is a function of the rotor angle.

Estimation methods basing on back-EMF do not necessarily estimate the back-EMF directly. For example, methods utilizing the extended Kalman filter (EKF) only implicitly exploit this physical effect and the state vector does not contain the back-EMF terms [32]. The other back-EMF based methods estimate the back-EMF vector either in the stator-fixed α-β coordinate system or in the arbitrary dc-qc coordinate system (figure A.1).

In the stator-fixed α-β coordinate system, the back-EMF vector is a function of the rotor angle:

$$\begin{pmatrix} e_\alpha \\ e_\beta \end{pmatrix} = \begin{pmatrix} -\omega_r \Psi_{pm} \sin\theta_d \\ \omega_r \Psi_{pm} \cos\theta_d \end{pmatrix}$$

Observer basing on the machine equation 3.5 can be used to estimate this vector and the rotor angle θ_d can be calculated from this back-EMF vector directly.

In the arbitrary dc-qc coordinate system, the machine equation becomes:

$$\begin{pmatrix} U_{dc} \\ U_{qc} \end{pmatrix} = \begin{pmatrix} L & 0 \\ 0 & L \end{pmatrix} \begin{pmatrix} \dfrac{di_{dc}}{dt} \\ \dfrac{di_{qc}}{dt} \end{pmatrix} + \begin{pmatrix} R & -\omega_1 L \\ \omega_1 L & R \end{pmatrix} \begin{pmatrix} i_{dc} \\ i_{qc} \end{pmatrix} + \begin{pmatrix} \omega_r \Psi_m \sin\Delta\theta \\ \omega_r \Psi_m \cos\Delta\theta \end{pmatrix} \quad (5.16)$$

By comparing equation 5.16 to equation 3.5, two differences can be noticed. First, the electrical rotor speed ω_r in the second term on the right-hand side of equation 3.5 is replaced by the estimated speed ω_1 in equation 5.16. The second difference is the expression of the back-EMF vector. The back-EMF vector is now a function of the angle $\Delta\theta$ between the d-axis and the dc-axis (figure A.1), i.e. the angle estimation error:

$$\begin{pmatrix} e_{dc} \\ e_{qc} \end{pmatrix} = \begin{pmatrix} \omega_r \Psi_{pm} \sin\Delta\theta \\ \omega_r \Psi_{pm} \cos\Delta\theta \end{pmatrix}$$

The back-EMF in this form can be either approximated by ignoring the current dynamics [25] or be estimated with observer [26][30][31]. The rotor angle can be calculated by correcting the angle of the dc-axis with the knowledge of $\Delta\theta$.

The classification of the back-EMF-based angle estimation methods is shown in figure 5.11. In this subsection, an example is provided for each of the category of methods shown in figure 5.11. The simulation results are presented. And their performance will be compared.
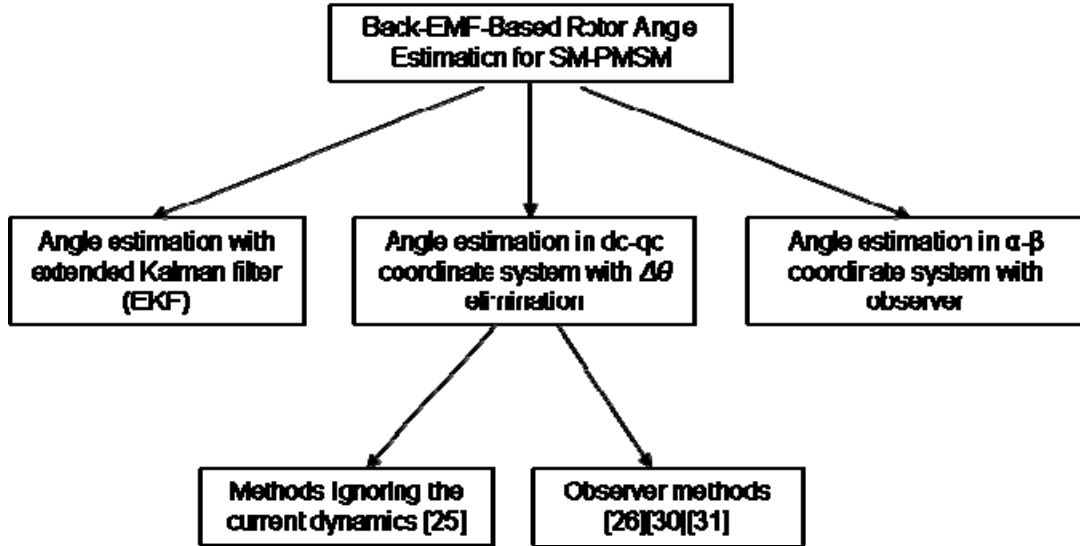
Figure 5.11: the classification of back-EMF-based angle estimation.

5.2.2.1 Rotor Angle Estimation with Extended Kalman Filter (EKF)

The extended Kalman filter approach is one of the most sophisticated methods for rotor angle estimation [32][34][35][36][38][39]. This category of estimation method combines the electrical and mechanical machine equations in one system equation and estimates the rotor angle directly as an element in the state vector. This subsection makes a brief introduction on EKF and the applied system model. The parameter tuning of EKF has been raised in the literature as an analytically still unsolved problem [32]. The parameter tuning in the simulation follows the guidelines summarized in [32].

Extended Kalman Filter (EKF)

The Extended Kalman Filter (EKF) is an approximation of the Kalman Filter for non-linear system. EKF linearizes the non-linear system about the estimated state and the system input in each step, ignoring both the process noise and the measurement noise during the linearization, and treats the system as a linear system. The non-linear system is described by the stochastic difference equation:

$$
\begin{aligned}
x_k &= f(x_{k-1}, u_{k-1}, w_{k-1}) \\
z_k &= h(x_k, v_k)
\end{aligned}
\tag{5.17}
$$

The covariance matrix of the process noise w_k is denoted as Q and the covariance matrix of the measurement noise v_k is denoted as R. By ignoring the process noise and the measurement noise, the a priori state estimation and the a priori system output estimation are:

$$\hat{x}_k^- = f(\hat{x}_{k-1}, u_{k-1}, 0)$$
$$\hat{z}_k^- = h(\hat{x}_k^-, 0)$$

(5.18)

The linear approximation of the system equation 5.17 in the calculation step k is given by the first order Taylor expansion of equation 5.17 about the point $(\hat{x}_{k-1}, u_{k-1}, 0)$ for the state equation and $(\hat{x}_k^-, 0)$ for the output equation respectively:

$$x_k \approx \hat{x}_k^- + A_k(x_{k-1} - \hat{x}_{k-1}) + W_k w_{k-1}$$
$$z_k \approx \hat{z}_k^- + H_k(x_k - \hat{x}_k^-) + V_k v_k$$

(5.19)

The Jacobian matrixes A_k, W_k, H_k, V_k in the step k are calculated by:

$$A_k = \left[a_{ij} = \frac{\partial f_i}{\partial x_j}(\hat{x}_{k-1}, u_{k-1}, 0) \right]$$

$$W_k = \left[w_{ij} = \frac{\partial f_i}{\partial w_j}(\hat{x}_{k-1}, u_{k-1}, 0) \right]$$

$$H_k = \left[h_{ij} = \frac{\partial h_i}{\partial x_j}(\hat{x}_k^-, 0) \right]$$

$$V_k = \left[v_{ij} = \frac{\partial h_i}{\partial v_j}(\hat{x}_k^-, 0) \right]$$

(5.20)

The algorithm of the EKF is illustrated in figure 5.12. Due to the calculation of the matrix inversion, the calculation effort per step is very high.

The Machine Model for EKF-based Rotor Angle Estimation

Since the current measurement in the d-q coordinate system is not possible (system output measurement) without the rotor angle, only the machine model in the stator-fixed α-β coordinate can be applied for EKF-based rotor angle estimation.

$$x_k = A \cdot x_{k-1} + B \cdot u_{k-1} + w_{k-1}$$
$$z_k = H \cdot x_k + v_k$$

$$x_k = \left[i_{\alpha,k}, i_{\beta,k}, \omega_{r,k}, \theta_{el,k} \right]^T$$
$$u_k = \left[u_{\alpha,k}, u_{\beta,k} \right]^T$$
$$z_k = \left[i_{\alpha,k}, i_{\beta,k} \right]^T$$

$$A = \begin{bmatrix} 1 - \dfrac{T \cdot R}{L} & 0 & \dfrac{T \cdot \Psi_{pm}}{L} \sin\theta_{el} & 0 \\ 0 & 1 - \dfrac{T \cdot R}{L} & -\dfrac{T \cdot \Psi_{pm}}{L} \cos\theta_{el} & 0 \\ 0 & 0 & 1 & 0 \\ 0 & 0 & T & 1 \end{bmatrix} ; B = \begin{bmatrix} \dfrac{T}{L} & 0 \\ 0 & \dfrac{T}{L} \\ 0 & 0 \\ 0 & 0 \end{bmatrix} ; H = \begin{pmatrix} 1 & 0 & 0 & 0 \\ 0 & 1 & 0 & 0 \end{pmatrix}$$

$$(5.21)$$

The discrete system model is described by equation 5.21, which is the approximation of the electrical machine equation 3.5 and the mechanical equation 3.8 with first order Eular method. The rotor speed change during the small sampling interval (100 μs) is ignored. To reduce the computation effort, it is assumed that both the process noise and measurement noise is additive, i.e. their covariance matrixes Q and R remain constant during the innovation. It should be noted that the matrix A is also a function of the state variable because the estimated rotor angle is involved.

Extension of the system state vector with the phase resistance [40] or the mechanical loading moment [32] can also be found in the literature. But due to the high computation demand, these extensions are not practical for the computation hardware in our brake system.

The Parameter Tuning of EKF

The parameter tuning of EKF appears to be a tricky step. Although some suggestions had been made in [32][33] for the parameter tuning problem, there is no general procedure till today. A good summary can be found in [32] over the recommendations for EKF parameter tuning in the literature. The parameter tuning in the simulation follows these recommendations. The recommendations in [32] are listed here:

- Initial values of the terms of the system covariance matrix P_0 can often be selected equal zero. If the initial values must be tuned (in order to improve the filter performance at the filter start-up), only the diagonal terms are usually

taken into account. The initial values of the matrix *P* do not affect the transient durations as well as the filter steady-state behaviour.

- Due to the lack of statistical information about the drive system and especially in order to simplify the tuning process, the covariance matrices *Q* and *R* are considered to be diagonal and, moreover, invariant. It means that all the terms out of the main diagonal are considered to be zero.

- The EKF works with the square errors. The covariance matrices represent mean square error of corresponding quantities. This knowledge helps to define the initial values of the tuned covariance matrices *Q* and *R*.

- The filter convergence and stability is much more sensitive to the terms of the covariance matrix *Q* than *R*.

- Increasing values of the terms of the matrix *Q* correspond to the less exact machine model. In such case, the measured values are more accented via Kalman gain *K*.

- Increasing values of the terms of the matrix *R* correspond to the less exact measurement results. In such case, the machine model is more accented.

- Big differences between the terms of the matrices *Q* and *R* can lead to the filter divergence.

In the simulation, the initial value of the covariance matrix P_0 is chosen to be zero because the system state at the beginning of the estimation is known (motor stands still). The covariance matrixes *Q* and *R* are set to be 4-by-4 respectively 2-by-2 diagonal matrixes. And because the error actually occurs in the current measurement, the tuning is focused on the covariance matrix *R*. It should be noted that the covariance matrix *Q* must not be set as zero matrix. Otherwise the estimation will be instable because the ratio between the diagonal elements of *Q* and *R* is infinitive.
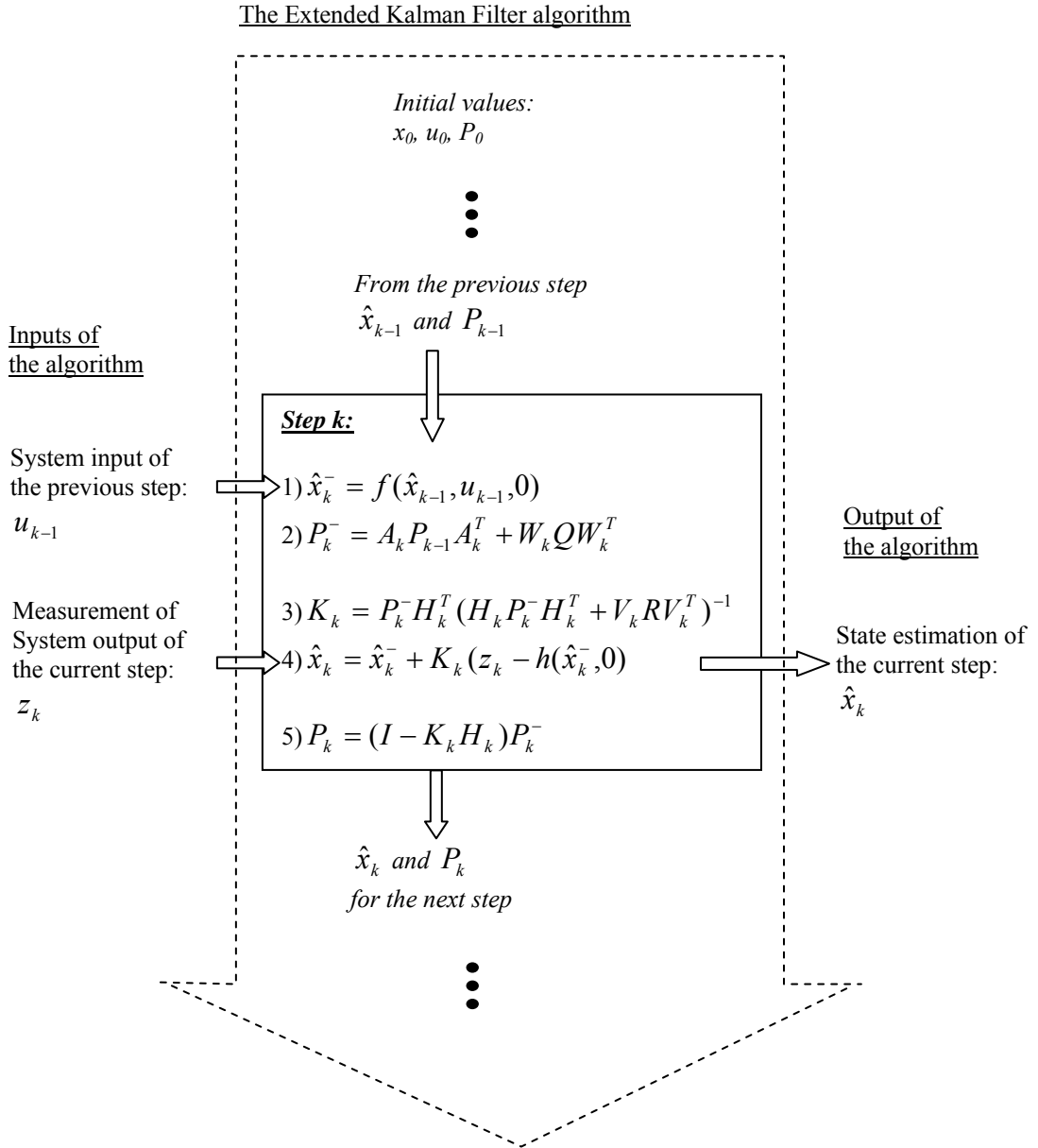
> The noise covariance **Q** and **R** should be tuned.

The Extended Kalman Filter algorithm

Initial values:
$x_0,\ u_0,\ P_0$

⋮

From the previous step
$\hat{x}_{k-1}\ and\ P_{k-1}$

Inputs of the algorithm

Step k:

System input of the previous step:

u_{k-1}

1) $\hat{x}_k^- = f(\hat{x}_{k-1}, u_{k-1}, 0)$

2) $P_k^- = A_k P_{k-1} A_k^T + W_k Q W_k^T$

Output of the algorithm

Measurement of System output of the current step:

z_k

3) $K_k = P_k^- H_k^T (H_k P_k^- H_k^T + V_k R V_k^T)^{-1}$

4) $\hat{x}_k = \hat{x}_k^- + K_k(z_k - h(\hat{x}_k^-, 0))$

State estimation of the current step:

$\hat{x}_k$

5) $P_k = (I - K_k H_k)P_k^-$

$\hat{x}_k\ and\ P_k$
for the next step

⋮

Figure 5.12: The algorithm of Extended Kalman Filter.

5.2.2.2 The Direct Position Error Estimation of Sakamoto

The direct position error estimation is published by K.Sakamoto in [25] in 2001. The estimation method basically approximate the back-EMF in the dc-qc coordinate by ignoring the derivative of the current signals (open-loop estimator) and eliminates the angle error $\Delta\theta$ with a PLL controller. Figure 5.13 illustrates the algorithm of Sakamoto.

By ignoring the current derivative in equation 5.16, the back-EMF is approximated by the equation 5.22:

$$
\begin{pmatrix} e_{dc} \\ e_{qc} \end{pmatrix} = \begin{pmatrix} \omega_r \Psi_{pm} \sin \Delta\theta \\ \omega_r \Psi_{pm} \cos \Delta\theta \end{pmatrix} = \begin{pmatrix} U_{dc} \\ U_{qc} \end{pmatrix} - \begin{pmatrix} R & -\omega_1 L \\ \omega_1 L & R \end{pmatrix} \begin{pmatrix} i_{dc} \\ i_{qc} \end{pmatrix}
\tag{5.22}
$$

The angle estimation error is calculated by equation 5.23:

$$
\Delta\theta = \tan^{-1}\left(\frac{e_{dc}}{e_{qc}}\right) = \tan^{-1}\left[\frac{U_{dc} - R \cdot i_{dc} + \omega_1 L \cdot i_{qc}}{U_{qc} - R \cdot i_{qc} - \omega_1 L \cdot i_{dc}}\right]
\tag{5.23}
$$

This approximation is invalid if $e_{qc} = 0$. This corresponds to two possibilities: either the rotor speed $\omega_r = 0$, or $\Delta\theta = 2k\pi \pm \pi/2$ (k is an arbitrary integer). The first situation is the common problem of back-EMF-based estimation, i.e. the estimation fails at zero rotor speed because the back-EMF vanishes. The second situation poses a restriction on the approximation of the estimation error $\Delta\theta$, namely, $-\pi/2 < \Delta\theta < \pi/2$. This condition can be held only if the closed-loop estimation converges fast enough. The PLL controller in figure 5.13 is a PI-controller that manipulates the rotation speed ω_1 of the dc-qc coordinate so that $\Delta\theta$ can be eliminated.
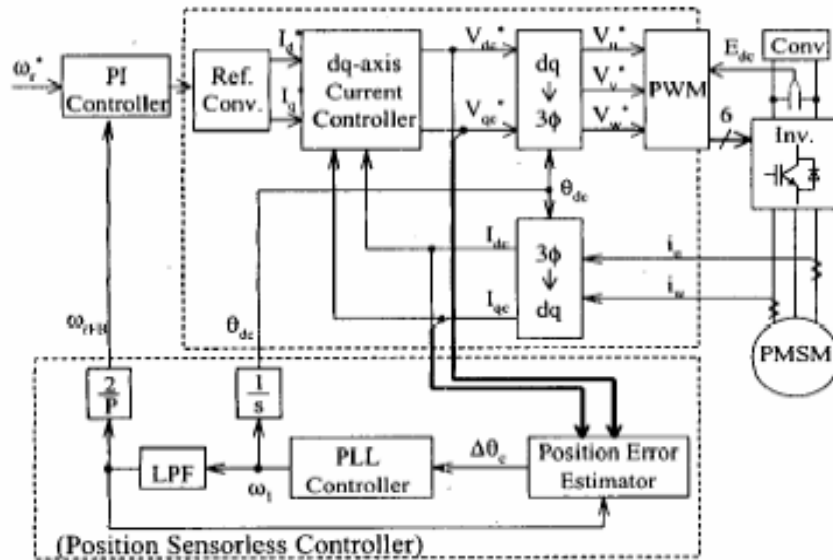

Figure 5.13: the structure of the direct position error estimation of K.Sakamoto [25].

This angle estimation method can achieve very fast convergence by properly adjusting the parameters of the PLL controller. However, neglecting the current dynamics

produces bigger estimation error in the approximated back-EMF vector in operation with fast torque variation.

5.2.2.3 Back-EMF Estimation in dc-qc Coordinate with Observer

This category of rotor angle estimation approaches [26][30][31] estimates the back-EMF in dc-qc coordinate with observer and aligns the dc-axis to the d-axis by correcting its angle with the angle error $\Delta\theta$, which is calculated from the back-EMF estimate. Compared to the method of Sakamoto [25], this type of methods also considers the current derivative.

With the widely applied assumption that the rotor speed change is much slower than the current change. The derivative of the back-EMF vector in the dc-qc coordinate system can be approximated by:

$$\begin{pmatrix} \dot{e}_{dc} \\ \dot{e}_{qc} \end{pmatrix} = \begin{pmatrix} (\omega_1 - \omega_r) \cdot \omega_r \Psi_{pm} \cos\Delta\theta \\ (\omega_r - \omega_1) \cdot \omega_r \Psi_{pm} \sin\Delta\theta \end{pmatrix} = \begin{pmatrix} (\omega_1 - \omega_r) \cdot e_{qc} \\ (\omega_r - \omega_1) \cdot e_{dc} \end{pmatrix} \tag{5.24}$$

If the estimated rotor speed nearly coincides with the rotor speed, i.e. $\omega_1 \approx \omega_r$. It can be further assumed that:

$$\begin{pmatrix} \dot{e}_{dc} \\ \dot{e}_{qc} \end{pmatrix} \approx \begin{pmatrix} 0 \\ 0 \end{pmatrix} \tag{5.25}$$

With this assumption, the following system equation can be established basing on equation 5.16:

$$\begin{pmatrix} \dot{i}_{dc} \\ \dot{e}_{dc} \\ \dot{i}_{qc} \\ \dot{e}_{qc} \end{pmatrix} = \begin{pmatrix} -\dfrac{R}{L} & -\dfrac{1}{L} & \omega_1 & 0 \\ 0 & 0 & 0 & 0 \\ -\omega_1 & 0 & -\dfrac{R}{L} & -\dfrac{1}{L} \\ 0 & 0 & 0 & 0 \end{pmatrix} \cdot \begin{pmatrix} i_{dc} \\ e_{dc} \\ i_{qc} \\ e_{qc} \end{pmatrix} + \begin{pmatrix} \dfrac{1}{L} & 0 \\ 0 & 0 \\ 0 & \dfrac{1}{L} \\ 0 & 0 \end{pmatrix} \cdot \begin{pmatrix} U_{dc} \\ U_{qc} \end{pmatrix} \tag{5.26}$$

The current components in the dc-qc coordinate system can be measured directly because the angle of the dc-axis is always known. Therefore it is not necessary to design a full order observer for all the four state variables. The observer only need to estimate the back-EMF components e_{dc} and e_{qc} so that the angle error $\Delta\theta$ can be

calculated. Accordingly, a reduced order observer is designed. The following definitions are made for the observer design:

$$\vec{x}_i = \begin{pmatrix} i_{dc} \\ i_{qc} \end{pmatrix}, \qquad \vec{x}_e = \begin{pmatrix} e_{dc} \\ e_{qc} \end{pmatrix}, \qquad \vec{U} = \begin{pmatrix} U_{dc} \\ U_{qc} \end{pmatrix}$$

$$A_{11} = \begin{pmatrix} -\dfrac{R}{L} & \omega_1 \\ -\omega_1 & -\dfrac{R}{L} \end{pmatrix}, \quad A_{12} = \begin{pmatrix} -\dfrac{1}{L} & 0 \\ 0 & -\dfrac{1}{L} \end{pmatrix}, \quad A_{21} = A_{22} = \begin{pmatrix} 0 & 0 \\ 0 & 0 \end{pmatrix}$$

$$B_1 = \begin{pmatrix} \dfrac{1}{L} & 0 \\ 0 & \dfrac{1}{L} \end{pmatrix}, \qquad B_2 = \begin{pmatrix} 0 & 0 \\ 0 & 0 \end{pmatrix}$$

The system equation 5.26 can be rewritten as:

$$\begin{aligned} \dot{\vec{x}}_i &= A_{11}\vec{x}_i + A_{12}\vec{x}_e + B_1\vec{U} \\ \dot{\vec{x}}_e &= A_{21}\vec{x}_i + A_{22}\vec{x}_e + B_2\vec{U} \end{aligned} \tag{5.27}$$

The current components in the dc-qc coordinate system are considered as the system output:

$$\vec{y} = \vec{x}_i$$

The reduced order observer is basically adding a correction term to the second equation of equation 5.27:

$$\dot{\hat{\vec{x}}}_e = A_{22}\hat{\vec{x}}_e + A_{21}y + B_2\vec{U} + H\left(\vec{x}_e - \hat{\vec{x}}_e\right) \tag{5.28}$$

The cap sign stands for estimated value; and H is the amplification matrix of the correction, which is still to be defined. To get rid of the unknown $\vec{x}_e$, the first equation of equation 5.27 is inserted in equation 5.28. And because A_{21}, A_{22}, B_2 are zero matrixes and A_{12}^{-1} obviously exists by its definition, this results in:

$$\dot{\hat{\vec{x}}}_e = H\left(A_{12}^{-1}(\dot{\vec{y}} - A_{11}\vec{y} - B_1\vec{U}) - \hat{\vec{x}}_e\right) \tag{5.29}$$

By defining a new state vector $V = \hat{\bar{x}}_e - HA_{12}^{-1}\bar{y}$, the equation 5.29 can be reformed as:

$$\dot{V} = -H \cdot V + (-HHA_{12}^{-1} - HA_{12}^{-1}A_{11})\bar{y} - HA_{12}^{-1}B_1\bar{U} \qquad (5.30)$$

By updating the new state vector V in the equation 5.30 with the current measurement $\bar{y}$ and the voltage vector $\bar{U}$, the back-EMF vector in the dc-qc coordinate system can be calculated by:

$$\hat{\bar{x}}_e = \begin{pmatrix} e_{dc} \\ e_{qc} \end{pmatrix} = V + HA_{12}^{-1}\bar{y} \qquad (5.31)$$

To define the amplification matrix H, the estimation error $\varepsilon = \bar{x}_e - \hat{\bar{x}}_e$ should be considered. By subtracting equation 5.28 from the second equation of 5.27, the error dynamic equation can be obtained:

$$\dot{\bar{\varepsilon}} = -H \cdot \bar{\varepsilon} \qquad (5.32)$$

To eliminate the estimation error $\bar{\varepsilon}$, H should be a positive definite matrix. For simplicity, H is defined as a diagonal matrix with positive diagonal elements $\lambda_{1,2}$:

$$H = \begin{pmatrix} \lambda_1 & 0 \\ 0 & \lambda_2 \end{pmatrix} \qquad (5.33)$$

Mathematically, the bigger the diagonal elements $\lambda_{1,2}$ are, the faster the estimation error will converge to zero. In the practice however, $\lambda_{1,2}$ can not be infinitively large. If their values are too big, the observer will be very sensitive to the high frequency measurement noise, which could lead to instability of the observer. Therefore, the choice of these values is a compromise between fast convergence (big $\lambda_{1,2}$) and stability (limited $\lambda_{1,2}$).

5.2.2.4 Back-EMF Estimation in α-β Coordinate with Observer

This category of methods estimated the back-EMF vector in the α-β coordinate system. The back-EMF vector in the α-β coordinate system is defined as

$$\begin{pmatrix} e_\alpha \\ e_\beta \end{pmatrix} = \begin{pmatrix} -\omega_r \Psi_{pm} \sin\theta_d \\ \omega_r \Psi_{pm} \cos\theta_d \end{pmatrix}$$

Assuming again that the rotor speed change is much slower than the current change, and the estimated rotor speed approximately coincides with the real rotor speed; the following system equation can be established basing on equation 3.5:

$$\begin{pmatrix} \dot{i}_\alpha \\ \dot{i}_\beta \\ \dot{e}_\alpha \\ \dot{e}_\beta \end{pmatrix} = \begin{pmatrix} -\dfrac{R}{L} & 0 & -\dfrac{1}{L} & 0 \\ 0 & -\dfrac{R}{L} & 0 & -\dfrac{1}{L} \\ 0 & 0 & 0 & -\omega_1 \\ 0 & 0 & \omega_1 & 0 \end{pmatrix} \cdot \begin{pmatrix} i_\alpha \\ i_\beta \\ e_\alpha \\ e_\beta \end{pmatrix} + \begin{pmatrix} \dfrac{1}{L} & 0 \\ 0 & \dfrac{1}{L} \\ 0 & 0 \\ 0 & 0 \end{pmatrix} \cdot \begin{pmatrix} U_\alpha \\ U_\beta \end{pmatrix} \qquad (5.34)$$

Since the current components in the stator-fixed α-β coordinate system are directly measurable, it is again not necessary to design a full order observer. Similar as the estimation in the dc-qc coordinate system, a reduced order observer is designed, which only estimates the back-EMF components e_α and e_β. And the rotor angle is calculated from this back-EMF estimate. Due to the similarity, the derivation of the reduced order observer is omitted here. With the following matrix definitions

$$\bar{x}_i = \begin{pmatrix} i_\alpha \\ i_\beta \end{pmatrix}, \quad \bar{x}_e = \begin{pmatrix} e_\alpha \\ e_\beta \end{pmatrix}, \quad \bar{U} = \begin{pmatrix} U_\alpha \\ U_\beta \end{pmatrix}, \quad \bar{y} = \bar{x}_i$$

$$A_{11} = \begin{pmatrix} -\dfrac{R}{L} & 0 \\ 0 & -\dfrac{R}{L} \end{pmatrix}, \quad A_{12} = \begin{pmatrix} -\dfrac{1}{L} & 0 \\ 0 & -\dfrac{1}{L} \end{pmatrix}, \quad A_{21} = \begin{pmatrix} 0 & 0 \\ 0 & 0 \end{pmatrix} \quad A_{22} = \begin{pmatrix} 0 & -\omega_1 \\ \omega_1 & 0 \end{pmatrix}$$

$$B_1 = \begin{pmatrix} \dfrac{1}{L} & 0 \\ 0 & \dfrac{1}{L} \end{pmatrix}, \quad B_2 = \begin{pmatrix} 0 & 0 \\ 0 & 0 \end{pmatrix}$$

$$V = \hat{\bar{x}}_e - HA_{12}^{-1}\bar{y}$$

The reduced order observer is defined as:

$$\dot{V} = (A_{22} - H) \cdot V + [(A_{22} - H)HA_{12}^{-1} - HA_{12}^{-1}A_{11}]\bar{y} - HA_{12}^{-1}B_1\bar{U}$$

$$(5.35)$$

And the back-EMF e_α and e_β are calculated by:

$$\hat{\vec{x}}_e = \begin{pmatrix} e_\alpha \\ e_\beta \end{pmatrix} = V + HA_{12}^{-1} \vec{y}$$

The definition of the correction gain matrix H is a little different than the estimation in the dc-qc coordinate system. Without derivation, the estimation error $\vec{\varepsilon} = \hat{\vec{x}}_e - \vec{x}_e$ fulfills the dynamic equation 5.36:

$$\dot{\vec{\varepsilon}} = \underbrace{(A_{22} - H)}_{K} \cdot \vec{\varepsilon} \tag{5.36}$$

Let:

$$H = \begin{pmatrix} h_{11} & h_{12} \\ h_{21} & h_{22} \end{pmatrix}$$

Then the dynamic matrix K for the error equation is:

$$K = \begin{pmatrix} -h_{11} & -\omega_1 - h_{12} \\ \omega_1 - h_{21} & -h_{22} \end{pmatrix}$$

Since the estimated rotor speed ω_1 is known, a sufficient condition to make K negative definite is:

$$h_{12} = -\omega_1$$
$$h_{21} = \omega_1$$
$$h_{11}, h_{22} > 0$$

The tuning of the parameters h_{11}, h_{22} is again a compromise between fast convergence (big h_{11}, h_{22}) and stability (limited h_{11}, h_{22}).

5.2.2.5 The Simulation Results of Back-EMF Based Rotor Angle Estimation and Summary

The simulation results of the back-EMF based angle estimation methods introduced in this section are presented here. The simulation provides a comparison among the different Back-EMF-based rotor angle estimation methods. Parameters of the methods can also be tuned offline before the fine tuning on the test bench.

The method of Sakamoto [25] is abbreviated as the PLL method after the name of the estimation control structure used in this method. Two rotor rotation profiles have been chosen: the sinusoidal rotation and the ABS operation. The ABS operation is the rotor motion measured during an ABS-braking operation. The ABS operation is a typical operation in which highly dynamic rotor speed variation is present. During the simulation, noise signal was injected in the current signal measurement. An offset error (-0.3 A-0.3 A) and Gauss noise with zero mean and a variance of 0.2 A were added to each of the three phase current signals. This noise injection resembles the real measurement condition on the test bench. Since all the back-EMF methods are not applicable for zero rotor speed, the estimation was switched off under the mechanical rotor speed of 100 rpm.

The parameter of the EKF method had been tuned according to the recommendation summarized in [32]. The initial covariance matrix P_0 was set to a zero matrix because the initial condition of the state vector is known. The covariance matrix Q and R are set on try-and-error base. Both are set as diagonal matrix according to [32]. Since the noise is injected in the current measurement and the process equation is rather accurate, it is reasonable to set the diagonal elements of R bigger than Q. Although the Jacobian matrixes H_k, W_k, V_k are constant matrixes with the system model chosen (equation 5.21), the matrix multiplication and inversions involved in the EKF method cause higher computation effort compared to the other back-EMF based estimation methods. It should be noted also that the estimated rotor angle is a parameter in the prediction step (the dynamic matrix A).

The figure 5.14 presents the simulation results of the sinusoidal operation and the figure 5.15 shows the results of the ABS operation. The first subplot of each figure illustrates the electrical rotor angle and the estimated angles. The dash line shows the switch signal. The estimation is active if the switch signal is 'high'. Due to the small estimation error, it is difficult to compare the performance with this plot. Therefore,

the estimation errors of each of the four methods are shown in the following sub-plots. In figure 5.15, it can be seen that the observer methods in the dc-qc or the α-β coordinate systems provide similar and the smallest estimation error both in the sinus and the ABS operations. The EKF method also produces satisfying result. But due to the complexity of the method, it will not be further considered in the solution. The PLL method has the biggest estimation error due to the ignorance of the current derivative.
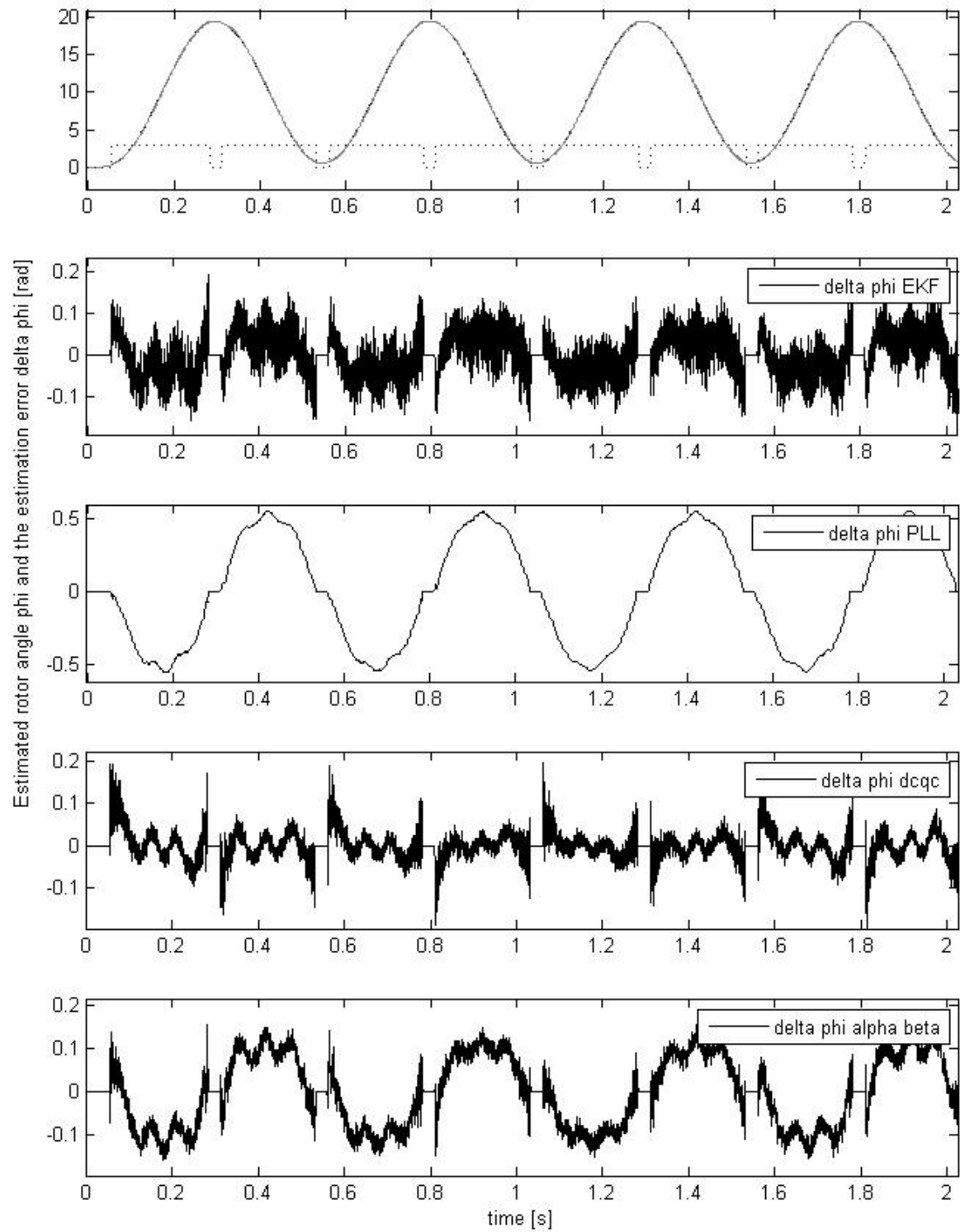
Figure 5.14: the simulation results of the back-EMF based angle estimation in sinus operation.
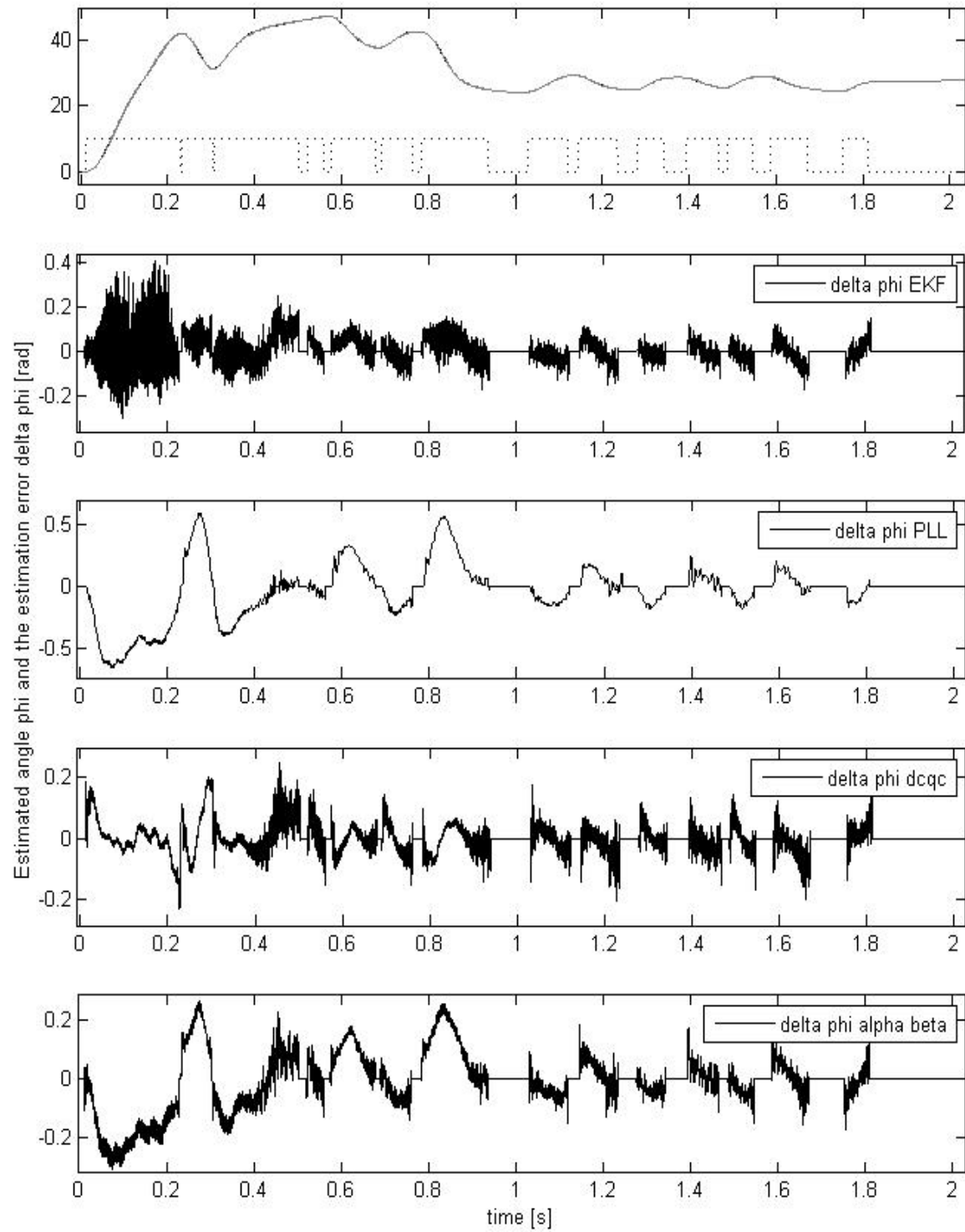
Figure 5.15: the simulation results of the back-EMF based angle estimation in the ABS operation.

5.3 Active Rotor Angle Estimation Methods

For angle estimation at very low (several Hz) and zero rotor speed, the back-EMF is too weak. Therefore it is not possible to estimate the back-EMF stably with observer. The rotor angle can not be estimated with EKF-based methods either, because the system is not observable at zero speed [40]. In this speed range, active estimation method utilizing secondary physical effects is a popular field of research [41-48]. These effects are called secondary because they are normally insufficiently or not at all modeled by the fundamental frequency motor model, e.g. equation 3.3 or 3.5. Typical examples of such effects are the anisotropy of magnetic saturation of the iron; the anisotropy of the leakage inductance; effects of stator yokes; rotor eccentricity etc. While the leakage inductance anisotropy is frequently discussed in the publication about the sensorless control of asynchronous motor (ASM) [45][46], the anisotropy of magnetic saturation seems to be the only applicable secondary effect for SM-PMSM at the moment [41-44][47]. The anisotropy of magnetic saturation introduces a rotor position dependency of the inductance. An explanation of the magnetic saturation anisotropy in a SM-PMSM is presented in subsection 5.3.1.
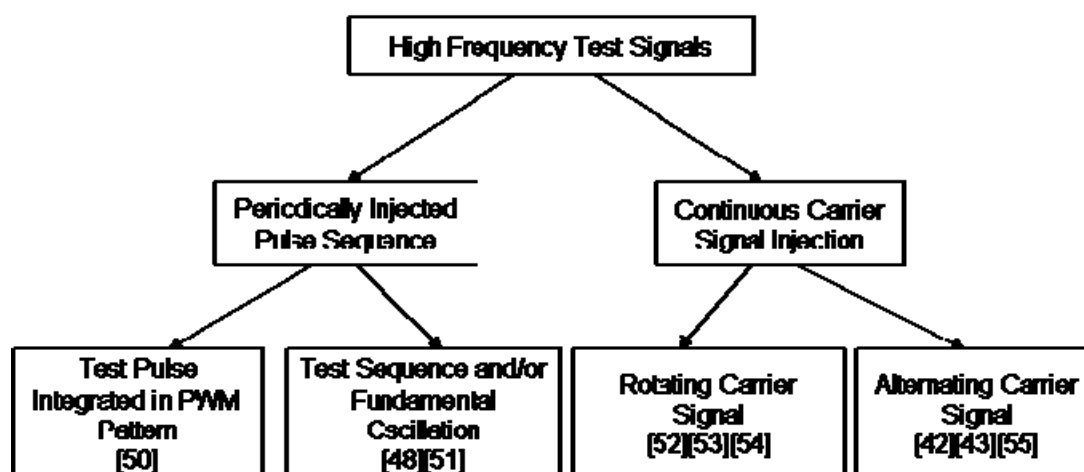
Figure 5.16: an overview of the existing high frequency injection methods [49].

To utilize the secondary physical effects for the purpose of rotor angle estimation, methods with high frequency test signal injection have become more and more popular [42-43][52-55]. In these methods high frequency voltage/current test signals are injected and superposed on the control current/voltage signals. And because the control signals have the fundamental frequency which is much lower than the injected test signal, it is possible to extract the current/voltage response to the high frequency

test signal with proper filtering and modulation. Normally the transient behavior of the current/voltage response are observed and analyzed to determine the rotor position. An overview on the test signals published so far is provided in [49] and is illustrated in figure 5.16:

The high frequency test signals can be categorized into two groups [49] as shown in figure 5.16: the periodically injected pulse sequence and the continuously injected carrier test signals. Typical examples of these methods will be introduced in subsection 5.3.2 and 5.3.3.

Recently a new type of injection signal is introduced in [44]. The injected test signal has a very high frequency of 100-500 kHz[5]. However, this kind of oscillation signal can not be generated by conventional power converters that normally work at a frequency of 20 kHz or less. Extra hardware is therefore needed for the high frequency test signal generation which makes this method not practical for commercial use.

Basically, one can inject the high frequency test signal as voltage or as current. However, the injection of current test signal is constrained by the dynamic of the current control. In comparison to that, voltage test signal can be injected by simply manipulating the PWM pattern. The voltage injection is therefore preferred.

5.3.1 The Anisotropy of Magnetic Saturation in SM-PMSM

In an SM-PMSM, there are two sources of magnetic flux: the flux of the permanent magnet on the rotor; and the magnetic flux of the winding current. In the following discussion of the magnetic flux of winding current, the term *current vector* refers to the vectorial sum of the three phase current vectors (U-V-W); as usually adopted in the field-oriented control theory. Since each phase current vector has an amplitude proportional to the magnetic motive force (mmf) it produces and has the same direction as its mmf; the overall mmf produced by the three phase current vectors should also be proportional to the amplitude of the current vector sum and has the same direction as the current vector. The relation between flux and current is described by $\Psi = L \cdot I$. Since L is changing with respect to the mmf as schematically shown in figure 5.17, the flux generated by the current vector is not linearly proportional to the current vector. And especially if the iron is strongly saturated, the inductance L decreases rapidly and tends to the value of the air inductance. This means the magnet flux increases only very little when the mmf further rises.

---

[5] The injection signals of the other methods have typically the frequency in the range of 0.5 kHz-3 kHz.

The permanent magnet flux has an approximately sinusoidal amplitude distribution along the rotor circumference in our SM-PMSM. Due to the permanent magnet flux, the iron is also slightly saturated in a sinusoidal manner along the stator circumference under current-free condition. And the distribution of the iron saturation due to permanent magnet should be synchronous to the orientation of the permanent magnet flux (d-axis), i.e. rotor synchronous. The flux distribution of the permanent magnet of a very similar SM-PMSM is shown in figure 5.18. The figure is taken from [56], in which the author presented the FEM simulation results of the flux distribution in a SM-PMSM with 4 poles.
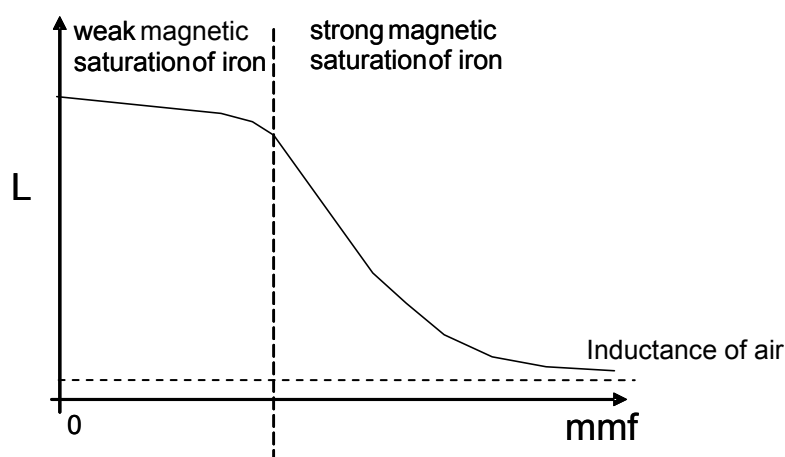
Figure 5.17: schematic illustration of the relation between inductance and flux.
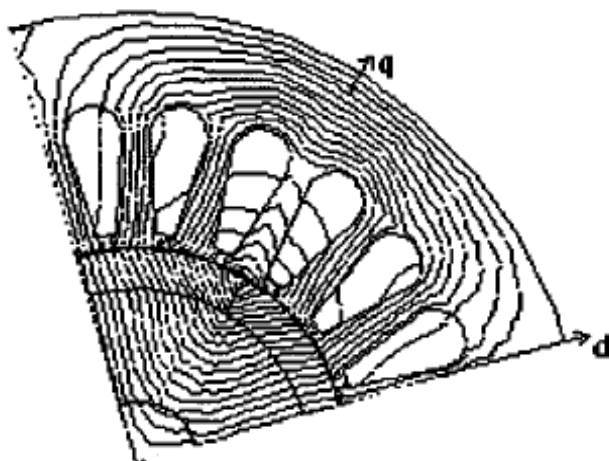
Figure 5.18: the distribution of the permanent magnet flux (current-free). [56]
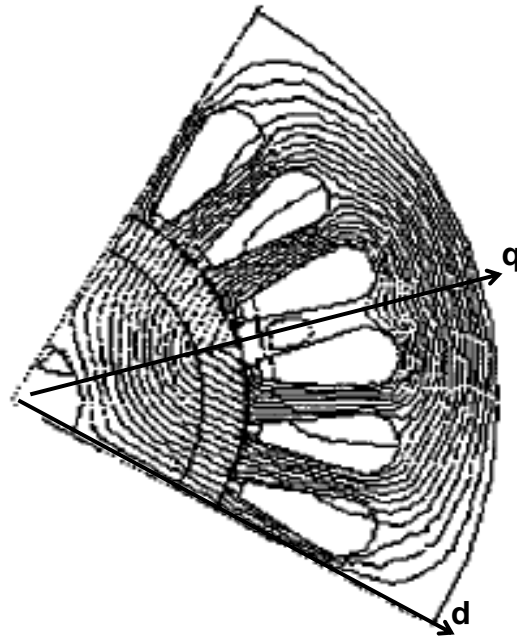
Figure 5.19: the distribution of the permanent magnet flux and the imposed flux in d-direction (Id>0, Iq=0). [56]

In figure 5.18, the flux density in the d-direction is significantly stronger than in the q-direction. Although due to the radial symmetric construction of SM-PMSM, the inductance should be almost the same in any radial direction, the sinusoidal distribution of the mmf of the permanent magnet however can result in slight difference in the inductance in different radial directions. And if an mmf is produced by the winding current in the positive d-direction (the direction of the permanent magnet flux), the strongest local saturation can be produced, i.e. the biggest inductance drop can be observed in this case. This is shown in figure 5.19 [56].

In field oriented control, the current vector is generated in the *q-direction* to achieve the maximal motor torque and the minimal power lost. Let's call this the control current vector; and the current vector for rotor position estimation will be referred to as the test current vector. The control current vector produces an mmf in the q-direction. If the control current vector I_q is strong enough, which is the case in operation with heavy load, the anisotropy of the iron saturation or inductance anisotropy will be 'blurred' (figure 5.20).
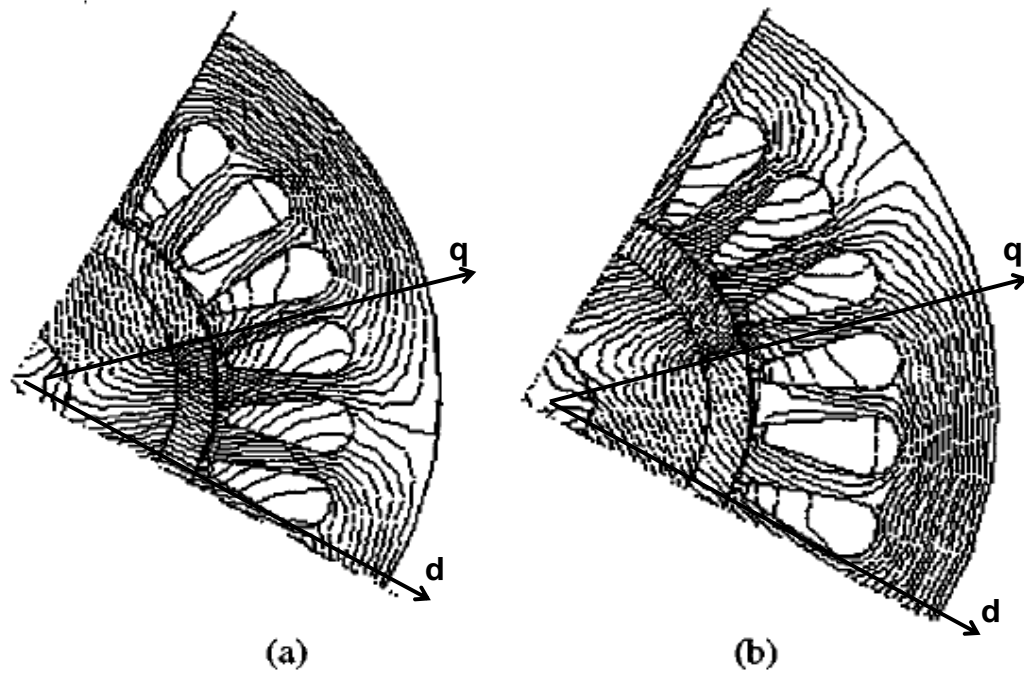
Figure 5.20: flux distribution in the iron with large Iq. [56]. The flux density is high both in d- and q-direction. (a) positive Iq; (b) negative Iq.

5.3.2 Pulse Sequence Test Signal Injection

The pulse sequence test signal is a sequence of voltage pulses with the same amplitude and duration that are injected in different directions along the stator circumference. By analyzing the current responses of these voltage pulses, the inductance anisotropy is detected and the orientation of the d-axis can be determined. Typical rotor position estimation methods using pulse sequence can be found in [47, 57, 58]. Such methods can be considered as a kind of open-loop 'measurement' of the inductance anisotropy. To have a better understanding of these methods, an analytical explanation is provided here. The definition of the coordinate systems shown in figure A.1 is modified a little. Namely, the estimated coordinate system is denoted as the x-y coordinate instead of dc-qc coordinate to avoid confusion with the discussion on the angle estimation at high and medium rotor speed. The new definition of coordinate system is shown in figure 5.21. All angles mentioned in the following discussion are electrical angles so that the number of pole pairs will not show up in the equations.
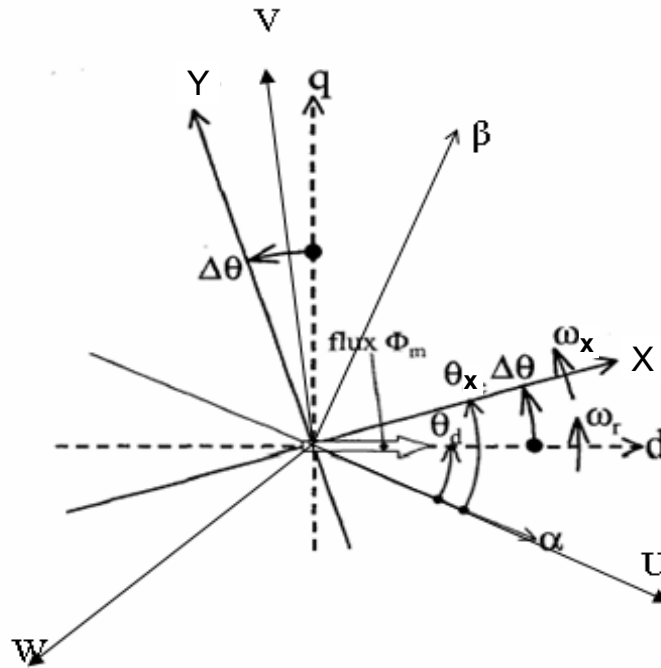
Figure 5.21: the new definition of the coordinate systems. The dc-qc coordinate in figure A.1 is renamed as the x-y coordinate to avoid confusion.

The fundamental frequency model of SM-PMSM in α-β coordinate system is described by equation 3.5. If the equation is transformed into the vector form, it becomes:

$$\vec{U}_{\alpha\beta} = D_1 \cdot \dot{\vec{I}}_{\alpha\beta} + D_2 \cdot \vec{I}_{\alpha\beta} + \vec{K}_{e,\alpha\beta} \tag{5.37}$$

$$\vec{U}_{\alpha\beta} = \begin{pmatrix} U_\alpha \\ U_\beta \end{pmatrix}, \qquad \vec{I}_{\alpha\beta} = \begin{pmatrix} I_\alpha \\ I_\beta \end{pmatrix}, \qquad \dot{\vec{I}}_{\alpha\beta} = \begin{pmatrix} \dot{I}_\alpha \\ \dot{I}_\beta \end{pmatrix}$$

$$D_1 = \begin{bmatrix} L_0 + \Delta L \cos 2\theta_d & \Delta L \sin 2\theta_d \\ \Delta L \sin 2\theta_d & L_0 - \Delta L \cos 2\theta_d \end{bmatrix}, \qquad L_0 = \frac{L_d + L_q}{2}, \; \Delta L = \frac{L_d - L_q}{2}$$

$$D_2 = \begin{bmatrix} R - \omega_r L_d \sin 2\theta_d & -\omega_r (L_d + L_q \cos 2\theta_d) \\ \omega_r (L_d \cos 2\theta_d + L_q) & R - \omega_r L_q \sin 2\theta_d \end{bmatrix}$$

The back-EMF is: $\vec{K}_{e,\alpha\beta} = \omega_r \Psi_{pm} \begin{pmatrix} -\sin\theta_d \\ \cos\theta_d \end{pmatrix}$

At very low and zero rotor speed, i.e. $\omega_r \approx 0$, the back-EMF term $\vec{K}_{e,\alpha\beta}$ can be ignored and the matrix D_2 can be approximated as:

$$D_2 \approx \begin{bmatrix} R & 0 \\ 0 & R \end{bmatrix} \tag{5.38}$$

And because the current derivative term is dominant at voltage jumps of the injected voltage pulses, the current-voltage relation can be further approximated by:

$$\vec{U}_{\alpha\beta} \approx D_1 \cdot \dot{\vec{I}}_{\alpha\beta} \tag{5.39}$$

If the α-axis is defined as the real axis and the β-axis is defined as the imaginary axis the equations can also be written in complex form. Now suppose the voltage vector $\vec{U}_{\alpha\beta}$ lies in the positive X-direction, and define:

$$U_s = U_\alpha + jU_\beta = |U_s| \cdot e^{j\theta_X}$$
$$\dot{I}_s = \dot{I}_\alpha + j\dot{I}_\beta = |\dot{I}_s| \cdot e^{j\theta_X} \tag{5.40}$$

With the definition 5.40, equation 5.39 can be transformed into:

$$U_s \approx L_0 \cdot \dot{I}_s + \Delta L \cdot e^{j2\theta_d} \cdot \dot{I}_s^* \tag{5.41}$$

Also with the definition 5.40 and equation 5.41, the following relation can be obtained:

$$z = \frac{|U_s|}{|\dot{I}_s|} \approx L_0 + \Delta L \cdot e^{j(2\theta_d - 2\theta_X)} \tag{5.42}$$

$$\begin{aligned}y = z^{-1} &\approx k \cdot (L_0 + \Delta L \cos 2\Delta\theta) + j \cdot k \cdot \Delta L \sin 2\Delta\theta \\ &= k \cdot L_0 + k \cdot \Delta L \cdot e^{j2\Delta\theta}\end{aligned} \tag{5.43}$$

$$k = \frac{1}{(L_0 + \Delta L \cos 2\Delta\theta)^2 + \Delta L^2 \sin^2 2\Delta\theta}$$

For very short duration of voltage pulse, equation 5.42 can be approximated by:

$$|U_s| = z \cdot \frac{\Delta |I_s|}{\Delta t} \quad \Rightarrow \quad \Delta |I_s| = y \cdot |U_s| \cdot \Delta t \tag{5.44}$$

In the INFORM method introduced in [47], z is called the INFORM reactance, and y is the inverse INFORM reactance. Since the amplitude $|U_s|$ and the duration Δt of the test voltage pulse are known and constant; and the injection angle θ_X is also known; by injecting the voltage pulse in different directions and measuring the amplitude change $\Delta |I_s|$ of the current vectors in the corresponding directions, the rotor position contained in y can be explicitly solved. In the INFORM method [47], the inverse INFORM reactance y is formulated as:

$$\begin{aligned}\text{Re}\{y\} &= y_0 - \Delta y \cdot \cos 2\Delta\theta \\ \text{Im}\{y\} &= -\Delta y \cdot \sin 2\Delta\theta\end{aligned} \tag{5.45}$$

Comparing equation 5.45 and equation 5.43, we can obtain the analytical expression of y_0 and Δy:

$$\begin{aligned}y_0 = k \cdot L_0 &= \frac{L_0}{(L_0 + \Delta L \cos 2\Delta\theta)^2 + \Delta L^2 \sin^2 2\Delta\theta} \\ \Delta y = -k \cdot \Delta L &= \frac{-\Delta L}{(L_0 + \Delta L \cos 2\Delta\theta)^2 + \Delta L^2 \sin^2 2\Delta\theta}\end{aligned} \tag{5.46}$$

From equation 5.46, it can be seen that y_0 and Δy are variables depending on the difference $\Delta\theta$ between the injection angle of the voltage pulse and the d-axis. This

is not only because their expressions contain the term $\Delta\theta$, but also because the inductance terms L_0 and ΔL depend on the distribution (d-axis synchronous) of the iron saturation, which changes also according to $\Delta\theta$. In the INFORM method [47], however, y_0 and Δy are assumed to be invariant with respect to $\Delta\theta$, this leads to position estimation error. In [47], it had also been observed that y_0 and Δy are fluctuating significantly around the assumed circle. For better estimation of $\Delta\theta$, a big Δy is preferred, i.e. a big ΔL is advantageous. This makes the attempt reasonable to inject very strong voltage pulse to amplify the inductance anisotropy, as was done in [47]. But strong voltage pulse also introduces strong motor torque pulse if the voltage pulse is not aligned to the d-axis and thus disturbs the motor control. This is a common drawback of methods using pulse sequence test signal.

In [58], a more straight forward approach was proposed. As introduced in subsection 5.3.1, due to the sinusoidal mmf distribution of the permanent magnet, the stator iron is saturated differently along the stator circumference. The permanent magnet flux density reaches its maximum in the d-axis. If the injected voltage pulse is aligned to the positive d-axis, strong local saturation can be expected, which in turn results in a significant drop of L_d, i.e. drop of the amplitude of the reactance z in equation 5.42. Considering equation 5.44, if voltage pulses with the same amplitude and duration are injected successively in different radial directions, the maximal current change $\Delta|I_s|$ should be observed when the voltage pulse is nearly aligned to the positive d-axis. By this means, the orientation of the d-axis can be found out and thus the rotor angle. An alternative of this method is to send voltage pulses pair successively in different directions and the voltage pulses pair always have the opposite direction. The d-axis is then characterized by the biggest $\Delta|I_s|_{U+} - \Delta|I_s|_{U-}$. Inspire of its simplicity, such methods need to inject noticeably more voltage pulses to achieve a good estimation resolution and produce hence even more motor torque pulses. And the implementation of such methods requires very precise synchronization between voltage pulse injection and current measurement.

5.3.3 High Frequency Continuous Test Signal Injection

The methods basing on continuous test signal inject either a rotating test voltage vector (revolving carrier injection); or a sinusoidal test voltage in the estimated d-axis (alternating carrier injection). Typical examples of such methods can be found in [42][49]. In contrast to the pulse-sequence-based methods introduced in section

5.3.2, these methods do *not* require strong magnetic saturation in the iron. The amplitude of the injected high frequency voltage is very small compared to the motor control voltage. The frequency of the test signal lies typically between 0.5 kHz to 3 kHz, which is much higher than the fundamental frequency (rotor rotation frequency). These methods utilize the tiny inductance anisotropy caused by the anisotropy of the permanent magnet flux without triggering strong magnetic saturation with winding current. Since the distribution of the permanent magnet flux is assumed to be sinusoidal, the flux in d-direction should be stronger than the flux in q-direction (ideally zero flux). This results in a slightly bigger inductance in the q-direction (L_q) than in the d-direction (L_d) under current-free condition. The *high-frequency current response* of the injected test voltage is extracted from the current measurement with a band-pass filter, which rejects the fundamental frequency component. The high-frequency current response is then processed with proper modulation and demodulation and band-pass filtering so that a quantity, which is proportional to the angle estimation error, is generated. And this quantity is used to correct the angle estimation in a closed-loop tracking observer. Since this quantity for estimation correction is normally proportional to the tiny inductance difference in the d- and q-directions, it is not a wonder that such methods suffer a poor signal-to-noise ratio. Large motor moment also worsens the estimation precision because the flux of the moment-producing current vector (I_q) blurs the flux anisotropy of the permanent magnet.

5.3.3.1 The Continuous Test Signals

As shown in figure 5.16, there are basically two types of continuous test signals: the *revolving carrier injection* and the *alternating carrier injection*.

The revolving carrier injection injects a rotating test voltage vector. The injected voltage test signal can be formulated in complex form as the following:

$$u_c^{(S)} = u_c \cdot e^{j\omega_c t} \tag{5.47}$$

The complex value $u_c^{(S)}$ represents the test voltage vector in the stator-fixed α-β coordinate (figure 5.21). In this representation, the stator-fixed α-β coordinate system is considered as the complex plane, in which the α-axis corresponds to the real axis and the β-axis corresponds to the imaginary axis. u_c is a constant scalar, which can be quite small in amplitude, since strong iron saturation is not required. ω_c is the con-

stant injection frequency, which lies typically between $2\pi \times 0.5$ kHz to $2\pi \times 3$ kHz. The superscript S stands for stator-fixed and the subscript c stands for carrier signal.

The alternating carrier injection method is characterized by injecting a sinusoidal voltage only in the *estimated d-direction*. The injection voltage is described in complex form as:

$$u_c^{(S)} = u_c \cdot \cos(\omega_c t) \cdot e^{j\theta_X} \tag{5.48}$$

Where θ_X is the estimated angle of the d-axis (figure 5.21).
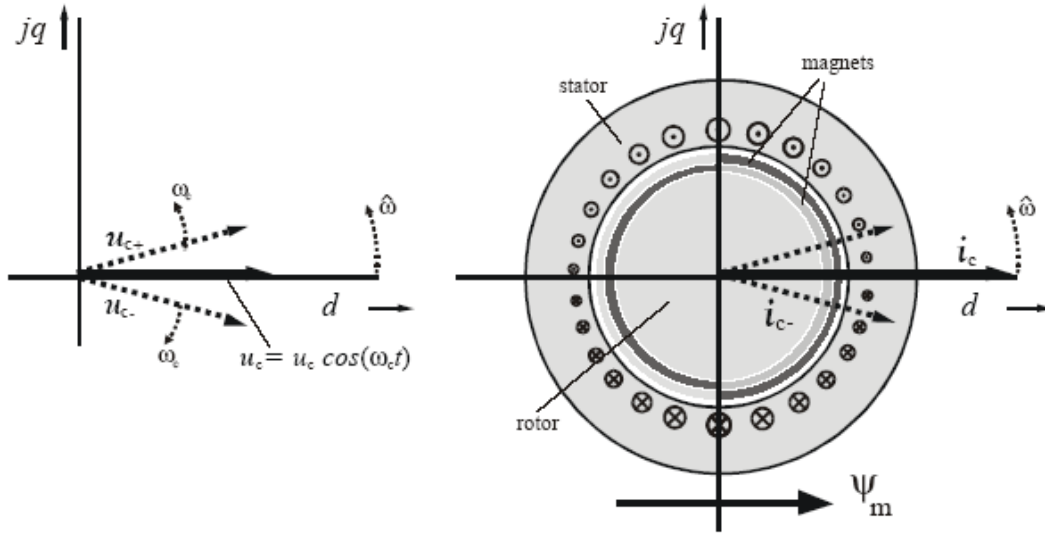
Figure 5.22: the alternating carrier injection. $\hat{\omega}$ is the estimated rotor speed.

The revolving carrier injection has the same problem as the pulse sequence injection discussed in section 5.3.2, i.e. it produces motor moment fluctuation; while the alternating carrier injection has no influence on the motor moment if the angle estimation is correct. According to the Euler's formula:

$$\cos(\omega_c t) = \frac{e^{j\omega_c t} + e^{-j\omega_c t}}{2} \tag{5.49}$$

the alternating carrier injection can also be considered as injecting a positive as well as a negative revolving voltage vector symmetrically with respect to the estimated d-axis at the same time (figure 5.22). The estimations with the positive revolving voltage vector and with the negative revolving voltage vector provide redundant estimation and can hence be used to compensate noise. Therefore, the alternating carrier in-

jection shows better performance in general compared to the revolving carrier injection.

5.3.3.2 The Estimation Method of M. Linke with Alternating Carrier Injection

The estimation scheme proposed by M. Linke in his dissertation [49] is illustrated in figure 5.23. A high-frequency voltage signal is injected in the *estimated* d-axis (X-axis in figure 5.21). The test voltage is expressed in complex form as:

$$u_c^{(S)} = u_c \cos(\omega_c t) \cdot e^{j\theta_X} \tag{5.50}$$

Without citing the derivation, the resulting high-frequency current response in complex form (α-β coordinate) can be written as:

$$i_c^{(S)} = \frac{u_c}{j4\omega_c L_d L_q} \left\{ \begin{array}{c} \underbrace{\left[(L_d + L_q)e^{j\theta_X} + (L_q - L_d)e^{-j(\theta_X - 2\theta_d)}\right] \cdot e^{j\omega_c t}}_{\text{Positive sequence component}} \\[2em] \underbrace{-\left[(L_d + L_q)e^{j\theta_X} + (L_q - L_d)e^{-j(\theta_X - 2\theta_d)}\right] \cdot e^{-j\omega_c t}}_{\text{Negative sequence component}} \end{array} \right. \tag{5.51}$$

The expression can be briefed as: $i_c^{(S)} = i_p^{(S)} + i_n^{(S)}$; where $i_p^{(S)}$ stands for the positive sequence component with factor, and $i_n^{(S)}$ stands for the negative sequence component with factor. It should be noted that the measured current consists of not only this high-frequency current response to the test voltage but also the fundamental frequency current response to the control voltage. The normalized amplitude spectrum of the measured current vector $I^{(S)}$ obtained from a test bench experiment is shown in figure 5.24.
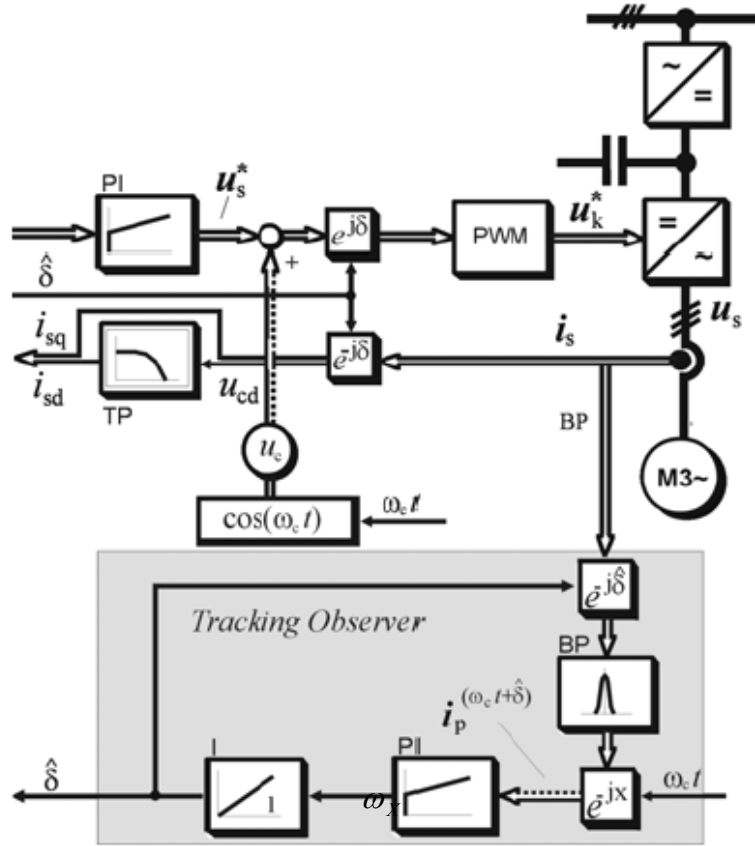
Figure 5.23: the angle estimation proposed in [49]. This is the original diagram published in [49], in which $\delta = \theta_d, \hat{\delta} = \theta_X$.
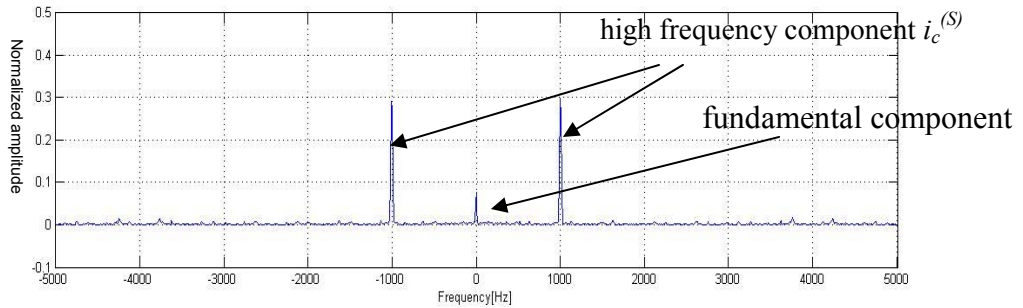

Figure 5.24: the normalized amplitude spectrum of the measured current vector $I^{(S)}$ (complex). The measurement is taken from a test bench experiment in which the motor position was controlled to follow a sinusoidal curve and the loading moment was zero. The sampling frequency was 10 kHz and the frequency of the injected test voltage is $\omega_c = 2\pi \times 1$ kHz.

The fundamental component as well as the high frequency positive and negative sequence components of the current response can be seen clearly in figure 5.24. The fundamental component is quite weak because the experiment was done under load-free condition.
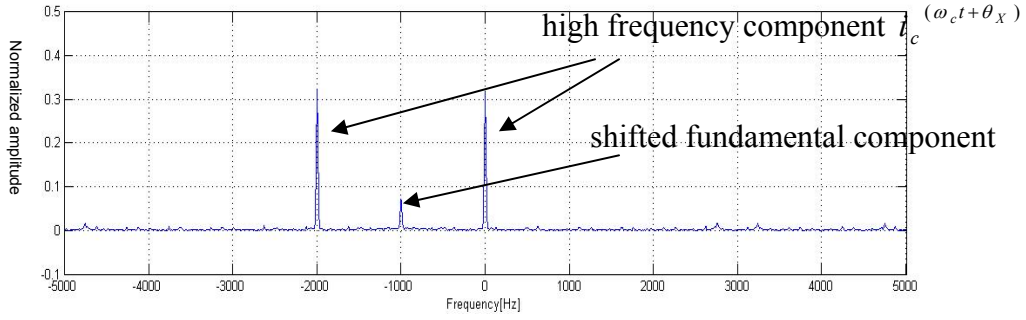
Figure 5.25: the normalized amplitude spectrum of the measured current after the modulation (normalized amplitude spectrum of $I^{(\omega_c t + \theta_X)}$).

As mentioned before, one can extract the angle estimation error either from the positive sequence component or the negative sequence component form the high frequency current response. The procedure to calculate the estimation error from the positive sequence component is shown. For this purpose, the measured current vector $I^{(S)}$ is first modulated as follow:

$$I^{(\omega_c t + \theta_X)} = I^{(S)} \cdot e^{-j(\omega_c t + \theta_X)} \tag{5.52}$$

This modulation can be interpreted as 'shifting' the spectrum of the current measurement $I^{(S)}$ in the negative frequency direction (compare figure 5.24 and figure 5.25).

With this modulation, the high-frequency current response $i_c^{(S)}$ contained in $I^{(S)}$ under goes the same modulation:

$$i_c^{(\omega_c t + \theta_X)} = i_c^{(S)} \cdot e^{-j(\omega_c t + \theta_X)} \tag{5.53}$$

The resulting expression of $i_c^{(\omega_c t + \theta_X)}$ is:

$$i_c^{(\omega_c t + \theta_X)} = \frac{u_c}{j4\omega_c L_d L_q} \left\{ \begin{bmatrix} (L_d + L_q) + (L_q - L_d)e^{-j2(\theta_X - \theta_d)} \end{bmatrix} \\ - \begin{bmatrix} (L_d + L_q) + (L_q - L_d)e^{-j2(\theta_X - \theta_d)} \end{bmatrix} \cdot e^{-j2\omega_c t} \right\} \tag{5.54}$$

The positive sequence component is shifted to around zero frequency and the negative sequence component is shifted to $-2\omega_c$. The positive sequence component can now be extracted by low-pass filtering of the modulated current measurement

$I^{(\omega_c t+\theta_X)}$ around zero frequency. This low-pass filtering also rejects the fundamental frequency component from $I^{(\omega_c t+\theta_X)}$. The extracted positive sequence component is described by:

$$
\begin{aligned}
i_p^{(\omega_c t+\theta_X)} &= \frac{u_c}{j4\omega_c L_d L_q}\left[(L_d+L_q)+(L_q-L_d)\cdot e^{-j2\Delta\theta}\right] \\
&= \frac{u_c}{4\omega_c L_d L_q}\left\{(L_d-L_q)\sin 2\Delta\theta - j\left[(L_d+L_q)+(L_q-L_d)\cos 2\Delta\theta\right]\right\}
\end{aligned}
$$

(5.55)

where $\Delta\theta=\theta_X-\theta_d$ is the angle estimation error defined in figure 5.21. If we assume that the estimation error is small, i.e. $\sin 2\Delta\theta \approx 2\Delta\theta$, the real part of the extracted positive sequence component can be approximated as:

$$
\operatorname{Re}\left\{i_p^{(\omega_c t+\theta_X)}\right\} \approx \frac{u_c}{4\omega_c L_d L_q}\cdot(L_d-L_q)\cdot 2\Delta\theta
$$

(5.56)

The real part is linearly proportional to the angle estimation error $\Delta\theta$ and is fed to a *PLL tracking observer* (figure 5.23) to correct the estimation error. The tracking observer consists of a PI-controller and an integrator. The PI-controller use the real part of $i_p^{(\omega_c t+\theta_X)}$ (equation 5.56) to manipulate the estimated rotor speed ω_X. And the estimated rotor speed is then integrated and produces the estimated rotor angle θ_X. In [49] it is asserted that the observer is independent of motor parameter, one only need to adjust the parameter of the PI-controller properly. Considering equation 5.56, it is noticed that the motor parameters are actually relevant while tuning the PI-controller.

The negative sequence component $i_n^{(S)}$ of $i_c^{(S)}$ in equation 5.51 can also be utilized to estimate the rotor angle in the same way. Only the modulation with equation 5.52 should be changed to:

$$
I^{(-\omega_c t+\theta_X)} = I^{(S)}\cdot e^{j(\omega_c t-\theta_X)}
$$

(5.57)

And this shifts the negative sequence component to a frequency band around zero Hertz and shifts the positive sequence component to a frequency around $2\omega_c$. The angle estimation with the positive as well as the negative sequence component can be combined together to reduce estimation error.

5.3.4 Summary on the Active Rotor Angle Estimation Methods

In this section, the physical background, the classification and some examples of active rotor angle estimation methods for SM-PMSM have been introduced. This type of methods provides the possibility to estimate the rotor angle of SM-PMSM at very low and zero rotor speed. Approaches utilizing the strong magnetic saturation effect or the weak magnetic saturation effect (figure 5.17) can be found in the literature. Although much research has been done on such estimation methods, there are still significant problems unsolved. For methods utilizing the strong saturation with periodic pulse signal injection, the strong torque ripples can seriously disturb the motion control and also result in acoustic noise and shortened durability of the bearings. For methods utilizing the weak saturation effect with continuous carrier signal injection, the saturation related anisotropy of the inductance in a SM-PMSM is too weak for a robust estimation. Further more, the estimation will be erroneous under heavy mechanical load.

5.4 The Combined Rotor Angle Estimation for the Whole Rotor Speed Range

In section 5.2 and 5.3, examples of the existing rotor angle estimation approaches have been introduced. However, every category of estimation methods has its advantages and drawbacks. The flux linkage estimation with closed-loop integrator and amplitude limiter [21] successfully confines the estimated flux linkage on the origin-centered circle. But the estimated angle will still drift to a constant direction determined by the measurement error vector at very low rotor speed. The bigger the dc measurement error is, the faster the angle estimate drifts away at low rotor speed. The back-EMF based estimation can be adapted to fast speed change by proper design of the observer. However such methods are not applicable for very low (<100 rpm) and zero rotor speed due to the vanishing of the back-EMF. Active estimation methods provide though the possibility to estimate the rotor angle at zero speed, but the disturbance of strong torque ripple or the poor robustness are their main drawbacks. And the estimation can also be disturbed by big motor moment.

So far there is no mature angle estimation method for SM-PMSM which is applicable for the whole operation speed range including standstill. For high and medium rotor speed, back-EMF based angle estimation with observer is a robust method with small

computation effort compared to the Extended Kalman Filter approach. For very low rotor speed and standstill, the flux-linkage based method proposed by Hu and Wu [21] is the only reasonable choice at the moment due to the significant drawbacks of the active estimation methods. But as mentioned before, the angle estimate with this method still drifts to a constant after long time operation at low rotor speed. An ad hoc solution for this problem is to add a small but fast position variation to the position set value periodically if the rotor speed dwells under the speed threshold for long enough time. With this position set value manipulation, the rotor speed is forced to exceed the threshold after certain time dwelling in the very low speed range. And once the rotor speed is higher than the threshold, the closed-loop back-EMF based angle estimation will correct the drift and re-initialize the flux-linkage based estimation when the rotor speed falls below the threshold again. The period of this position set value manipulation depends on the offset error of the current measurement, which influence the drift speed of the angle estimate. The bigger the offset error is, the faster the drift will be and hence the shorter period should be chosen. The waveform of the additional position set value variation should be able to force the rotor speed to exceed the speed threshold; and the amplitude of the additional position variation should be as small as possible to minimize the disturbance on the brake moment control.

In the experiment square wave with the amplitude of π/2 rotor angle and the duration of 50ms had been added to the rotor position set value (before the low pass filter of the position controller). π/2 seems to be a rather big angle but due to the high transmission ratio of the gears, this rotation is not enough to close the air gap between the brake disk and the lining. Therefore, no brake moment will be produced by this additional rotor position variation if the driver does not want to brake. And this additional rotor angle variation results in an additional brake moment which is about 14% of the full brake moment of the wheel if the brake lining and brake disk come into contact. Under the measurement condition on the test bench, the rotor position set value will be manipulated if the rotor speed stays under 100 rpm for more than 200 ms.

The new estimations scheme is shown in figure 5.26. The rotor angle estimation is separated into the estimation at high and medium rotor speed and the estimation at very low and zero speed. For high and medium rotor speed ($\varpi_{mech} > 100\,\text{rpm}$) The back-EMF based estimation with observer in the α-β coordinate system is applied. The flux linkage estimation with closed-loop integrator and amplitude limiter [21] estimates the rotor position at very low speed and standstill. The switching between the estimation methods is controlled by the estimated amplitude of the back-EMF vector, because this amplitude is proportional to the amplitude of the rotor speed.
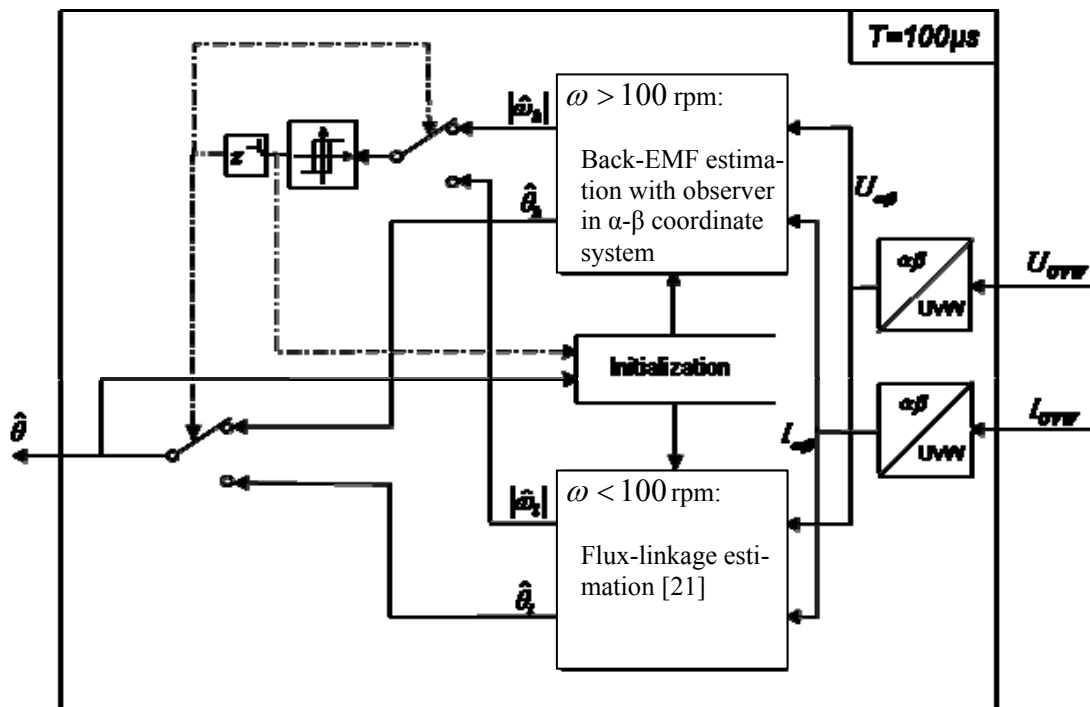
Figure 5.26: the structure of the rotor angle estimation module.

A hysteresis element is used for the switching so that frequent switching near the threshold can be avoided. The initialization unit prepares the initial values for the estimation methods at each switching. It basically saves the last estimated rotor angle before the switching, and uses this as the initial values for the next applied estimation algorithm. Hence, a 'jump' of the estimated rotor angle during switching will not occur. The voltage signals are the set values for the PWM pattern generation instead of voltage measurement. The whole estimation algorithm works at the sampling time of 100μs; while the position controller has the sampling time of 2.5ms. This sets the requirement on the convergence speed for the back-EMF based estimation. The continuous differential equations in the estimation methods are discretized and approximated with the Euler method in the digital implementation.

Chapter 6

The Experiment Results

In this chapter, the experiment results of the fault tolerant position control of the SM-PMSM are presented. The performance of the new position controller and the angle estimation are shown in section 6.1 and section 6.2. Section 6.3 shows the functionality of the whole fault tolerant position control by injecting fault into the measured signals from the AMR angle sensor.

The SM-PMSM under test has a maximal rotor speed of 6000 rpm and a maximal motor moment of 1.2 Nm (at zero speed). Except for the position controller; the other algorithms have 10 kHz sampling rate (T=100 μs). The position controller has a sampling rate of 400 Hz (T=2.5 ms). The continuous algorithms are approximated with the backward Euler method in the digital implementation, i.e.:

$$\dot{x}_n = \frac{x_n - x_{n-1}}{T} \tag{6.1}$$

T is the sampling interval.

6.1 The Test of the Position Controller

The position control design in section 3.1.2 is tested with a step function as position set value. The step function corresponds to 4 revolutions of the rotor. The brake moment produced by this rotor rotation is enough to block the wheel. In the figure 6.1, the electrical rotor angle is shown, which is twice the rotor angle is. Because the motor has two pole pairs. The response speed of the position control is dominated by the delay time constant of the low-pass filter that pre-filters the original position set

value. This makes it very simple to adjust the dynamics of the position control. The low-pass filter is a first-order delay element. Its time constant is chosen so that the smoothened set value reaches 95% of the original set value at 100 ms delay. The parameters are first tuned with the offline motor model and than fine-tuned during the test bench implementation.
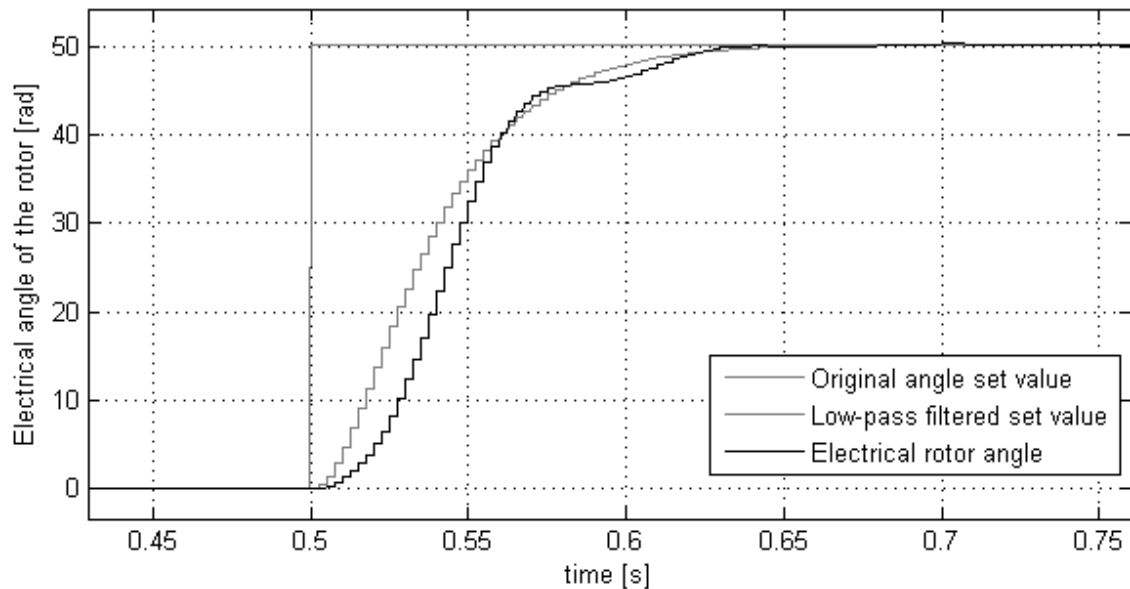
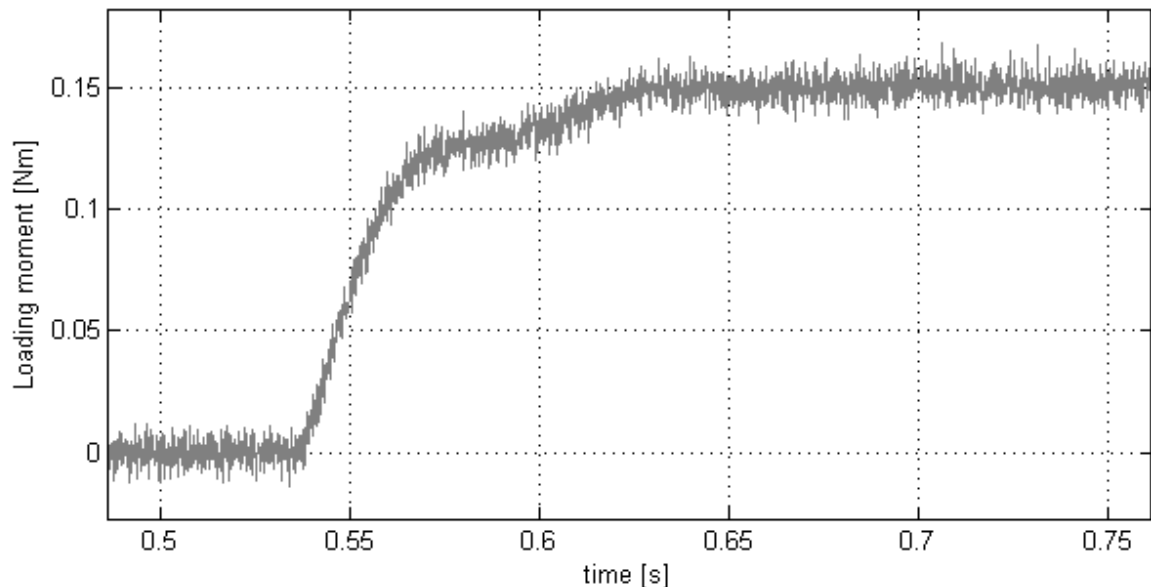**Figure 6.1: the rotor angle set value and the rotor angle.**

Figure 6.2: the loading moment on the motor shaft. The loading moment is produced by the other SM-PMSM on the test bench.
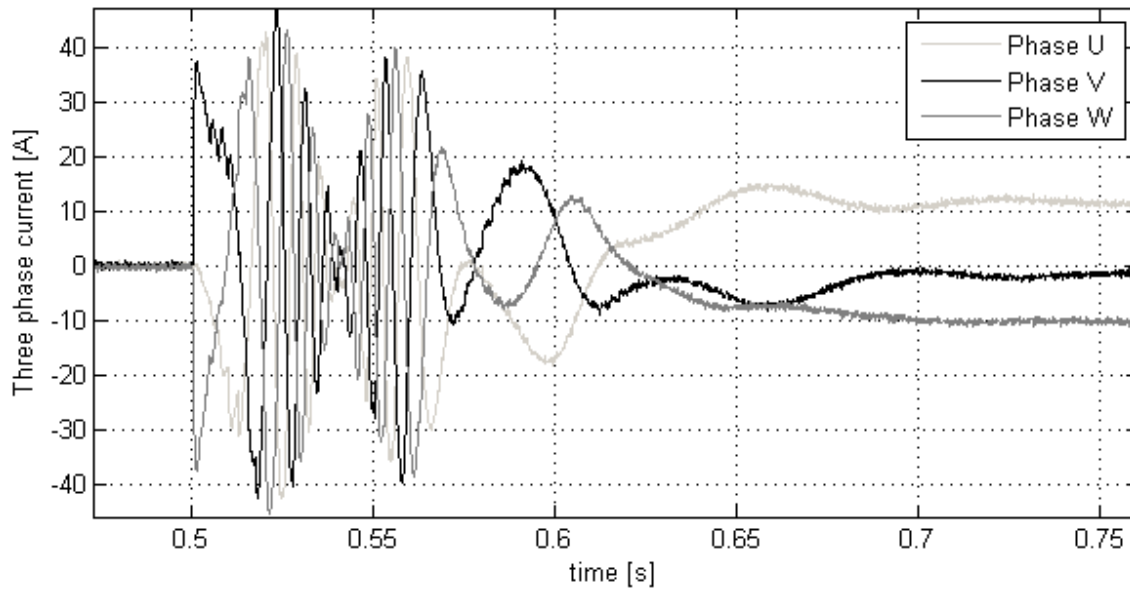
Figure 6.3: the three phase current of the test motor.

The loading moment is calculated by the model of the brake caliper according to the motor angle. And the loading moment is produced by the other SM-PMSM on the test bench (loading machine). The advantage of wedge brake can be noticed in figure 6.2. Namely, only 0.15 Nm motor moment is necessary for full braking. The high-frequency disturbance is caused by imperfect current control of the loading machine. The motor current is also shown in figure 6.3.

6.2 The Performance of the Combined Rotor Angle Estimation

The performance of the combined rotor angle estimation is tested with two motor operations; namely, zero speed operation and the ABS operation. As mentioned in section 5.4; if the rotor speed dwells below the threshold (100 rpm) for more than 0.2 s, a square wave will be added to the original angle set value. The square wave has a length of 50ms and amplitude of π (electrical angle). The amplitude corresponds to 90 degree rotor rotation. The period, amplitude and duration of this set value manipulation are determined during the experiment empirically. The purpose is to force the rotor speed to exceed the threshold so that the closed-loop back-EMF based angle estimation can correct the drift of the flux linkage based estimation at low speed. The period is actually determined by the drift speed which is related to the motor current measurement quality. The faster the drift is the shorter the period should be. The ABS operation uses the rotor position waveform from an ABS brake actuation as the

rotor position set value. This operation is a mixture of highly dynamic rotor position variation and long time low speed operation.

The manipulated rotor position set-value, the rotor angle and the angle estimate are shown in figure 6.4. The added square wave can be seen in the figure. The switch signal indicates which angle estimation method is active. Zero means the flux linkage based estimation for low rotor speed. And one means the back-EMF based estimation for high and medium rotor speed. Since the estimation error is very small compared to the position control deviation, the area marked by the square in figure 6.4 is enlarged and shown in figure 6.5. In this figure, the drift of the angle estimation at zero speed is shown clearly. Once the back-EMF based estimation is active, the drift is corrected.
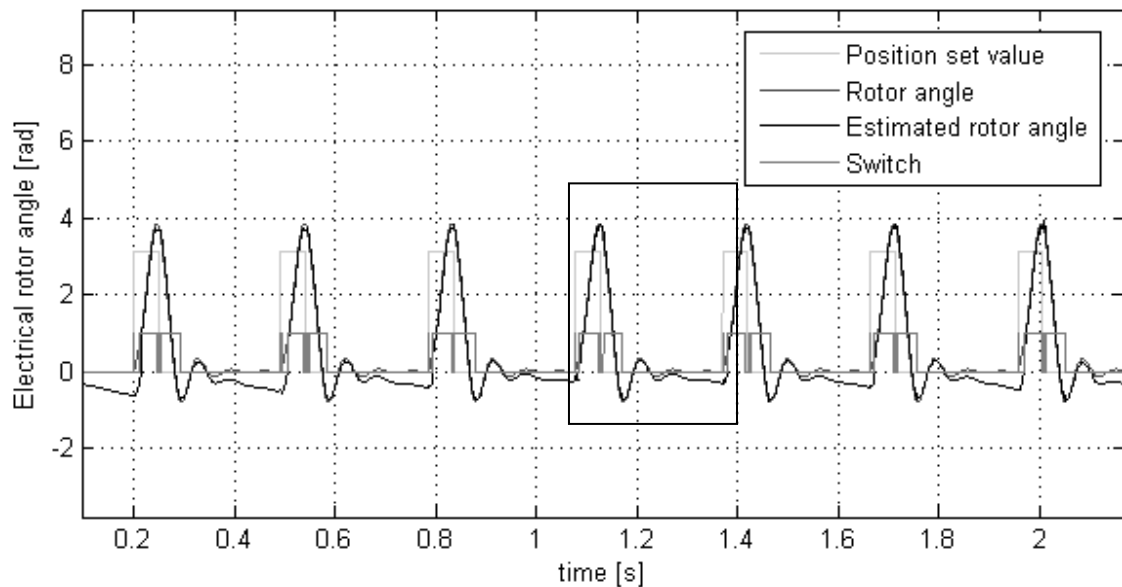
Figure 6.4: the rotor position in the zero speed operation. Square waves are added to the zero position set value periodically so that the drift of the angle estimate at low speed can be corrected by the closed-loop estimation at high speed.
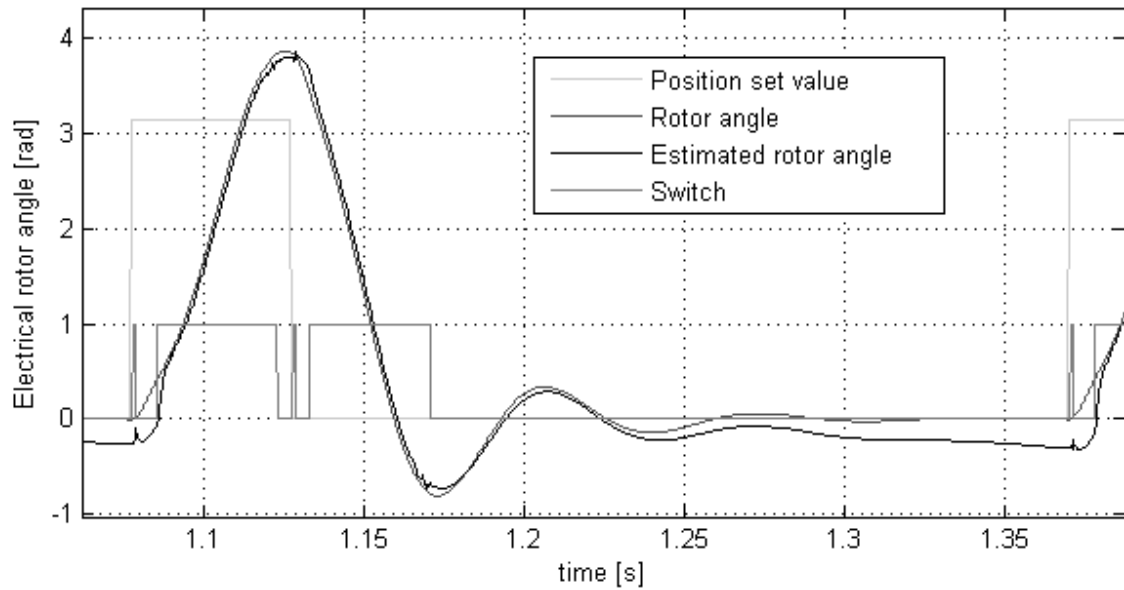
Figure 6.5: the enlarged plot of the area marked by the square in figure 6.4.

The estimated rotor angle is illustrated in figure 6.6. The assumption for the back EMF based estimation that the real rotor speed and the estimated speed are approximately the same is valid. The estimated back EMF is shown in figure 6.7 and 6.8. The real value of the back EMF is not measured directly but calculated from the measured rotor angle and rotor speed.
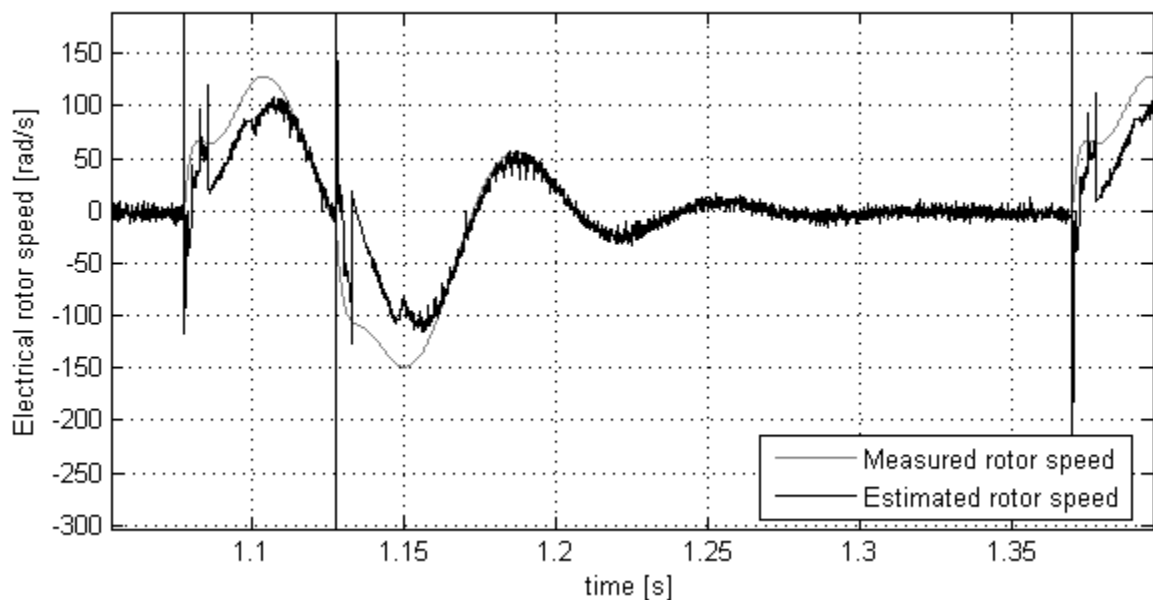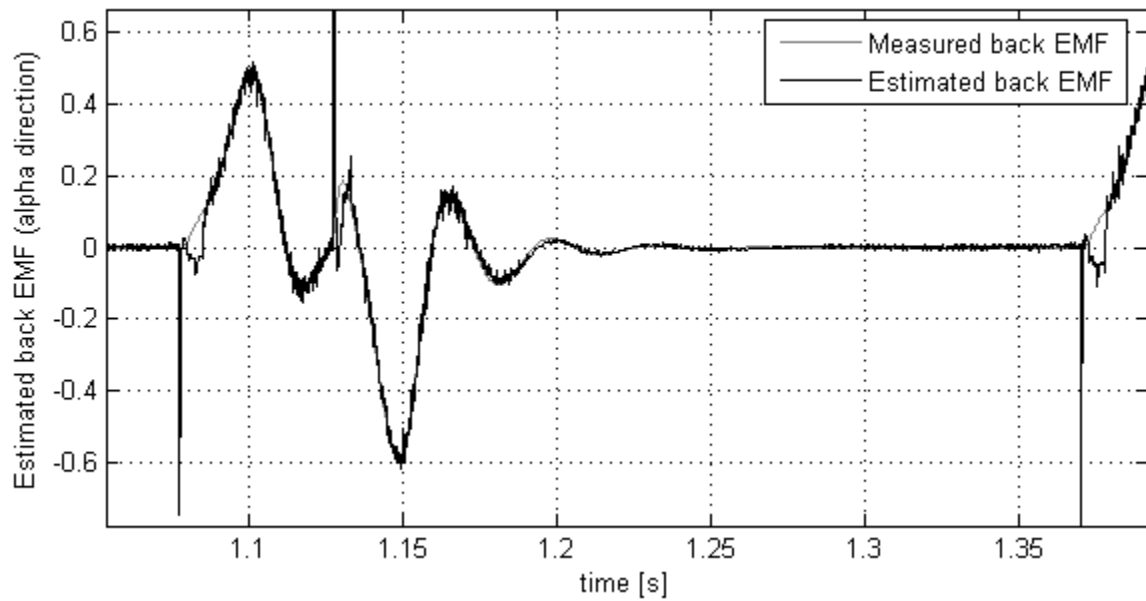

Figure 6.6: the estimated rotor angle.

Figure 6.7: the estimated back EMF (component on alpha axis).
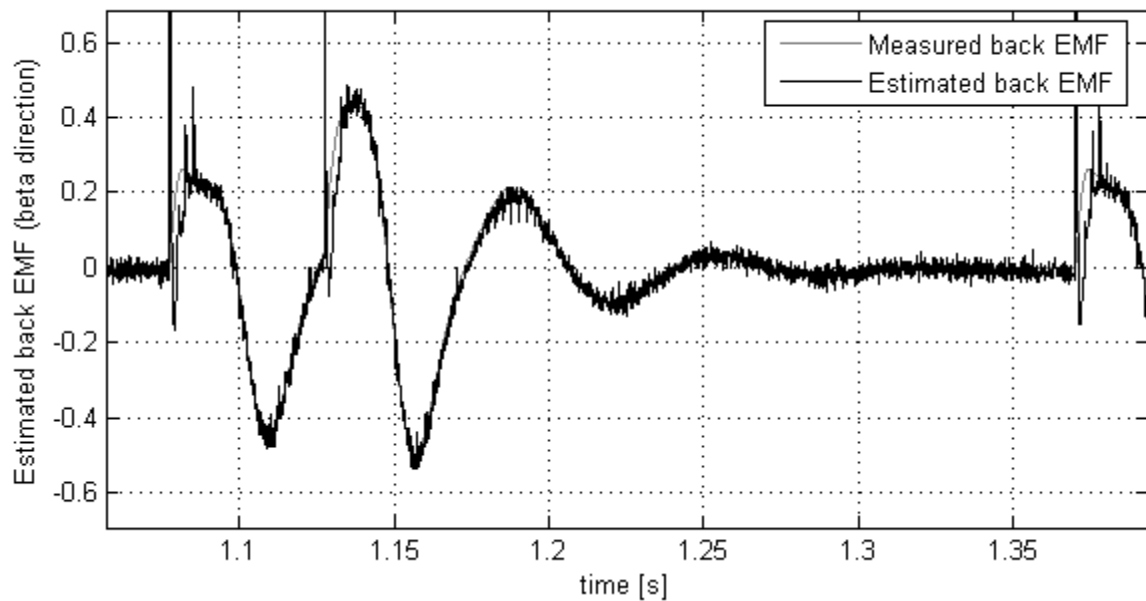
Figure 6.8: the estimated back EMF (component on beta axis).

Figure 6.9 shows the rotor position set-value, the rotor angle and the estimated angle in the ABS operation. The switch signal is ten times amplified. The back EMF based angle estimation under highly dynamic rotor angle variation between 0 s and 2 s is very successful. The periodic small position variation between 1.7 s and 5.6 s is caused by the added square wave in the position set value. Because in this time interval, the rotor speed often stays under the threshold for more than 0.2 ms.
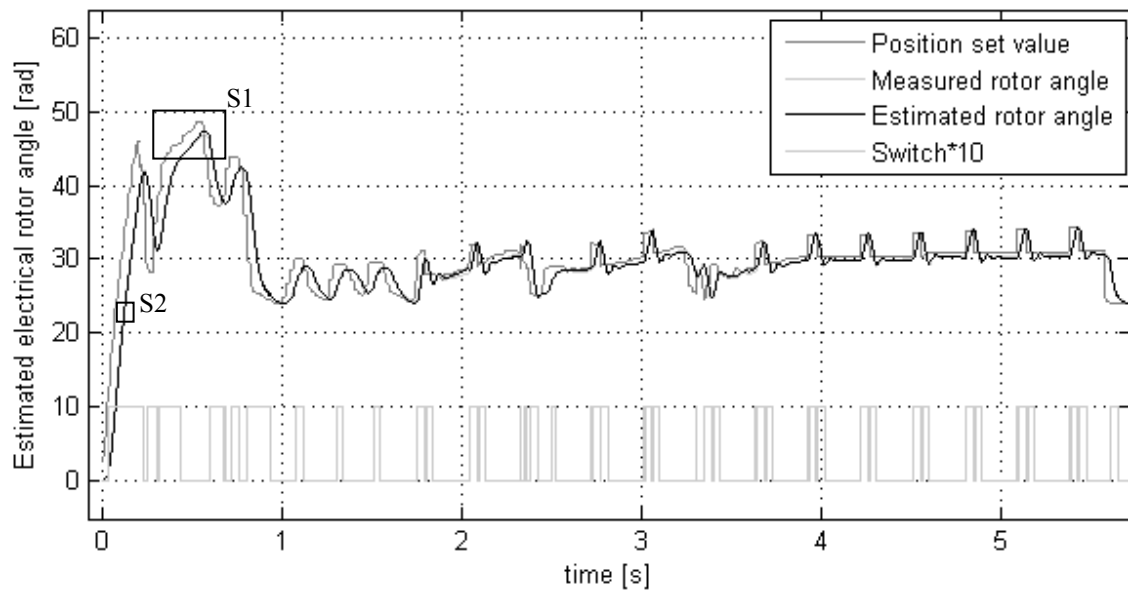
Figure 6.9: the rotor position set value, the rotor angle and the angle estimate in the ABS operation. The switch signal is shown with an amplification factor 10 so that it can clearly be seen.
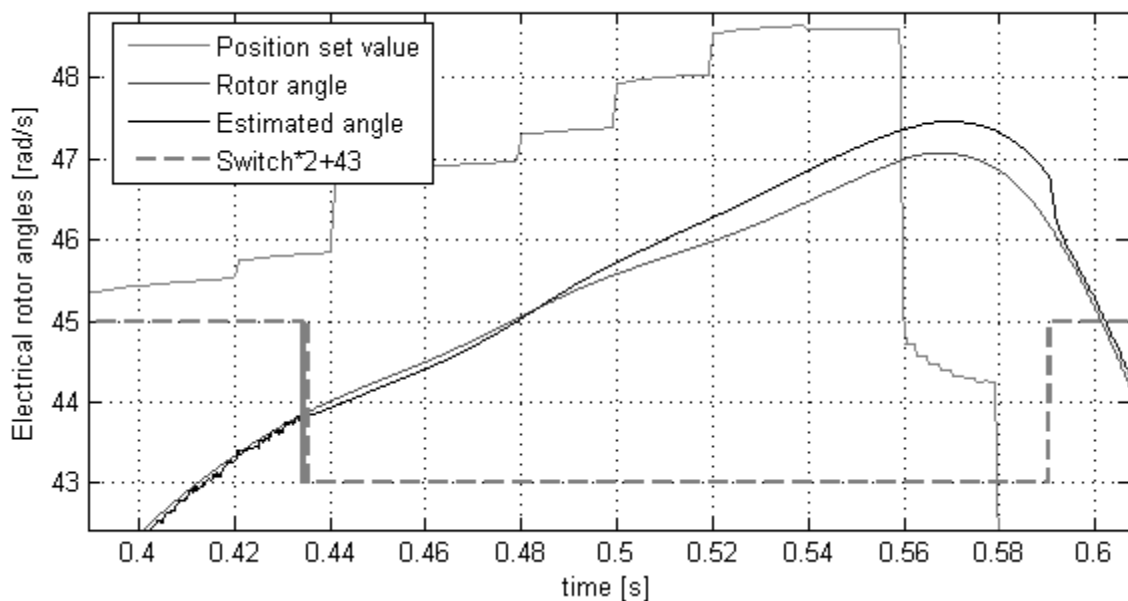
Figure 6.10: enlargement of the area S1 in figure 6.9. The switch signal is adapted to the window. The step-form discontinuity in the position set value is due to the sample rate in the ABS system (50 Hz, T=20 ms).

For a closer look at the performance of the combined angle estimation method; the area marked by the square *S1* in figure 6.9 is shown in figure 6.10. The step-form discontinuity in the position set value is caused by the low sample rate of the ABS system (50 Hz, T=20 ms). The switch signal is shifted and twice amplified to adapt to the observation window. In this figure, the transition between the estimation at low rotor speed and high speed is illustrated. The high frequency disturbance before the

flux linkage based estimation is active is caused by the small amplitude of the back-EMF vector.

The area marked by the square *S2* in figure 6.9 is also enlarged and shown in figure 6.11. The purpose is to show the delay of closed-loop angle estimation for high and medium rotor speed based on back-EMF. The delay is about 0.7 ms. Due to the high enlargement factor, the position set value can not be shown in the same figure. Because the position control deviation is much bigger than the angle estimation error.
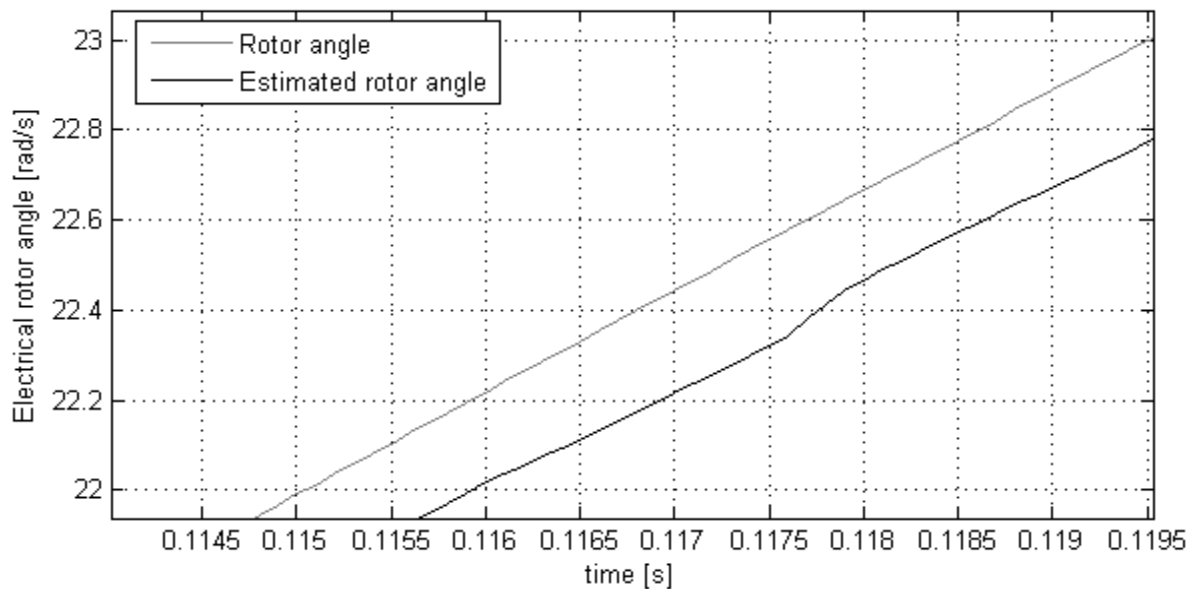
Figure 6.11: the enlarged illustration of the area marked by the square S2 in figure 6.9.

6.3 Test of the Fault Tolerant Control

In this section, the test result of the whole fault tolerant position control loop is presented. The fault injection (figure 2.5) manipulates the measured signals from the AMR angle sensor. Four types of fault can be injected in each channel of the AMR sensor (sine, cosine); namely, amplitude fault; offset fault; constant signal fault and zero-mean Gauss noise with adjustable variance. Although four types of fault can be injected in the AMR output signals per software and various motor operations can be tested, only two special cases are illustrated here. Because otherwise there will be too many plots. The purpose of this illustration is to show the basic functionality of the fault tolerant position control algorithm. In the first case, the fault injection manipulates the AMR outputs (sine, cosine channels) to stay constant. In the other case, the amplitude of the sine channel is manipulated with an amplification factor of 2. A sine wave with a period of 0.5 s and amplitude of 10 is chosen as the position set value.

The position set value, the angle calculated with AMR sensor outputs and the estimated rotor angle are shown in figure 6.12. The sine and cosine channels of the AMR sensor are forced to stay at constant after the fault injection (figure 6.13). Therefore the angle calculated with these signals also stays constant. The position control with estimated rotor angle is active after the decision making module changes the control mode. The real rotor angle is also shown in this figure as reference. Three statuses are shown in figure 6.14; namely the fault status from the model-based plausibility check; the fault status from the monitoring of the circular measurement locus (radius check); and the control mode determined by the decision making module. The fault status of the plausibility check and the fault status of the radius check are shifted vertically for better comparison. Status *low* means fault-free. For the control mode, 1 means control with measured angle and 2 means control with estimated angle. The supply voltage and the status of the current sensors are assumed to be correct through out the whole experiment and are hence not depicted. Since the constant AMR outputs are still on the standard circle (figure 4.8), the radius check is not able to detect the fault. The plausibility check compares the measured angle and the angle estimate and can therefore report the fault even. Because the rotor is rotating in a sinusoidal manner, there are still intersections between the erroneous constant angle and the estimated angle (figure 6.12) periodically. This explains why the fault status of the plausibility check returns to *low* periodically (figure 6.14). But due to the switching rule of the decision making module discussed in section 4.4; the position controller is not switched back to use the angle from the AMR sensor again (figure 6.14).

The area marked by the square in figure 6.12 is enlarged in figure 6.15. The AMR sensor outputs and the fault statuses in this time interval are illustrated in figure 6.16 and 6.17. In figure 6.17, a delay of the control mode change can be noticed. This is caused by the low-pass filtering of the fault statuses from the fault detection module before they are fed to the decision making module. This is done in order to avoid false alarm caused by impulse-type disturbance. The delay is less than 1 ms and hence will not affect the position control that has a sample interval of 2.5 ms.
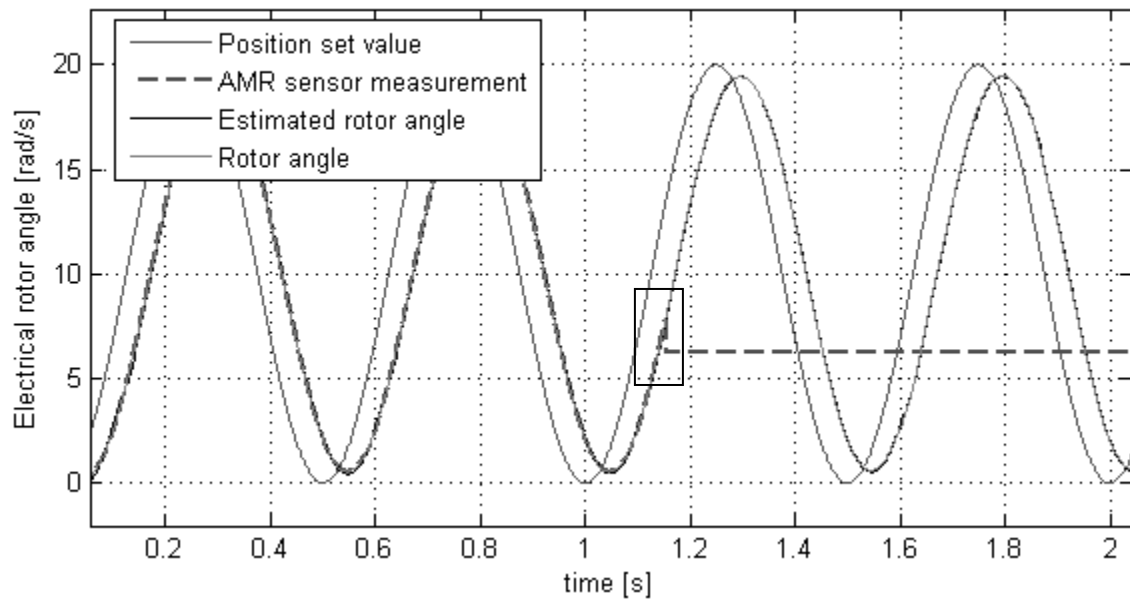
Figure 6.12: the position set value; the angle calculated with AMR sensor signals; the estimated rotor angle and the real rotor angle. The sine and cosine outputs of the AMR sensor are forced to stay constant after fault injection.
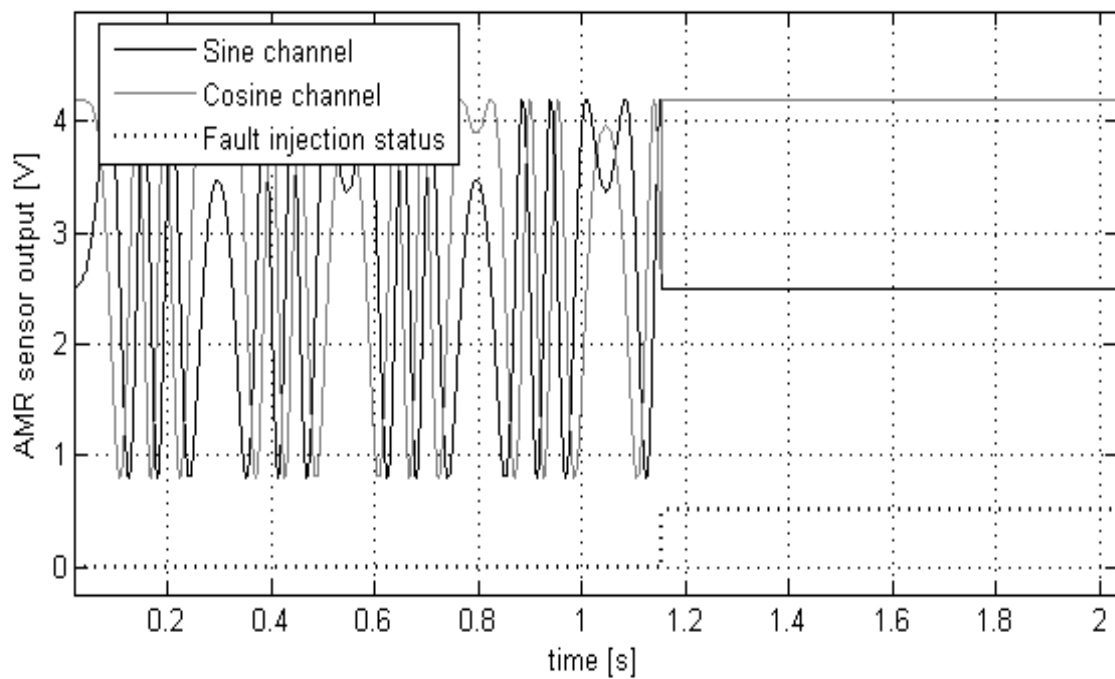

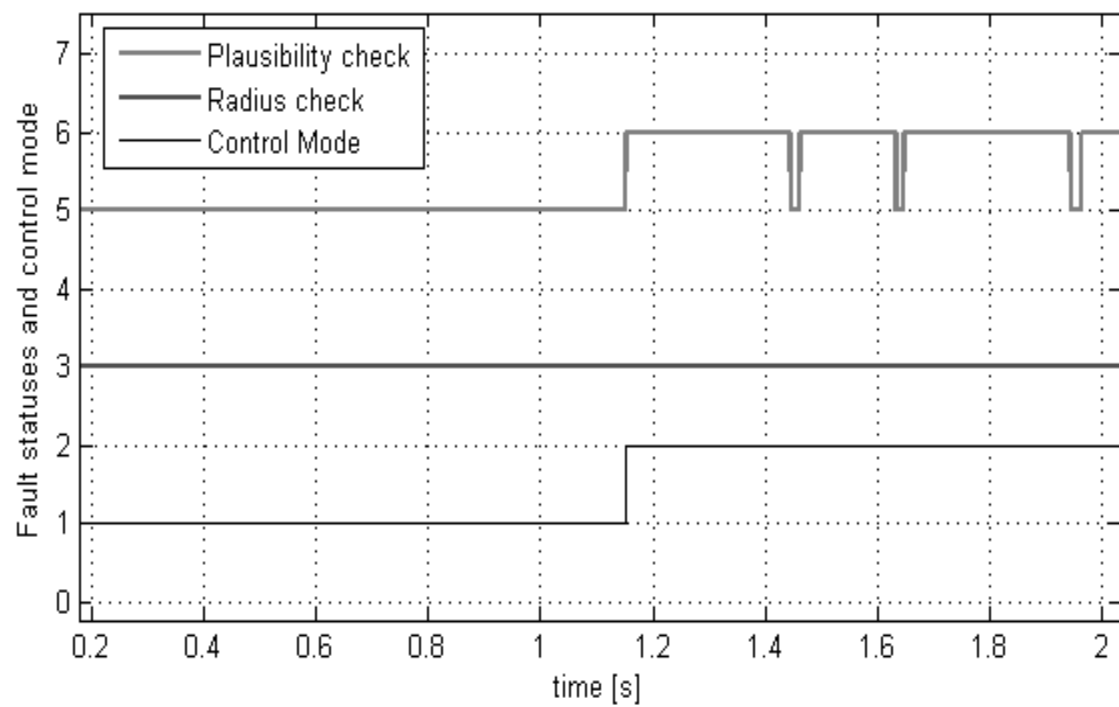**Figure 6.13: the sine and cosine outputs of the AMR sensor. After the fault injection, both stay constant.**

Figure 6.14: the fault statuses from the model-base plausibility check and the radius check. The control mode is changed by the decision making module after fault is detected.
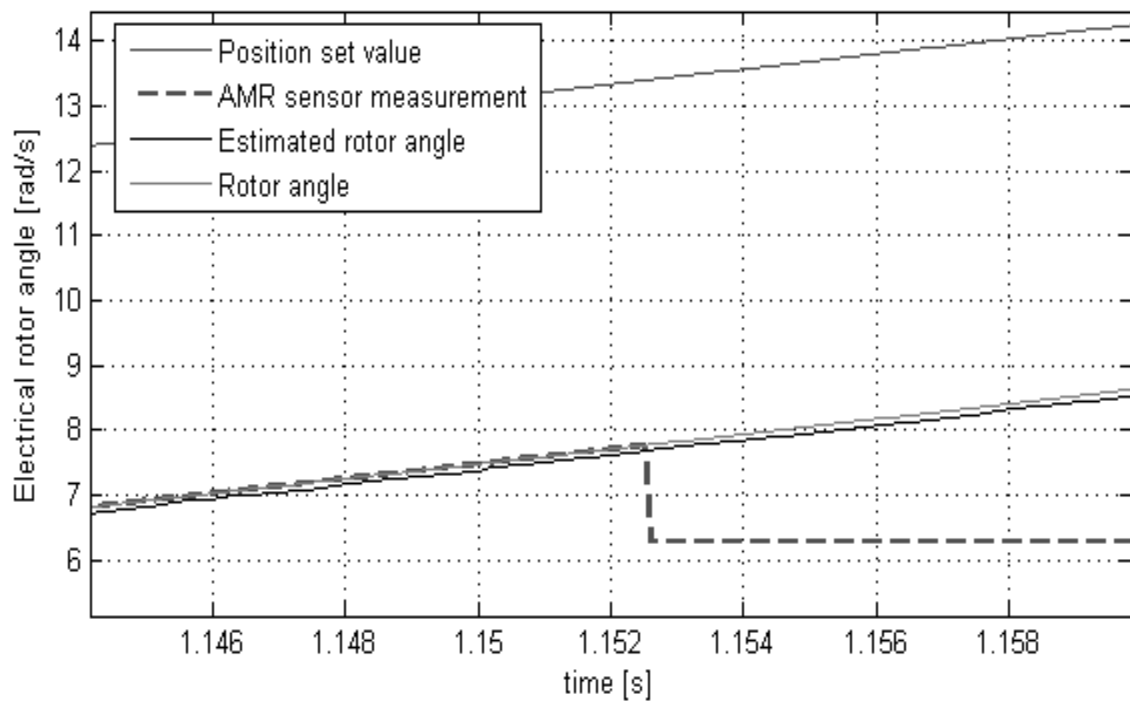
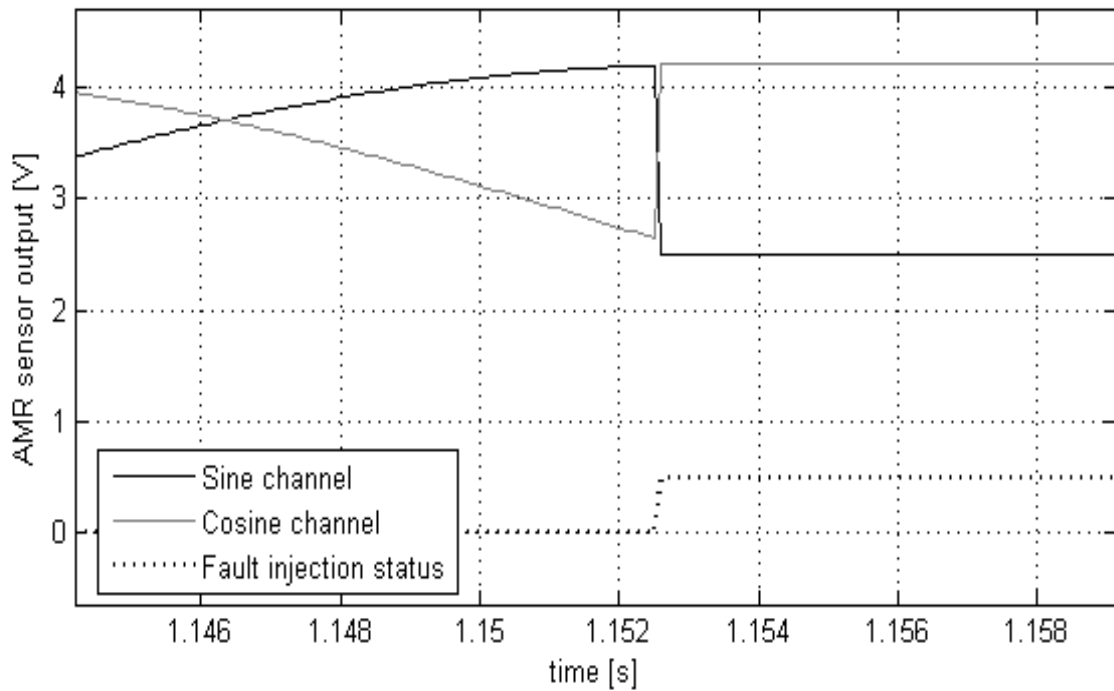**Figure 6.15: enlargement of the area marked in figure 6.12**

Figure 6.16: the AMR sensor outputs in the same time interval as figure 6.15.
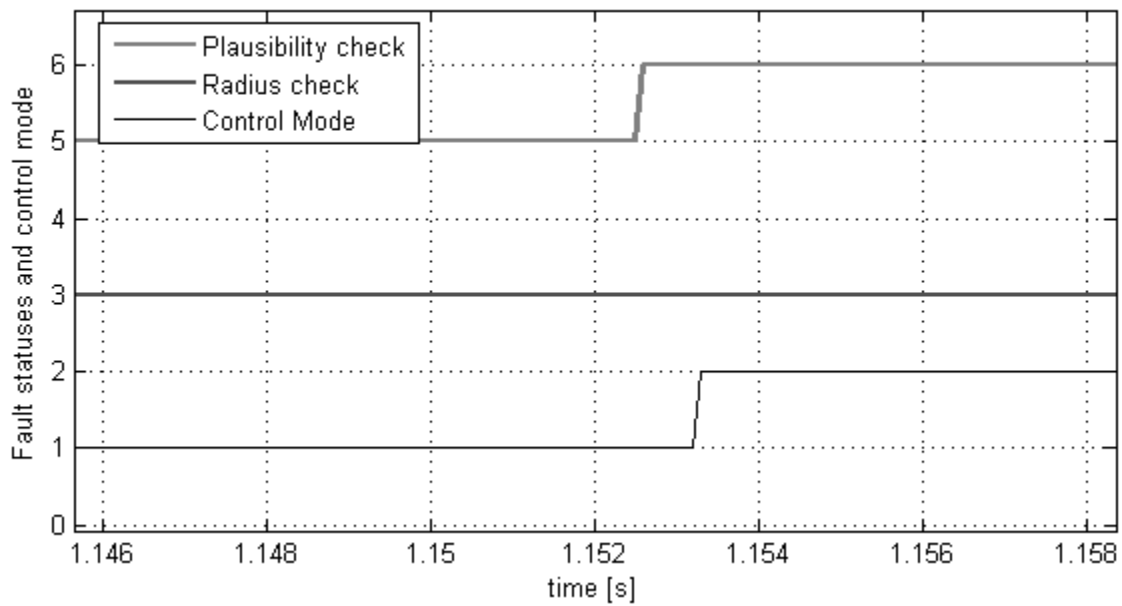

Figure 6.17: the fault statuses and the control mode in the same time interval as figure 6.15.

The test results of injecting amplitude fault in the sine channel of the AMR sensor are shown in the same manner. The figure 6.18 shows the position set value, the angle calculated with AMR sensor outputs, the estimated rotor angle and the real rotor angle. The area marked is enlarged in figure 6.21. The sine channel of the AMR sensor is amplified with a factor of 2. The angle error can be seen clearly in figure 6.21. But this angle error is too small to violate the plausibility check (figure 6.20 and fig-

ure 6.23). The error threshold of the plausibility check is set rather big to tolerate the drift of the angle estimate at low rotor speed.
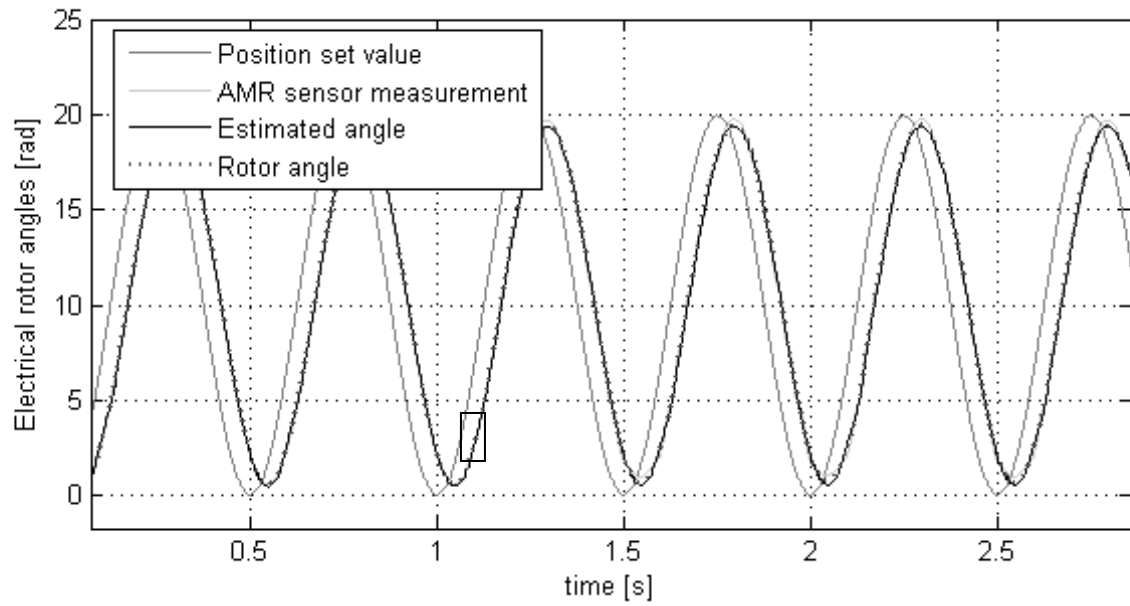

Figure 6.18: the position set value, the angle from AMR sensor, the estimated angle and the real rotor angle.
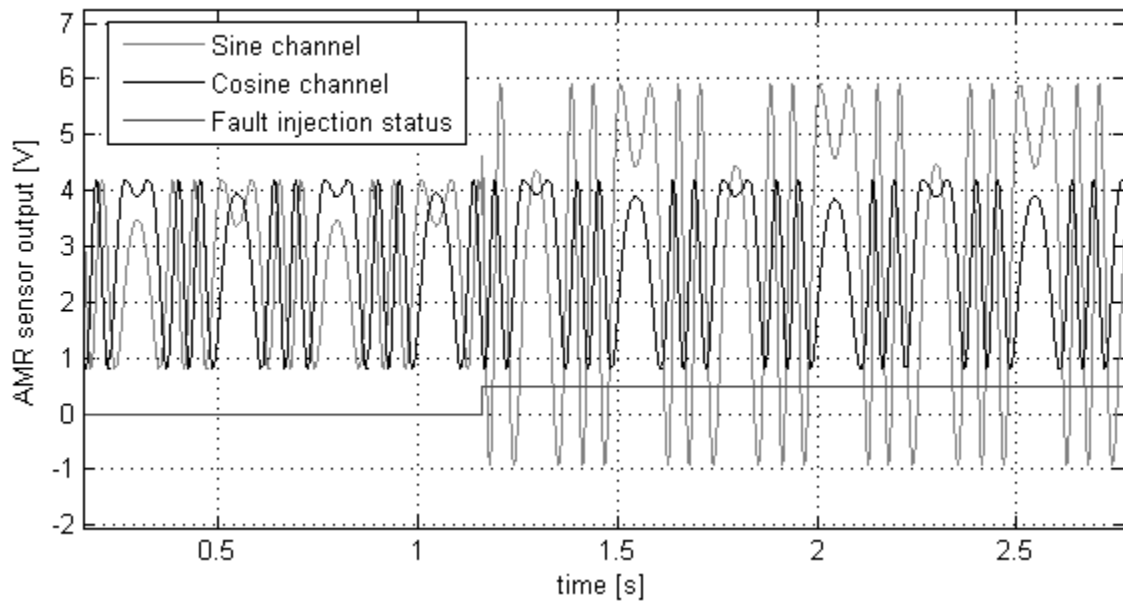

Figure 6.19: the AMR sensor outputs. After the fault injection, the sine channel is amplified with a factor of 2.
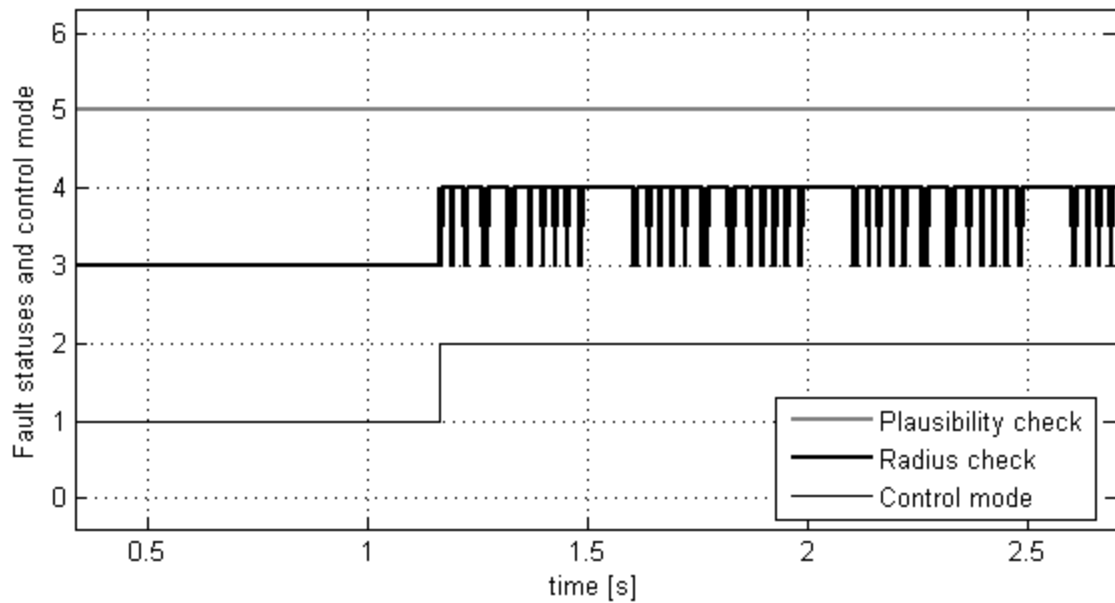
Figure 6.20: the fault statuses and the control mode.

The radius check successfully detects the fault. Because by changing the amplitude of the sine channel, the locus of the measurement from AMR sensor becomes an ellipse (equation 4.8). But this ellipse has intersections with the standard circle because the amplitude of the cosine channel and the offset of both channels are unchanged. This explains why the fault status from the radius check returns to low frequently (figure 6.20).
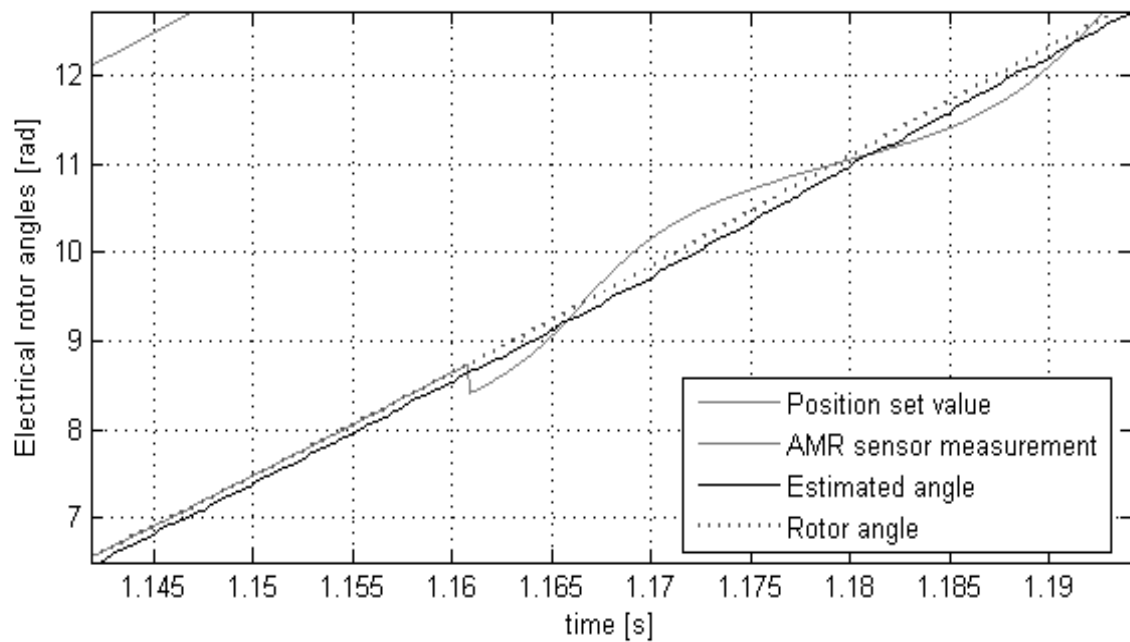

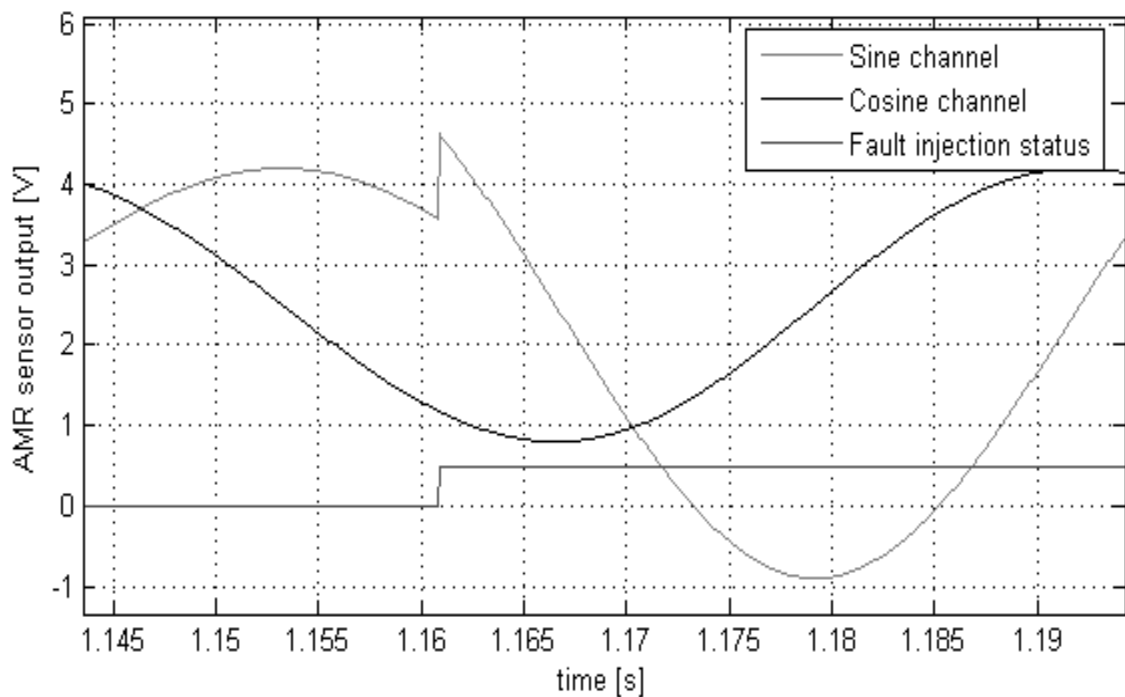**Figure 6.21: enlargement of the area marked in figure 6.18.**

Figure 6.22: the outputs of the AMR sensor in the same time interval of figure 6.21.
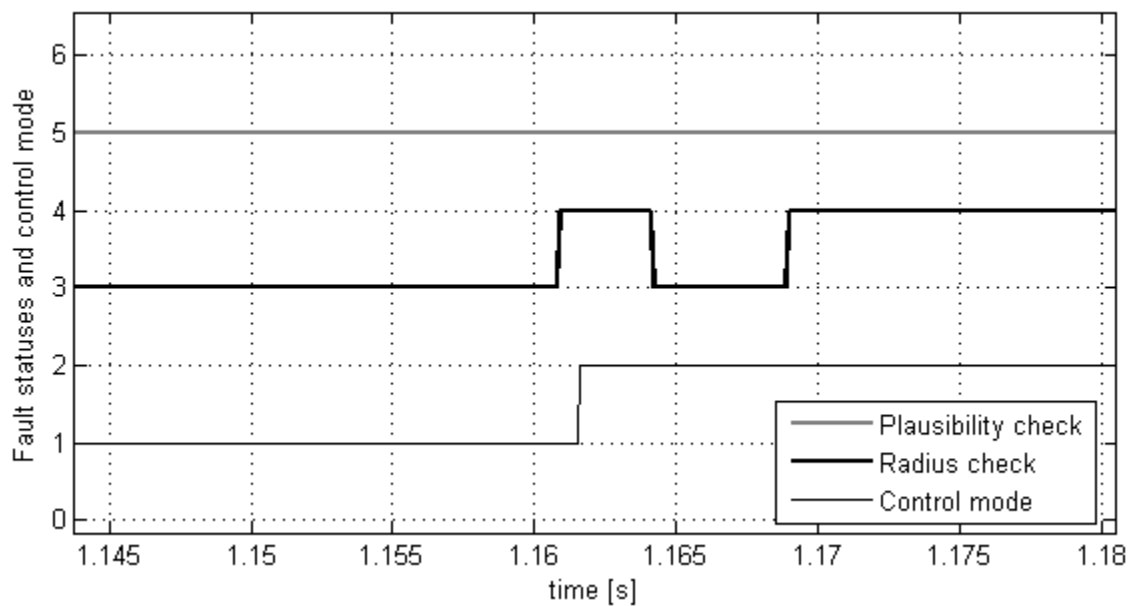

Figure 6.23: the fault statuses and control mode in the same time interval of figure 6.21.

The position control with estimated rotor angle in two other motor operations is also demonstrated here. Figure 6.24 illustrates the zero speed operation, in which the original position set value is constantly zero. Square waves are added to the position set value automatically if the rotor speed has been lower than the threshold for more than 0.2 s. The real rotor angle does not converge to the set value due to the error of the angle estimate. It should be noted that the dynamic of the position controller should be much lower than the closed-loop angle estimation to avoid stability prob-

lem. Figure 6.25 illustrates the test result of the position control with estimated rotor angle in ABS operation. And figure 6.26 shows the loading moment on the rotor shaft in the ABS operation.
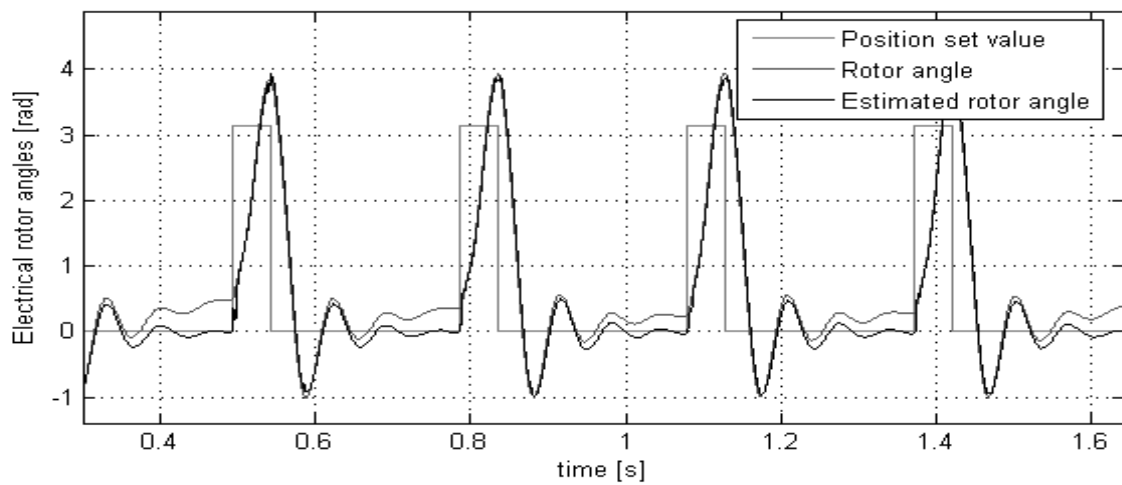
Figure 6.24: position control with estimated rotor angle. The original position set value is constantly zero. The square waves are added because the rotor speed is lower than the threshold for longer than 0.2 s.
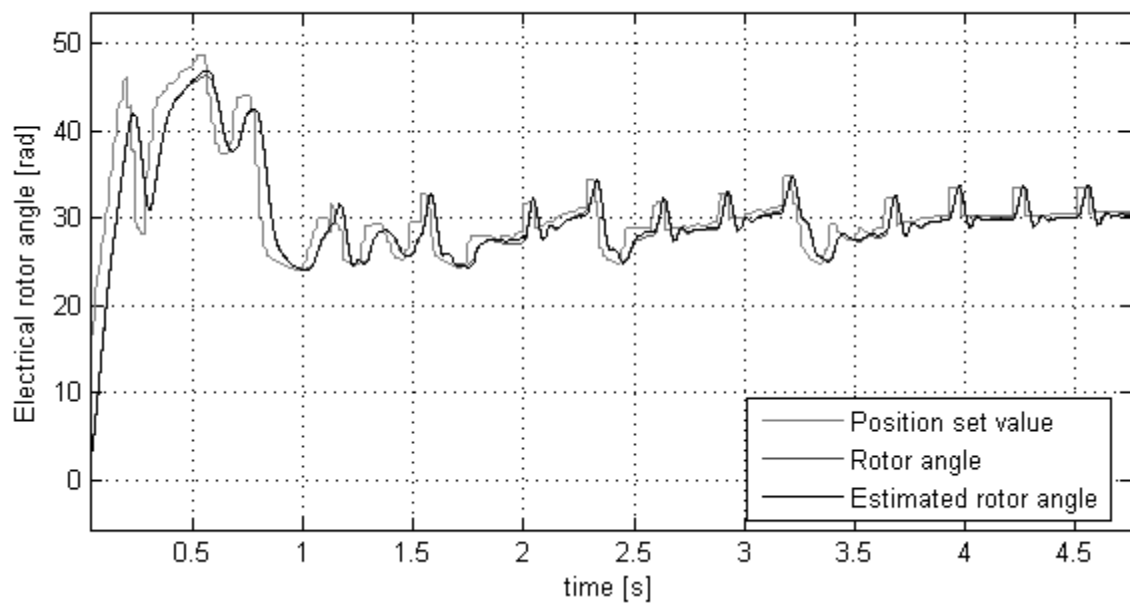
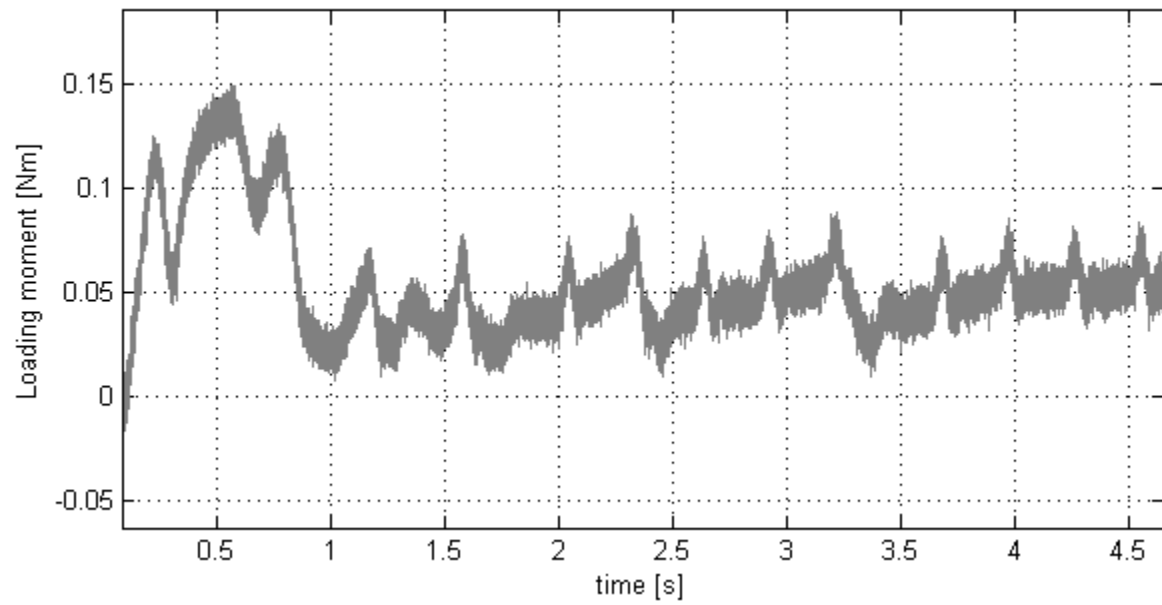**Figure 6.25: position control with estimated rotor angle in ABS operation.**

Figure 6.26: the loading moment on the rotor shaft in the ABS operation.

Chapter 7

Summary and Outlook

In this study, the fault tolerant position control is designed for the SM-PMSM in the brake actuator of an electro-mechanical wedge brake. The following results have been achieved:

1. An active fault tolerant control scheme is proposed with online switching of the source of angle information for the position controller.
2. The fault behavior of the AMR angle sensor is investigated and a fault detection module is designed.
3. The rotor angle estimation of an SM-PMSM in the whole rotor speed range is studied and an ad-hoc solution is proposed for the application in the specific brake actuator.
4. A position controller with single closed-loop structure instead of cascaded closed-loop structure had also been developed.
5. For the validation of the algorithm with real SM-PMSM hardware, a rapid control prototyping test bench had been setup.

The fault tolerant solution avoids brake actuator shut down when the only rotor angle sensor in the actuator fails. This pure software fault tolerant solution increase the availability of the brake actuator without any change on the hardware design. The parameter tuning of the position control is very simple thanks to its simple structure.

So far there is no mature angle estimation method for SM-PMSM which is applicable for the whole operation speed range including standstill. Although the ad-hoc solution is applicable, a robust estimation method without manipulating the position set value or other side effects is still desired. Because with the proposed position set value manipulation, the motor is almost always moving. Although the additional ro-

tation is small, this can still influence the durability of the mechanical parts, e.g. bearing, rack gear, etc. For the set value manipulation in the ad-hoc solution, the wave form of the additional rotor angle variation is still to be optimized.

Another possibility is to use motor with inherent inductance anisotropy, e.g. motor with buried magnet. For such machine, position sensorless control technique is already in commercial use.

Appendix A:

The Coordinate Systems and Transformations

The analysis with the fundamental frequency machine model applies many coordinate systems. This appendix makes an explanation on all the coordinate systems in this dissertation. The analysis of the machine will be carried out in the equivalent single-pole-pair machine. The definitions of the coordinate systems are shown in figure A.1. Most trivial is the U-V-W coordinate system that indicates the directions of the magnetic motive force (mmf) generated by the three phase winding current. The α-β coordinate system is stator-fixed and the α-axis is aligned with the U-axis. The d-q coordinate system is synchronous to the rotor, and the d-axis is aligned with the direction in which the sinusoidal distributed permanent magnet flux reaches its maximum. For the analysis on the rotor position estimation in chapter 5, an orthogonal coordinate system dc-qc with arbitrary rotation angle is also defined.
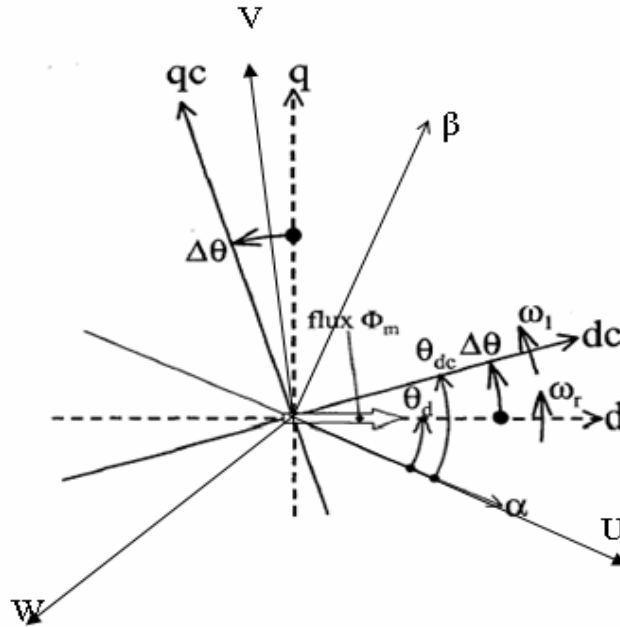

Figure A.1: definitions of coordinate systems

The *Clarke transformation* converts the *balanced* 3-phase quantities in the U-V-W coordinate system into the α-β coordinate system. The Transformation is represented by equation A.1 in matrix form:

$$
\begin{pmatrix} v_\alpha \\ v_\beta \\ v_0 \end{pmatrix} = \frac{2}{3} \begin{bmatrix} 1 & \cos\dfrac{2\pi}{3} & \cos\dfrac{4\pi}{3} \\ 0 & \sin\dfrac{2\pi}{3} & \sin\dfrac{4\pi}{3} \\ \dfrac{1}{2} & \dfrac{1}{2} & \dfrac{1}{2} \end{bmatrix} \cdot \begin{pmatrix} v_U \\ v_V \\ v_W \end{pmatrix}
\tag{A.1}
$$

The inverse Clarke transformation is:

$$
\begin{pmatrix} v_U \\ v_V \\ v_W \end{pmatrix} = \begin{bmatrix} 1 & 0 & \dfrac{1}{2} \\ \cos\dfrac{2\pi}{3} & \sin\dfrac{2\pi}{3} & \dfrac{1}{2} \\ \cos\dfrac{4\pi}{3} & \sin\dfrac{4\pi}{3} & \dfrac{1}{2} \end{bmatrix} \cdot \begin{pmatrix} v_\alpha \\ v_\beta \\ v_0 \end{pmatrix}
\tag{A.2}
$$

where the quantity v can be any balanced 3-phase quantities, e.g. current, voltage. It should be noted that the inverse transformation is only valid if the 3-phase system is balanced, i.e.

$$
v_0 = \frac{v_U + v_V + v_W}{3} = 0
\tag{A.3}
$$

The *Park Transformation* converts the quantities in the stator-fixed α-β coordinate system into the rotor-synchronous d-q coordinate system:

$$
\begin{pmatrix} v_d \\ v_q \end{pmatrix} = \begin{pmatrix} \cos\theta_d & \sin\theta_d \\ -\sin\theta_d & \cos\theta_d \end{pmatrix} \cdot \begin{pmatrix} v_\alpha \\ v_\beta \end{pmatrix}
\tag{A.4}
$$

The inverse Park Transformation is:

$$
\begin{pmatrix} v_\alpha \\ v_\beta \end{pmatrix} = \begin{pmatrix} \cos\theta_d & -\sin\theta_d \\ \sin\theta_d & \cos\theta_d \end{pmatrix} \cdot \begin{pmatrix} v_d \\ v_q \end{pmatrix}
\tag{A.5}
$$

Sometimes the Clarke transformation and Park transformation are combined into one transformation to convert the quantities in U-V-W system directly into d-q system. But again, the inverse of this transformation is only valid if the 3-phase system is balanced; since the Clarke transformation is involved.

Bibliography

[1]   Schröder, D.
        Elektrische Antriebe 2: Regelung von Antrieben.
        Springer-Verlag Berlin Heidelberg 1995. ISBN 3-540-57610-X.

[2]   Nguyen, P.Q. ; Dittrich, J-A.
        Praxis der feldorientierten Drehstromantriebsregelungen.
        Expert-Verlag 1999. 2nd Edition, ISBN 3-8169-1698-8.

[3]   Isermann, R.
        Überwachung und Fehlerdiagnose:
        Moderne Methoden und ihre Anwendungen bei technischen Systemen.
        VDI-Verlag, Düsseldorf 1994. ISBN 3-18-401344-8.

[4]   Mahmoud, M. M.; Jiang, J.; Zhang, Y.
        Active Fault Tolerant Control Systems: Stochastic Analysis and Synthesis.
        Springer-Verlag Berlin Heidelberg 2003. ISBN 3-540-00318-5.

[5]   Patton, R.J.
        Fault-Tolerant Control: The 1997 Situation.
        Proceeding of the IFAC Symposium SAFEPROCESS' 97, Hull, UK, pages
        1033-1055,1997.

[6]   Isermann, R.
        Supervision, fault-detection and fault-diagnosis methods-An introduction.
        Control Engineering Practice, 5, no. 5:639-652, 1997.

[7]   Birolini, A.
        Reliability Engineering: Theory and Practice.
        Springer-Verlag Berlin Heidelberg 2004, fourth edition. ISBN 3-540-40287-X.

[8]   Chen, J.; Patton, R.J.
        Robust Model-based Fault Diagnosis for Dynamic Systems.
        Kluwer Academic Publishers 1999. ISBN 0-7923-8411-3.

[9]   Simani, S.; Fantuzzi, C. and Patton, R.J.
        Model-based Fault Diagnosis in Dynamic Systems Using Identification Techniques.
        Springer-Verlag London Berlin Heidelberg 2003. ISBN 1-85233-685-4.

[10]   Astroem, K.J.; Albertos, P.; Blanke, M.; Isidori, A.; Schaufelberger, W.; Sanz, R.
        Control of Complex Systems.
        Springer-Verlag 2001. ISBN 978-1-85233-324-9

[11]   Maki, M.; Jiang, J.; Hagino, K.
        A stability guaranteed active fault tolerant control system against actuator failures.
        Proceedings of the 40th IEEE conference on Decision and Control, Orlando, FL, USA, pages 1893-1898, 2001.

[12]   Gao, Z.; Antsaklis, P.J.
        Pseudo-inverse method for reconfigurable control with guaranteed stability.
        Proceedings of the 11th IFAC World Congress, Tallin, USSR, pages 16-22, 1990.

[13]   Jiang, J.
        Design of reconfigurable control systems using eigenstructure assignment.
        International Journal of Control, 59, no. 2:395-410, 1994.

[14]   Morse, W.D.; Ossman, K.A.
        Model following reconfigurable flight control system for the AFTI/F-16.
        Journal of Guidance, Control and Dynamics, 13, no. 6:969-976, 1990.

[15]   Huang, C.Y.; Stengel, R.F.
        Restructurable control using proportional integral implicit model following.
        Journal of Guidance, Control and Dynamics, 13, no. 2:303-309, 1990.

[16]   Montenegro, S.
        Sichere und fehlertolerante Steuerungen: Entwicklung sicherheitsrelevanter Systeme.
        Carl Hanser Verlag München Wien, 1999. ISBN 3-446-21235-3.

[17]   Blanke, M.

Diagnosis and Fault-Tolerant Control.
Springer-Verlag 2003. ISBN 3-540-01056-4.

[18]   Laprie, J.-C.
Dependability: Basic Concepts and Terminology in English, French, German,
Italian and Japanese.
Springer-Verlag, Vienna, Austria, 1992.

[19]   Philips Semiconductors
Application Note of KMZ41 and UZZ9000

[20]   W.A.Hill, R.A.Turton, R.J.Dungan and C.L.Schwalm
A Vector-Controlled Cycloconverter Drive for an Icebreaker.
IEEE Transaction of Industrial Application, Vol.23, No.6, page 1036-1042,1987.

[21]   J. Hu, B. Wu
New Integration Algorithms for Estimating Motor Flux over a Wide Speed
Range.
IEEE Transaction on Power Electronics Vol.13, No.5, September 1998.

[22]   J. Luukko, M.Niemelä and J.Pyrhönen
Estimation of the Flux Linkage in a Direct-Torque-Controlled Drive.
IEEE Transaction on Industrial Electronics. Vol.50, No.2, April, 2003.

[23]   J. Luukko
Direct Torque Control of Permanent Magnet Synchronous Machines-Analysis
and Implementation.
Dissertation of Lappeenranta University of Technology, Finland 2000.

[24]   P.P.Acarnley and J.F.Watson
Review of Position-Sensorless Operation of Brushless Permanent-Magnet Ma-
chines.
IEEE Transaction on Industrial Electronics, Vol.53, No.2. April, 2006.

[25]   K. Sakamoto, Y. Iwaji, T. Endo, Y. Takakura
Position and Speed Sensorless Control for PMSM Drive Using Direct Position
Error Estimation.
Industrial Electronics Society, 2001. IECON '01. The 27th Annual Conference
of the IEEE, Volume 3, 29 Nov.-2 Dec. 2001 Page(s):1680 - 1685 vol.3

[26] B. Nahid-Mobarakeh, F. Meibody-Tabar, and F.-M. Sargos
Back-EMF Estimation Based Sensorless Control of PMSM: Robustness with Respect to Measurement Error and Inverter Irregularities.
Industry Applications, IEEE Transactions on Volume 43, Issue 2, March-april 2007 Page(s):485 – 494.

[27] S. Chi, L. Xu
Position Sensorless Control of PMSM Based on a Novel Sliding Mode Observer over Wide Speed Range.
Power Electronics and Motion Control Conference, 2006. IPEMC '06. CES/IEEE 5th International, Volume 3, Aug. 2006 Page(s):1 - 7

[28] K. Paponpen, M. Konghirun
An Improved Sliding Mode Observer for Speed Sensorless Vector Control Drive of PMSM
Power Electronics and Motion Control Conference, 2006. IPEMC '06. CES/IEEE 5th International, Volume 2, Aug. 2006 Page(s):1 - 5

[29] K.-L. Kang, J.-M. Kim, K.-B. Hwang, K.-H. Kim
Sensorless Control of PMSM in High Speed Range with Iterative Sliding Mode Observer.
Applied Power Electronics Conference and Exposition, 2004. APEC '04. Nineteenth Annual IEEE. Volume 2, 2004 Page(s):1111 - 1116 vol.2

[30] N. Matsui
Sensorless PM Brushless DC Motor Drives.
IEEE Transaction on Industrial Electronics, Vol.43, No.2 April 1996.

[31] B. Nahid-Mobarakeh, F. Meibody-Tabar and F.-M. Sargos
A Globally Converging Observer of Mechanical Variables for Sensorless PMSM.
Proceeding IEEE PESC'00, June 2000, pp.885-890.

[32] Z. Peroutka
Design considerations for sensorless control of PMSM drive based on extended Kalman filter.
Power Electronics and Applications, 2005 European Conference on 11-14 Sept. 2005 Page(s):10 pp.

[33] S. Bolognani, L. Tubiana, M. Zigliotto
Extended Kalman Filter Tuning in Sensorless PMSM Drives.
IEEE Transactions on Industry Applications, Vol. 39, No. 6, Nov./Dec. 2003.

[34] A. Qiu, B. Wu
Sensorless Control of Permanent Magnet Synchronous Motor Using Extended Kalman Filter.
Electrical and Computer Engineering, 2004. Canadian Conference on Volume 3, 2-5 May 2004 Page(s):1557 - 1562 Vol.3

[35] M. N. Eskander, O. M. Arafa, O. A. Mahgoub
Sensorless Control of PMSM and BDCM Based On EMF Extraction And Extended Kalman Estimator.
Industrial Electronics, 2006 IEEE International Symposium on Volume 3, July 2006 Page(s):2168 – 2175.

[36] M. C. Huang, A. J. Moses, F. Anayi, X. G. Yao
Reduced-Order Linear Kalman Filter (RLKF) Theory in Application of Sensorless Control for Permanent Magnet Synchronous Motor(PMSM).
Industrial Electronics and Applications, 2006 1ST IEEE Conference on May 2006 Page(s):1 – 6.

[37] G. Welch, G. Bishop
An Introduction to the Kalman Filter.
Technical report TR 95-041 department of computer science, University of North Carolina at Chapel Hill. April 5, 2004.

[38] R. Dhaouadi, N.Mohan and N.Norman
Design and Implementation of an Extended Kalman Filter for the State Estimation of a Permanent Magnet Synchronous Motor.
IEEE Transaction on Power Electronics, Vol.6, page 491-497, July, 1991.

[39] S.Bolognani, R.Oboe and M.Zigliotto
Sensorless full-digital PMSM drive with EKF estimation of speed and rotor position.
IEEE Transaction on Industrial Electronics, Vol. 46, page 184-308, February, 1999.

[40] B. Nahid-Mobarakeh, F. Meibody-Tabar and F.-. Sargos *Mechanical Sensorless Control of PMSM with Online Estimation of Stator Resistance*.
IEEE Transactions on Industry Application, Vol.40, No.2, March/April 2004.

[41] J-H. Jang, J-I. Ha, M. Ohto
Analysis of Permanent-Magnet Machine for Sensorless Control Based on High-Frequency Signal Injection.
IEEE Transactions on Industry Applications, Vol. 40, No.6, November/December 2004.

[42] J-I. Ha, S-K. Sul
Sensorless Field-Orientation Control of an Induction Machine by High-Frequency Signal Injection.
IEEE Transaction on Industry Applications, Vol. 35, No.1 January/February 1999.

[43] M. Linke, R. Kennel, J. Holtz
Sensorless Position Control of Permanent Magnet Synchronous Machines without Limitation at Zero Speed
28th Annual Conference of the IEEE Industrial Electronics Society IECON'02, Sevilla/Spain, Nov. 5-8, 2002.

[44] J. Persson, M. Markovic and Y. Perriard
A New Standstill Position Detection Technique for Non-salient Permanent Magnet Synchronous Motors Using the Magnetic Anisotropy Method.
IEEE Transactions on Magnetics, Vol. 43, No.2, February 2007.

[45] H.-W. Pan
Ermittlung der Rotorposition und des Feldwinkels durch indirekte Messung der Streuinduktivität zum Zweck der drehgeberlosen feldorientierten Regelung von Asynchronmaschinen.
Dissertation, Uni Wuppertal Fachbereich Elektronik; VDI Fortschritt-Berichte, Elektrotechnik Reihe 21 Nr. 315, 2001.

[46] J. Juliet
Drehgeberlose Lageidentifikation bei elektrischen Asynchronmaschinen. Dissertation, Uni Wuppertal Fachbereich Elektronik
VDI Fortschritt-Berichte, Elektrotechnik Reihe 21 Nr. 372, 2005.

[47] M. Schroedl
Sensorless Control of AC Machines at Low Speed and Standstill Based on the INFORM Method.
Industry Applications Conference, 1996. Thirty-First IAS Annual Meeting, IAS '96., Conference Record of the 1996 IEEE Volume 1, 6-10 Oct. 1996 Page(s):270 - 277 vol.1

[48] R.D. Lorenz
Sensorless Drive Control Methods for Stable, High Performance, Zero Speed Operation
International Conference on Power Electronics and Motion Control EPE-PEMC, Kosice 2000.

[49] M. Linke
Injektion alternierender Trägersignale zur sensorlosen Regelung von Drehfeld-maschinen.
Dissertation, VDI Verlag 2003, ISBN: 3-18-334921-3.

[50] J. Holtz
Sensorless Control of Induction Motor Drives.
Proceeding of IEEE, Vol. 90. No. 8 August 2002.

[51] C.S. Staines, C.Asher, K.G. Bradley
A Periodic Burst Injection Method for Deriving Rotor Position in Saturated Cage-Salient Induction Motors without a Shaft Encoder.
Proc. IEEE-IAS 1998 Annual Meeting, St. Louis, Oct. 12-16, page 617-624.

[52] M.W. Degner, R.D. Lorenz
Using Multiple Saliencies for the Estimation of Flux, Position and Velocity in AC Machines
IEEE-IAS, Industrial Application Society, 32nd Annual Meeting, San Diego, CA, Oct. 1996, Vol.1 page 36-41.

[53] A. Consoli, G. Scarella, A. Test
A New Zero-Frequency Flux Position Detection Approach for Direct-Field-Oriented-Control Drives
IEEE Transaction on Industrial Application, Vol. 36, No. 3, May/June 2000.

[54]   N. Teske, G.M. Asher, M. Sumner and K.J. Bradley
Sensorless Position Control of Induction Machines using Rotor Saliencies under Load Condition
Proc. EPE-Conference, Lausanne, Switzerland, Sept 1999.

[55]   F. Blaschke, J. van der Burgt, A. Vandeput
Sensorless Direct Field Orientation at Zero Flux Frequency
31st IAS-Annual Meeting, 1996, Vol.1, page 189-196.

[56]   T. Gopalarathnam, R. McCann
Saturation and Armature Reaction Effects in Surface-Mount PMAC Motor.
Electric Machines and Drives Conference, 2001. IEMDC 2001. IEEE International 2001 Page(s):618 - 621.

[57]   E. Robeischl and M. Schroedl
Optimized INFORM Measurement Sequence for Sensorless PM Synchronous Motor Drives With Respect to Minimum Current Distortion
IEEE Transaction on Industry Applications, Vol. 40, No. 2, March/April 2004.

[58]   S. Nakashima, Y. Inagaki and I. Miki
Sensorless initial rotor position estimation of surface permanent magnet synchronous motor.
IEEE Proceeding of Electric Machines and Drives Conference. 9-12 May 1999, ISBN 0-7803-5293-9.